Adaptation for Climate Change

Protocols for representing variability and unsteadiness in flume facilities

Deliverable Number 8.2

Status: final version

Version: 3.3

Date: April 29th 2018

EC contract no 654110, HYDRALAB+

DOCUMENT INFORMATION

Title	Protocols for representing variability and unsteadiness in flume facilities
Lead Author	Frederic Moulin (CNRS-T)
Contributors	Stuart McLelland (university of Hull) Hannah Williams (University of Hull) William Allsop (HR Wallingford) Karl-Ulrich Evers (HSVA) Andrea Haase (HSVA) Nils Reimer (HSVA) Hayley Shen (Clarkson University) Agnieszka Herman (University of Gdansk) Andrei Tsarau (NTNU) Xavi Gironella (UPC) Andrea Marzeddu (UPC) Bas Hofland (Deltares and Delft University of Technology) Guido Wolters (Deltares) Alex Capel (Deltares) Bas Hoonhout (Deltares) Frederic Moulin (CNRS-T) Victor Dupuis (CNRS-T) Ana Mendonça (LNEC) Conceição Juana Fortes (LNEC) Rute Lemos (LNEC) Rui Capitão (LNEC) Maria Graça Neves (LNEC) Maria Teresa Reis (LNEC) Eunice Silva (HR Wallingford) Francisco Taveira-Pinto (UPORTO) Paulo Rosa-Santos (UPORTO)
Distribution	
Document Reference	

DOCUMENT HISTORY

Date	Revision	Prepared by	Organisation	Approved by	Status
December 8th 2017		F.Y. Moulin	CNRS-Toulouse		
December		F.Y. Moulin and all	CNRS-		Draft

22th 2017		participants	Toulouse		
January 18th 2018		F.Y. Moulin	CNRS-Toulouse		Draft
March 7nd 2018		F.Y. Moulin and all participants	CNRS-Toulouse		Draft
April 10th 2018		F.Y. Moulin and all participants	CNRS-Toulouse		Final draft for approval by all
April 26th 2018		F.Y. Moulin and all participants	CNRS-Toulouse		Final draft for last improvement
April 29th 2018		F.Y Moulin	CNRS-Toulouse		Final document

ACKNOWLEDGEMENT

This project has received funding from the European Union's Horizon 2020 research and innovation programme under grant agreement No 654110, HYDRALAB+.

DISCLAIMER

CONTENTS

1 INTRODUCTION

This deliverable is related to task 8.2 "Innovative approaches for representing variability and unsteadiness in flume facilities". The objectives of the task were to develop and test new protocols for reproducing the variability and unsteadiness associated with changes in the frequency and magnitude of extreme events driven by climate change. The strategy was to model experimentally the likely variations in wave and current forcing that will result from climate change. For ice/structure interactions, there was also the need to represent the variability of ice properties under changing conditions forced by climate change. These new protocols were required to have Europe's experimental facilities able to fully capture the variability of anticipated wave, current and ice dynamics, so that they can ultimately reproduce and quantify the (often non-linear) impacts on system response and trajectories of change.

At the very beginning of the project, a first deliverable (D8.1) was produced as part of task 8.1, consisting in a critical review of previous and on-going research programs that use physical models to investigate the impact of climate change. This review helped to define a set of experiments and tests carried out as part of task 8.2 in order to design new protocols or improving existing ones.

In coastal environments, climate-change scenarios predict an increase of the sea-level and both the frequency and amplitude of extreme storm events. In fluvial environments, the same scenarios predict an increase of both the frequency and amplitude of flood events. Meanwhile, the extent of the arctic sea ice will reduce significantly and its structure undergoes strong modifications: due to ice thickness reduction in the so-called Marginal Ice Zone (MIZ), breaking of the ice cover in flakes that dampen less efficiently gravity waves lead to very different forcing on the wave coastline.

As pointed out in deliverable D8.1, the evolution of hydro-ecosystems under climate-change forcing depends on complex and highly non-linear interactions among biology, morphodynamics and hydrodynamics that must be incorporated in physical models. Because of these non-linearities, all time-scales that are involved in the forcing are of importance, leading to highly different responses to the forcing regimes illustrated in Figure 3 of deliverable D8.1. However, since biological and morphodynamics aspects are at the core of tasks 8.3 and 8.5, it was decided that the deliverable of task 8.2 would essentially deal with aspects not addressed in the other tasks.

Among all the key focus areas identified for future research efforts in the critical review of deliverable D8.1 that did not involve interactions with biology and morphodynamics, most of them were related to the improvement of practices in the design of coastal structures. Not surprisingly, in a context of climate-change, there is a socio-economical need for maintaining a level of performance high enough for coastal structures (seawalls, vertical and rubble mound breakwaters) facing the consequences of climate-change (see elevation, storminess increase). For the design of vulnerable coastal infrastructures, owners / designers generally use targets that are highly sensible to any change of the forcing, like very low overtopping discharges, weak damage and so on. Existing practices were designed without taking into account future changes, and need to be improved to address the question of climate change.

In the critical review, the impact of climate change on ice in the Marginal Ice Zone (MIZ) was also discussed. It appears that the final wave forcing on the coastal shoreline is highly dependent on the

ice cover properties, thickness, intrinsic properties and state (grease, floes, consolidate). However, experimental data for the parametrization of wave attenuation in large-scale models are lacking, and there is a strong need to adapt existing ice tanks in order to address this question.

All these considerations led the partners to carry out complementary experiments in the different available infrastructures in order to test new methodologies and improve existing protocols:

- Wave overtopping measurements:
  In the flume of Wallingford (HRW), measurements of overtopping events and discharges in two 2D stable configurations were performed: on a vertical smooth wall and on a smooth slope. The objective was to focus on measurements in low overtopping conditions which are difficult and encountered in strategies for climate change adaptation. LNEC´s and FEUP's tests also complemented data of HRW for low overtopping conditions, with a rough slope in addition to a smooth one;
  Typically, overtopping measurements show a large scatter in results, especially when it comes down to low overtopping conditions. In order to reduce the uncertainty more insight is required in parameters like flow depth and bore speed of each individual wave. Therefore in the flume of Deltares, such measurements have been performed in which a video imagery technique is explored using artificial intelligence techniques (machine learning).

- Breakwater damage measurements:
  They were performed in 3 different facilities using stereo photogrammetry (LNEC, FEUP and Deltares). The objective of the 2D and 3D tests was to develop new damage parameter approaches which can be employed for complex breakwater geometries and to investigate structural alternatives to combat increased loading due to climate change.
  For damage evolution assess, LNEC´s 2D tests were carried out in parallel with 3D model breakwater stability tests conducted at the Faculty of Engineering of the University of Porto (FEUP) and 2D model tests at Deltares. FEUP´s tests were made in cooperation with Deltares.
  In the wide flume of the university of Porto (FEUP), measurements of overtopping and damage were performed for a 3D unstable configuration: for a rubble mound. The objective was to complete the data of HRW and LNEC with potential 3D effects. In the Scheldt Flume of Deltares 2D damage measurements were performed of a rock armoured breakwater structure with and without berm and using variable water levels.).

- Storm event and sequence modelling:
  In the flume of UPC, measurements of damage were performed for a 2D unstable configuration using stereo photography, focusing in particular on the physical modelling of a storm and the differences with the classical constant wave forcing protocol.

This plan of complementary experiments led to the collaborative production of three papers published and presented at the conference "Coasts, Marine Structures and Breakwaters 2017, "Realising the Potential", 5 - 7 September 2017 - Liverpool Waterfront , UK.

In parallel, experiments of ice-waves interactions were undertaken in the ice tank of HSVA, and a scanning 3D-2C PIV system has been tested in the flume of CNRS-T for the investigation of a typical multi-scale turbulent flow, focusing on spatial and time convergence issues for turbulent structures analysis.

In addition, task 8.2 has also benefited from tests and experiments conducted as part of the Transnational Access programme. Some results related to the task have been included in the deliverable. It consists in the development of a video image technique for the estimation of overtopping discharges (see section 2.3) and the investigation of the impact of rain fall event sequence on landscape shaping (see section 2.7).

All these tests are described and discussed in the present document. All the potential obstacles for future research efforts that were identified in the earlier critical review (deliverable D8.1) and related to task 8.2 are investigated here and the issues associated with morphodynamics and biology will be discussed in the deliverables of task 8.3 and 8.5 respectively.

At the end of each section, depending on the completeness of the experiments realized and the difficulties faced during the experiments, two kinds of conclusions are proposed in the present document. When the test results were conclusive, protocols have been built, that are recommended for facility users who would like to perform the same kind of study. In this case, the last subsection is entitled "recommended protocol" since it fulfils the right level of confidence for a protocol. When the test results were not conclusive, the last subsection has been written as a list of suggestions and recommendations to help the facility users to be aware of difficulties associated with this kind of experiments. The last subsection is then entitled "recommendations" since it does not fulfil the level of confidence expected for a protocol.

2 RESULTS

2.1 BREAKWATER DAMAGE ASSESSMENT FOR DIFFERENT STORM EVENT MODELLING APPROACHES

2.1.1 Objective description

Historically, significant wave height, wave period, storm direction and water level have been considered the main design variables for coastal structures. Based on these variables, physical model tests both in 2D or 3D wave facilities have been carried out for the design/optimization of the structures. Classically, the test methodology for the study of armour layer stability starts with the selection of one or more return periods (typically between 10 and 500 years), normally associated to the desired life expectancy of the structure. Associated to such return periods, significant wave heights could be obtained from the so-called extreme wave data samples, by assuming that extreme events follow an extreme probability density distribution (often a Fishet-Tippet-family extreme value distribution or a Weibull distribution are considered). The extreme wave regime normally consists of extrapolated values of the annual maximum significant wave height and maximum wave height, for a set of return periods, together with periods and directions associated, in some manner (usually, a correlation adjustment), to those extrapolated values. Instead of annual maximum values, we may use, if data are scarce, storm maximum values, using POT (Peak-Over-Theshold) method, as a common alternative. However, the correlation between wave height and period (and also with wave direction) variables usually shows a large scatter. Some laboratories propose to perform tests with constant wave steepness, considering values typically associated to storm conditions, e.g. from 0.02 to 0.06. Usually, 3 to 4 wave steepness values are selected in order to produce the same number of wave test conditions for the significant wave height and the peak period (H_s, T_p). A series of tests with 60, 80, 100 and 120% of the significant wave height with the associated peak/mean period (with constant wave steepness) may be performed to monitoring damage evolution (Owen & Allsop, 1984).

Recently, Martín-Hidalgo *et al.* (2014) and Martín-Soldevilla *et al.* (2015) studied analytically the damage evolution of an armour layer during real and synthetic storms. The authors showed that damage evolution is affected by storm sequencing by means of the empirical maximum energy flux model (J. A. Melby & Kobayashi, 2011). From all the tested synthetic storms, Martín Soldevilla *et al.* (2015) suggests that the Equivalent Magnitude Storm model (EMS) generally provides the best results for the most common kinds of storms (predominant sea, swell or both). According to these authors, a triangular shape is recommended for typical sea storms whereas a trapezoidal shape is more appropriate for more developed storm conditions. Also, by appropriately using these storm patterns it would be possible to define the complete evolution of the design storm for the required structure lifetime and return period. The synthetic storm could be used as a design parameter associated to the design return period, instead of the usual significant wave height. In this sense, consideration of other relevant variables, namely the wave period, the storm duration and the water level, is feasible and essential for a more sophisticated structure optimization.

Here, we study experimentally the damage assessment of a two-layer cubic block breakwater under a real storm, a synthetic storm and the classical methodology considering a wave steepness of 0.02, being this steepness associated to the design condition H_s, T_p of the peak of the real storm.

It is important to remember that the three methodologies tested for this report are fare from representing a comprehensive picture of the problem and that several simplifications have been used. A realistic comparison is very difficult though this report could be used as a simple guide to highlight possible source of errors in the different tested methodologies. In particular, different real storms, initial thresholds, wave steepness, synthetic storm profiles, etc. should have been tested

Two different methodologies for the measurement of damage have been considered. The classical N_{od} or Relative damage (Van der Meer, 1999) and the eroded depth (J. a. Melby & Kobayashi, 1998) around the mean water level have been used. The second approach, though not normally used for concrete armour layers, has been applied starting from a 3D digital model of the breakwater based on a series of images captured with an action camera. A high volume of information on the position and evolution of damage can be extracted from the digital model, however, for the scope of this deliverable report only the erosion profiles have been analysed. Measurement of damage in 2D and 3D physical models is considered in more detail in Section 2.2.

2.1.2 Tests and experiments

The experiments were carried out in the CIEMito wave flume at the Laboratori d'Enginyeria Maritima (LIM) of the Universitat Politecnica de Catalunya (LIM-UPC BarcelonaTech). The flume is 18 m long, 0.38 m wide, and 0.56 m deep. It is equipped with a piston-type wave paddle that generates regular and irregular waves.

During the experiments, only 14 m of the flume were used and the breakwater model was placed at the end of a 1:30 smooth slope. The breakwater model that has been used in the tests is a scaled model of the one used by Van der Meer (Van der Meer, 1988b) with a scale factor of 3. The selection of this configuration is due to the direct application of the stability formulae of Van der Meer (Van der Meer, 1988b, 1999). This facilitates determining pairs of H_s, T_p (peak of the storm values) that make the breakwater slightly unstable at the CIEMito tests. A sketch of the experimental set-up is given in Figure 1.

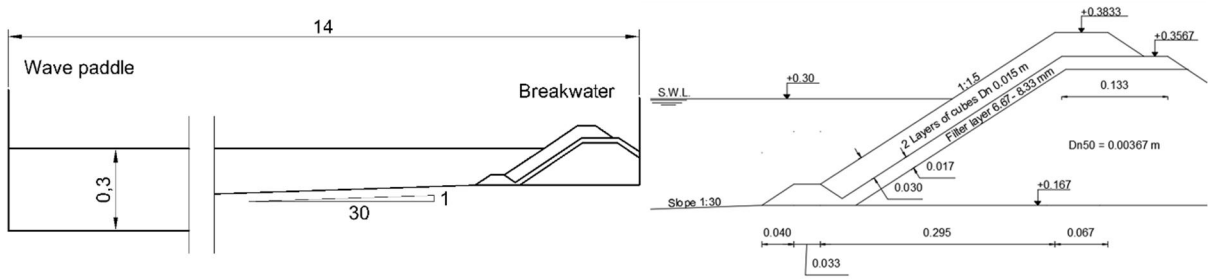

Figure 1 : Experimental layout – Ciemito wave flume configuration (Left) – breakwater cross-section (Right) – All dimensions in meters.

The core and filter layers consist of rubble gravel while the armour layer consists of resin cubes with a lead core in order to achieve, at the working scale, the same overall mass-density of prototype

concrete blocks given that fresh water was used in the laboratory tests. The characteristics of the three layers are summarized in Table 1.

The porosity of the breakwater remained constant throughout all experiments with a value of 40%. This has been achieved by placing always the same number of blocks, in the two layers and in the same area. Exactly 23 rows of 17 blocks have been deployed in an area of 0.385x0.345 m^2 for each layer. Every block has been numbered with a three digit unique number in order to be recognized later during the visual counting of the blocks that have moved.

Table 1 : Material properties

Layer	M_{50} [g]	Dn_{50} [mm]	ρ [g/cm3]
Core	0.13	3.7	2.65
Filter	0.9	7	2.65
Armour	7.7	14.5	2.29

Five resistance wave gauges were used for measuring the free surface elevation at 2.00, 2.82, 3.50, 13.48 and 11.2 m from the wavemaker. A sampling rate of 100 Hz was used; the degree of accuracy of these sensors is approximately 0.001 m (Oliveira, 2012; Stagonas et al., 2016). Pictures of the breakwater were taken before and after every wave test with a GoPro Hero 3+ black edition and the pictures for the 3d digital model of the breakwater have been taken with a QUMOX SJ4000. Both cameras have a resolution of 12Mp.

Real storm

The selected real storm was measured in the Mediterranean sea at a depth of 65m in front of the village of Blanes in Catalonia. The sea state was measured using a Datawell 'Wave Rider' buoy that belongs to the XIOM network. The storm was an extreme event that produced severe damage to beaches and structures along the Catalan coast. The bouy records 20 minutes of raw data every hour and returns wave statistics and spectra. The sea state curve exceeded the threshold of 1.5m significant wave height on December 26th at 10:00 AM and maintained a significant wave height larger than the threshold for 74 hours. At the peak, the storm showed a significant wave height of 4.65 m and a peak period of 11.6s. The storm evolution in terms of H_s and T_p is shown in Figure 2.

After a first series of hydraulic tests and based on the observed functional/resistance performance only the steps with a significant wave height higher than 3m have been used for the calculation of the synthetic storm.

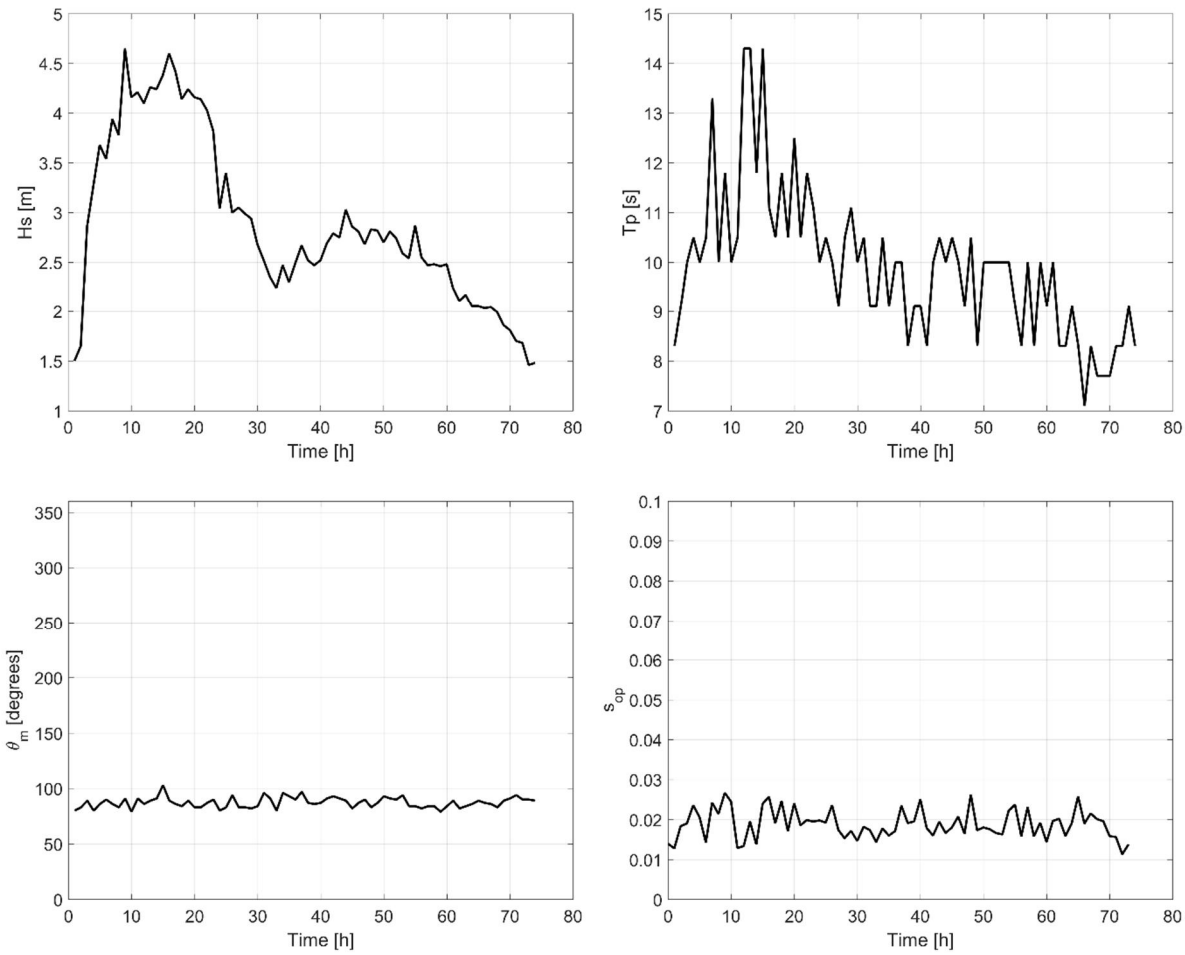

Figure 2 : Storm measured on December 26th 2008 at 41°39.003'N, 2°48.940'E – From top left clockwise - Significant wave height Hs (Left) – Peak period Tp (Center) – Direction θ_m (Right) – Wave steepness S_{op} - Recorded by LIM-UPC (Bolaños et al., 2009)

Classical methodology

For the tests carried out following the classical methodology the pair H_s, T_p of the peak of the real storm was used as the main design parameter. As described above, previous laboratory results suggested that tests should be performed with constant wave steepness, using values typically associated with storm conditions, e.g. from 0.02 to 0.06. Usually, 3 to 4 wave steepness values are selected in order to produce the same number of wave conditions (H_s, T_p). In our simplified methodology, to facilitate inter-comparisons, a single constant steepness has been used and it is the one associated to H_s, T_p of the peak of the real storm which is approximatively 0.02. It is also possible to see from Figure 2 that the wave steepness is oscillating around this value for all the duration of the real storm. A series of tests with 60, 80, 100 and 120% of the design significant wave height combined with the associated peak period were performed to monitor damage evolution following the classical methodology. The duration of each step was calculated starting from the number of waves generated during each step (N=1000).

Synthetic storm

The synthetic storm model used for these experiments is the 'Equivalent Magnitude Storm' (EMS) proposed first by Martín-Hidalgo et al., 2014, and improved later by Martín-Hidalgo *et al.* (2014) and Martín Soldevilla *et al.* (2015). This synthetic storm intends to reproduce the real storm with an isosceles triangle in which the peak is represented by the H_s peak of the real storm and the duration is established such that its magnitude (area describing the storm history above a threshold, introduced by De Michele *et al.* (2007) equals the one of the real storm. The threshold for these tests has been established at an H_s = 3 m based on previous tests. The threshold has been chosen in order to be as close as possible to the 60% of the design wave height that is also the first step in the classical methodology.

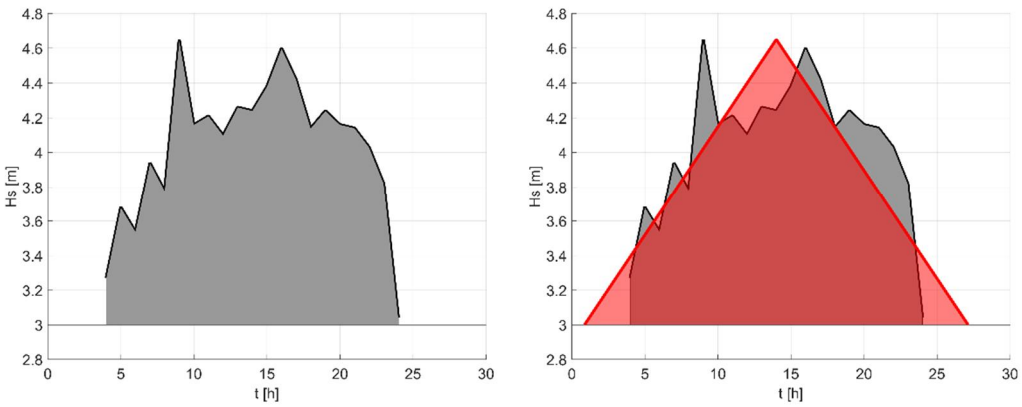

Figure 3 : Real Storm over a threshold H_s of 3m. In grey has been highlighted the storm profile (Left) – In red the EMS has been superposed over the real storm (Right)

The magnitude 'M' (measuring the energetic content) of the real and synthetic storm is M=21.7m·h. The duration of the synthetic storm is 26.2h instead of the 20h of the real storm. As for the classical methodology, for these tests only one constant steepness has been used and is the one associated to the design condition H_s, T_p of the peak of the real storm, that is approximately 0.02 (see Figure 2).

Design of the experiments

The scale of the experiment was chosen by taking into account that the breakwater under wave attack with the pair H_s, T_p of the real storm peak should have been unstable. Starting from the dimension of the block (scaled 1/3 with the Van der Meer structure), applying the formula of Van der Meer (Van der Meer, 1988b) with an associated N_{od}=2, the corresponding H_s has been calculated with eq(1).

$$\frac{H_s}{\Delta D_n} = \left(6.7\frac{N_{od}^{0.4}}{N^{0.3}} + 1.0\right) S_{om}^{-0.1} \qquad (1)$$

with:

H_s = significant wave height
Δ = submerged density
D_n = Nominal diameter
N_{od} = relative damage

N = number of waves
S_{om} = wave steepness associated to the mean wave period

The calculated significant wave height that generates the expected N_{od} is approximately 0.06 and this leads to scaling parameter of 1/77.5. For simplicity a scale of 1/80 has been applied and the pair H_s, T_p associated to the peak of the storm, scaled to the CIEMito wave flume dimensions will be H_s=0.058m and T_p=1.3s. These values and the scaled real storm have been considered for the calculation of the synthetic storm profile and for designing the tests following the classical methodology.

Once the scale and the duration of the discretized steps have been chosen the three storms have been scaled and propagated at the paddle water depth (0.3m in the wave flume and 24m in prototype).

For the real storm a total of 21 irregular wave conditions (generated with a Jonswap spectrum) were tested with H_s and T_p in the lab ranging between 0.035 – 0.054 m and 1.12 – 1.6 s, respectively. The length of each time series was 402 s and a Jonswap spectral parameter (γ) of 3.3 was used to represent the sea states. The scaled and propagated, measured and discretized real storm over a threshold of 0.035m is shown in Figure 4. This representation of the real storm will be called from now "Real Storm Methodology" (RSM)

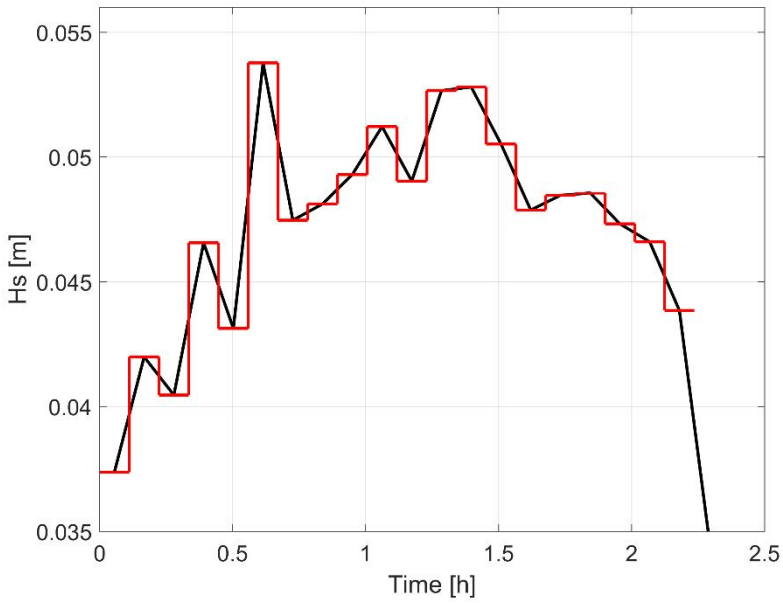

Figure 4: Real storm scaled 1/80, propagated at the wave paddle depth (black) and discretized in steps of 402s each (red)

For the classical methodology, to facilitate inter comparisons, the H_s, T_p chosen for the "100% step" are the one of the peak of the recorded storm. Only one constant steepness has been used that is S_{0p}=0.02, which is given by H_s, T_p recorded at the peak of storm. For a working scale of 1:80, this corresponds to target H_s and T_p in the lab of 0.054m and 1.3s, respectively. The tests with 60, 80, 100 and 120% of the design significant wave height with the associated peak period have been performed to monitor damage evolution under the classical methodology. This corresponds to a target H_s of 0.032, 0.043, 0.054 and 0.065 m, respectively. The duration of each step has been

calculated starting from the number of waves generated during each step, that was N=1000. The scaled and propagated measured real storm and discretized classical storm are shown in Figure 5

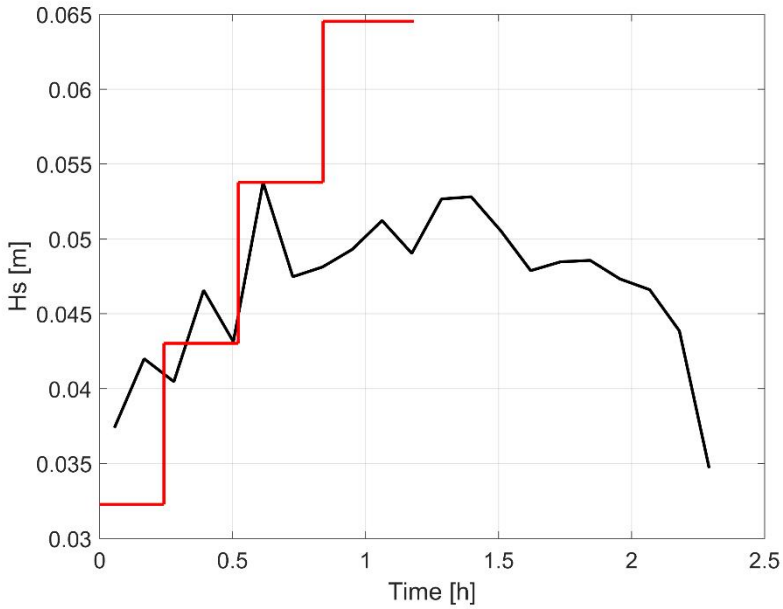

Figure 5 : Classical storm methodology (in red) derived from the scaled and propagated measured storm (in black)

For the classical methodology is important to identify two significant steps. The first is the design step (100% step) that from now on will be called CM100. The second step is the end of the test program (120% step) that is normally considered in order to assure that the armour has not been significantly overdesigned. We will refer to this step as the CM120.

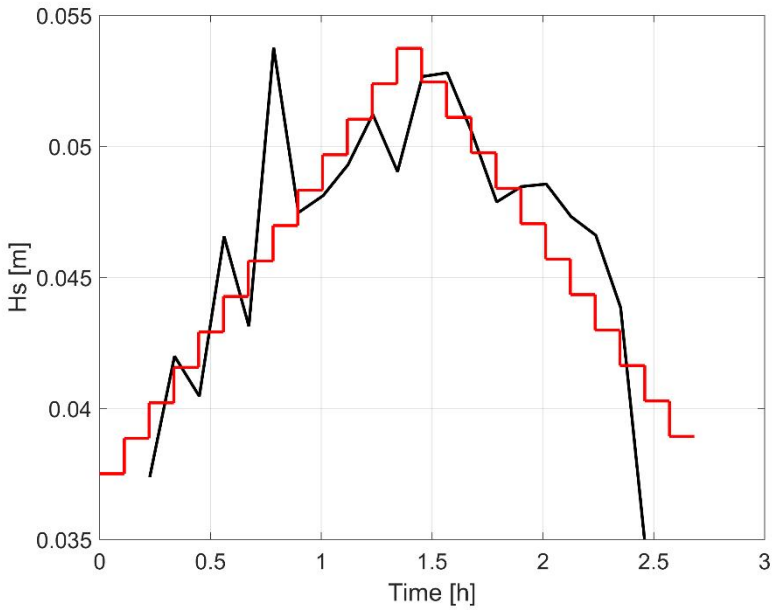

Figure 6 : Synthetic triangular storm methodology (in red) derived from the measured, scaled and propagated measured storm (in black)

Using the same discretization as for the real storm, for the synthetic storm model "EMS" with triangular shape, the length of each time series is 402s and 25 irregular wave conditions (generated with a Jonswap spectrum) were tested with H_s and T_p in the wave flume ranging between 0.035 – 0.054. As for the classical methodology, only one S_{0p} is used and is the one associated to the design condition H_s, T_p of the peak of the recorded storm, that is approximately 0.02. The scaled and propagated measured real storm and the discretized synthetic storm are shown in Figure 6.

From now on the results associated to the cumulative damage at the end of the test program of this synthetic storm model will be identified with the name EMSTRIA.

Comparison in between the RSM and the EMSTRIA will be performed at the end of the test program. These results will also be compared with the CM100 step. A direct comparison is not easily justifiable but it is possible to consider the measured cumulative damage at these points as the ones used for the final design/verification process.

Comparison at these "strategic points" will be performed in order to assess the capacity to improve the representation of the variability and unsteadiness of natural storms applied to stability tests.

Test program

In order to minimize the variability due to the test methodology the following criteria have been applied for the execution of all tests:

1. Construction of the filter layer;
2. Acquisition of 70 to 90 pictures from different angles to prepare the 3D digital model.
3. Construction of the breakwater placing 17 blocks in each of the 23 rows for the two layers.
4. Acquisition of 70 to 90 pictures from different angles of the complete breakwater for the preparation of the 3D digital model of the initial armour layer (Reference 3D).
5. Perpendicular (view) picture of the breakwater for the visual counting (Reference picture).

For the real and synthetic storms:

6. Wave attack sequences.
7. Perpendicular (view) picture of the breakwater to compare with the reference picture for the visual counting of the number of blocks that have been displaced during the wave attack.
8. Steps 6 and 7 repeated until the storm peak step.
9. Realization of 70 to 90 pictures from different angles for deriving the 3D digital model of the armour layer after the storm peak (to be compared with the Reference 3D).
10. Step 6 and 7 repeated until the end of the test program (end of the storm or no damage increase).
11. Realization of 70 to 90 pictures from different angles for deriving the 3D digital model of the armour layer after the complete test program (to be compared with the Reference 3D).
12. Deconstruction of the damaged breakwater.

For the classical methodology, the 3D map has been obtained after the 100% and 120% steps. After step 12 it would all start again with step 1 (construction of the filter layer) for the next test. Typical images used for the generation of the 3D digital model (top) and for the visual counting of the blocks that have been displaced (bottom) are shown in Figure 7.

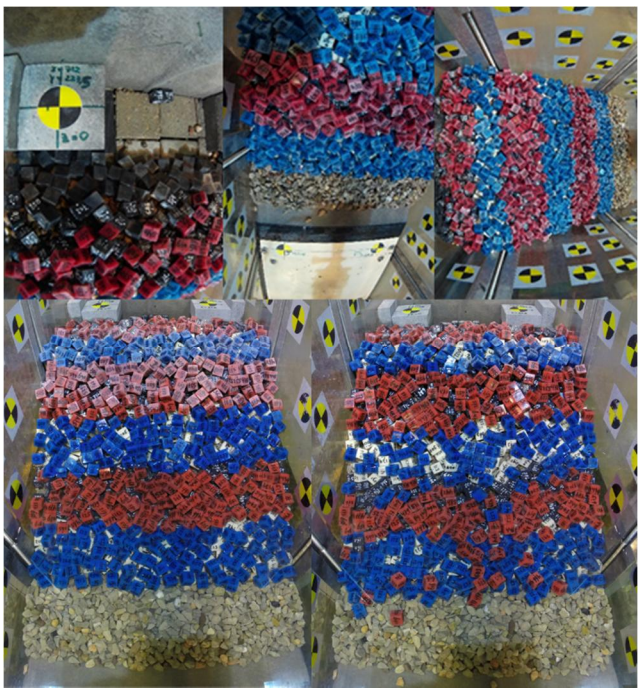

Figure 7 : (3 pictures on top) Example of three pictures in between the 70-90 for the realization of the digital 3D model – (2 pictures on bottom) perpendicular pictures for the visual counting.

Several repetitions of all the tested storms have been performed in order to study the variability of the results. However, a comprehensive analysis has not been completed yet.

2.1.3 Results and discussion

Two types of data analysis have been performed: one starting from the pictures perpendicular to the breakwater before and after the tested storm (Figure7 bottom) and another one using the data from the 3D digital model of the breakwater.

Every block has been identified with a unique three-digit number and could be followed numerically so that the position before and after each test can be checked. Van der Meer (Van der Meer, 1999) defines the relative damage N_{od} as the actual number of units displaced related to a width (along the longitudinal axis of the structure) of one nominal diameter. Furthermore, the author defines damage level associated to the relative damage, starting from N_{od}< 0.5 (acceptable damage) until N_{od}= 2 that represents the complete failure of the structure. The calculation of N_{od} is straight forward once the number of units that have been displaced more than one D_n is known (eq. 2 (Van der Meer, 1988a)).

$$N_{od} = \frac{N_{du} D_n}{w} \qquad (2)$$

where:

N_{du}= number of displaced units
D_n= nominal diameter
w= with of a cross section

In the case of a wave flume (Two-bi-dimensional), the complete width of the flume should be considered as a cross section. The average cross section has been used for the further analysis and we will refer to it as the 'representative profile'.

For the case where the 3D digital model is used for the damage evaluation, 70 to 90 pictures taken from different angles were loaded into the Autodesk Recap 360 program. The code, using common points in between various pictures, returns a 3D digital model of the breakwater as a point cloud. This point cloud is then georeferenced in a local coordinate system with the program Meshlab. Once the georeferenced cloud is loaded into Matlab, a structured mesh (in this case of 1mm) is generated interpolating the georeferenced point cloud values. When the meshes are generated, it is possible to calculate the representative profile of the breakwater for every step. The difference between the representative profile of the considered step (e.g. the profile of the breakwater after the wave attack relative to the peak of the storm) and the initial reference profile returns the erosion profile. From the erosion profile, it is possible to calculate the damage (eq. 3, Melby and Kobayashi (1998)).

$$E = \frac{d_e}{D_n} \tag{3}$$

where:

E = relative eroded depth
d_e= eroded depth
D_n= nominal diameter

The results of the three methodologies (RSM, CM100 and EMSTRIA) are illustrated and summarized in this section. A comparison in terms of relative damage and eroded depth has been made. The comparison of the three representative profiles is shown in Figure 8.

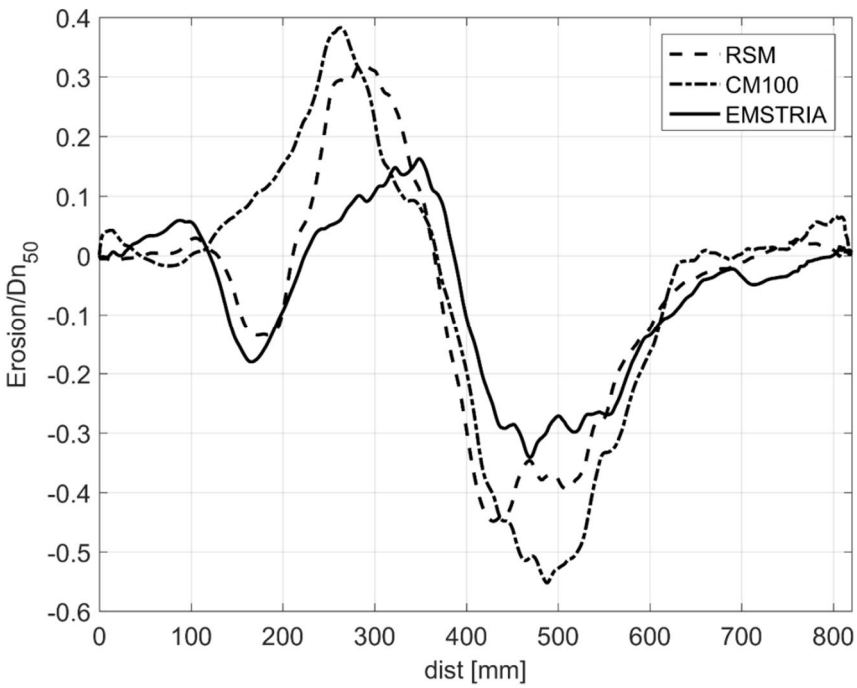

Figure8 : Representative erosion profiles comparison – all the results are plotted using the 3D digital model

In Figure the erosion profiles obtained from the 3D digital model are compared at the end of the test series for the RSM and EMSTRIA and at the step CM100 for the classical methodology. Qualitatively, it is possible to observe several differences and analogies in between the three profiles. The RSM test will be used as the benchmark in order to compare the other results.

Notably, the CM100 test (dash-dot line) returns a bigger eroded depth while the EMSTRIA presents a smaller eroded depth. Similar qualitative behaviour is observable for the deposition. The CM100 presents the larger maximum value while the EMSTRIA the lower value. The RSM shows an intermediate behaviour. On the flip side the position of the eroded and deposited area is similar for the three methodologies.

Table 2 summarizes the quantitative results. The relative damage N_{od} and the non-dimensional eroded depth *E* are compared for the three tested methodologies.

Table 2: Comparison of the results of the three test methodologies.

Case	*Nod*	*E*
RSM	4	0.45
CM100	5.9	0.50
EMSTRIA	2.35	0.34

N_{od}, as shown in the methodology section, is an extrapolated result from the visual counting of the blocks that have been displaced more than one D_n from the pictures taken perpendicular to the slope of the breakwater. In accordance with the visual analysis of the erosion profiles (Figure), it is possible to appreciate that the three methodologies return different results in terms of both relative damage N_{od} and eroded depth *E*. In particular, in terms of N_{od}, the CM100 shows a 47.5% increase in the damage if compared with the benchmark RSM while the EMSTRIA returns a 41.3% less damage. If the relative erosion depth is considered instead, the CM100 shows an 11.1% increase in the damage if compared with the benchmark RSM while the EMSTRIA returns a 24.4% less damage. It is then possible to appreciate from the results of Table 2 that the use of any of the damage indicators (N_{od} and E) will lead to similar qualitative conclusions.

It is also important to notice from Figure 7 that if the relative damage evolution is considered very different behaviours are noticeable. The CM shows an almost constant and steep growth during all the test run; the RSM shows a less but still steep growth until the peak of the storm and a milder increase of the relative damage from the peak of the storm until the end of the test series. The EMSTRIA instead, shows a moderate increase in the damage until the peak of the storm and almost no damage progression from the peak to the end of the test series.

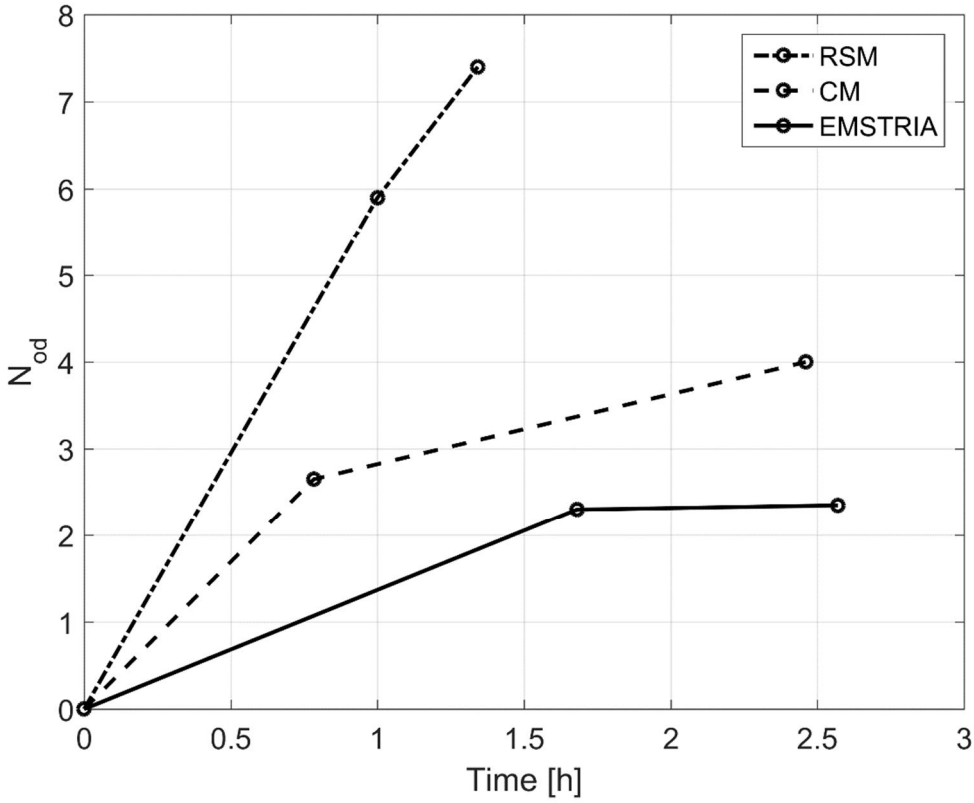

Figure 7: Nod Progression for the three methodologies

2.1.4 Recommendations

Whilst stability of a two-layer cubic block breakwater may be estimated using empirical models, a large numbers of variables (both physical and geometric) play a significant role in armour layer damage and discrepancies in comparison with analytical results are very likely. Therefore, physical experiments are recommended to study the stability of breakwater armour layers. A new methodology, based on a triangular synthetic storm (EMSTRIA) has been tested against a real storm (RSM) measured in the "Mediterranean Sea" with equivalent magnitude. A comparison with the classical methodology (CM) has also been performed. The RSM and the EMSTRIA are characterized by the same peak wave height, the same magnitude and the same global wave steepness. The CM100 has the same significant wave height and wave period of the peak of the RSM and the other steps (60, 80 and 120%) are based on this step. The four steps of the CM have the same global wave steepness of the EMSTRIA.

Clearly, a comprehensive comparison could only be made testing a large number of different real and synthetic storms (both methodologies and shapes) and performing a high number of repetitions but, suggestions could arise from the available results:

- For the studied case, the relative damage at the CM100 step, is 47% bigger than the relative damage for the RSM. If the N_{od} at the CM120 step is considered the difference with the RSM rises until the 85%.
- For the studied case, in comparison with the RSM, the EMSTRIA underestimate the damage of a 41.3%.

- The evolution of the relative damage shows also different behaviours for the three tested methodologies.
- If the CM is used, it is important to consider the real duration, in terms of number of waves, both of the peak and the complete real storm. For this case the peak of the RSM does not last for more than few hours and therefore performing tests with the classical methodology with more than 1000 waves (3h at the prototype scale) could lead to too conservative results.
- The authors recommend the study of historical sea states data and the selection of a synthetic storm shape that best fits the local storm shapes. In this case, a trapezoidal shape for the synthetic storm may have led to improved results.
- The placement of armour layer units is a critical step and could introduce variability in the results. Although a very strict methodology for the placement of the armour units was followed to guarantee the correct porosity, visual differences on the randomness of the placement are evident between reconstructions of each test. For this reason, a number of repetitions of the same test are recommended.
- In order to control the real porosity of the breakwater (once built), the use of the 3D reconstruction could be very useful. Subtracting the 3D reconstruction of the filter layer by the 3D reconstruction of the armour layer will return the local armour layer real thickness. Same procedure should be done also for the filter and the core.
- Preliminary data analysis performed on multiple repetitions if the same test suggests that the variability found in the damage, between repetitions of the same tests, is very large. Variations of more than 100% in between the minimum and the maximum damage associated to the same tests have been found.
- The photogrammetry 3D reconstruction could be a really helpful tool in order to automate damage calculation.

Far from being a comprehensive analysis, these tests want to be a first step towards an improved methodology for the design/verification of the breakwater's armour layer. Further experiments and analysis should be performed in order to study the capability of a synthetic storm to reproduce the real world. In particular, different shapes of the synthetic storm should be tested against multiple real storms. The parameters affecting the wave statistical distribution in a time series should also be tested in their range of variability in the real world. The designer, however, should be, in any case, sufficiently critical to apply the correct methodology that better represent the design conditions.

2.2 MEASUREMENT OF DAMAGE IN 2D AND 3D PHYSICAL MODELS OF BREAKWATERS BREAKWATERS BY STEREO-PHOTOGRAPHY

This aim of this set of experiments was to improve the description of damage to structures, investigate the effect of the sequence of events during testing, as well as understanding the possible influence of sea level rise. The test program was carried out in parallel both in 2D and 3D physical model tests, at the National Laboratory for Civil Engineering (LNEC, Portugal) and at the Faculty of Engineering of the University of Porto (FEUP, Portugal), respectively, working both in cooperation with Deltares.

2.2.1 Objective description

The aim of the scale model tests was to describe methods to assess damage in coastal structures under variable conditions in a flexible yet systematic manner. To achieve this goal, detailed scans of 2D and 3D tests on rock-armoured structures have been obtained. These scans are analysed in depth to investigate the damage behaviour under varying conditions, and to obtain representative parameters to describe and qualify the stability of the adapted structures.

2.2.2 Test campaigns

To obtain a large dataset of high-resolution damage scans, two test campaigns were performed and combined with existing datasets. The new test campaigns consisted of:

- 2D tests at LNEC, Portugal, where several kinds of cumulative damages on the tested structure were measured, considering increasing significant wave height build-up and constant peak period conditions;
- 3D tests at FEUP, Portugal, where the influence of wider test sections, a roundhead, and short-crested wave attack was investigated, for constant wave steepness
- 2D tests at Deltares, Netherlands, where the influence of varying water levels on damage (in depth-limited conditions), cumulative and non-cumulative damage, and structural adaptation alternatives to sea level rise (berm configurations) were investigated.

Definition of damage

In the 2D and 3D tests at FEUP and Deltares, the damage was defined as:

$$S_m = \frac{\langle e \rangle_{w=mDn50}}{D_{n50}}$$

$$E_{2D,m} = \frac{max_x(\langle e \rangle_{w=mDn50})}{D_{n50}}$$

$$E_{3D,m,n} = \frac{max_{x,y}(\langle e \rangle_{R=nDn50})_{w=mDn50}}{D_{n50}}$$

where the (always positive) local erosion depth is defined as $e = max[\ (z_{\text{before}} - z_{\text{after}})cos\alpha\ ;\ 0\ ]$, α is the structure slope, $\langle\ \rangle_{w...=}$ is a spatial average over the width of a flume (in the alongshore direction), $\langle\ \rangle_{R=...}$ is a (moving) spatial average over a circular area with radius R, m and n are integers, and Dn50 is the nominal diameter of the armour rock for which 50% of the rock mass is smaller. max_x is a maximum over the (cross-shore) x-direction and $max_{x,y}$ is a maximum over an area spanning the alongshore and cross-shore horizontal area.

In the case of the 2D tests at LNEC S_m and $E_{2D,m}$ definitions were used to evaluate the damage.

2D tests at LNEC

A first test series was carried out to obtain damage scans for a standard wave flume case (see Figure 10). These tests were done at in a 50 m long, 1.2 m deep, wave flume with an operating width of 0.8 m.

The flume is equipped with a piston-type wave maker that combines both irregular wave generation and dynamic absorption of reflected waves through the use of two wave gauges located in front of the paddle. Ten additional resistive-type wave gauges were deployed along the flume and an extra gauge was placed on the model armour layer slope to measure run-up levels (not analyzed here).

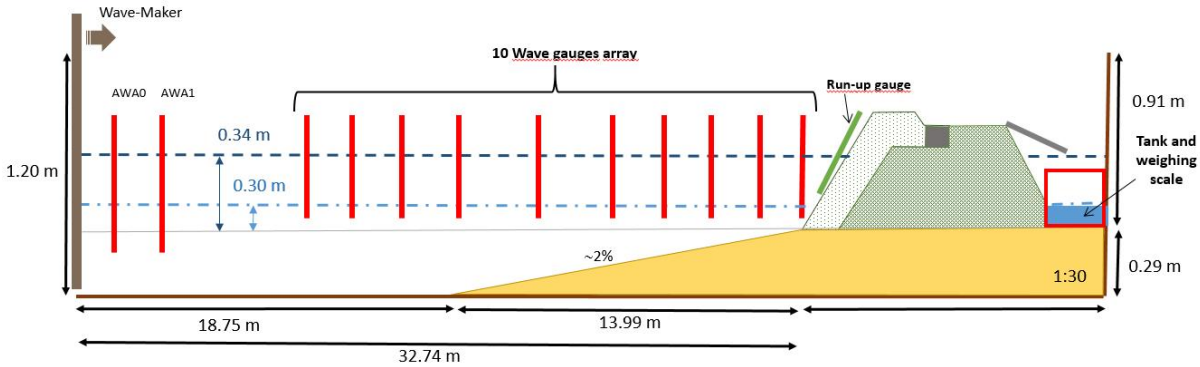

Figure 10 : Sketch of the experimental setup in the wave flume (dimensions for a 1:30 scale and for the minimum and maximum water levels).

The breakwater model was built and operated according to Froude's similarity law, with a geometrical scale of 1:30, to ensure reduced scale effects (the wave height-based Reynolds' number was D_{n50} $(gHs)^{1/2}$ / ν > $3x10^4$).). The reference breakwater cross section was built on a 14 m long and 0.29 m high foreshore, as previously depicted in in Figure 10.

The breakwater model was 0.8 m ($18D_n50$) wide and was composed of a main armour slope of 1:2, $2D_{n50}$ thick, with D_{n50} = 0.0445 m, with a single filter layer and a permeable core below, as shown in Figure 11. The armour crest was located 0.5 m above the structure toe. A concrete superstructure was also included, with its crest level at 1.7 cm below the armour crest. The width of the armour layer crest, seaward of the crest element, was 19.7 cm.

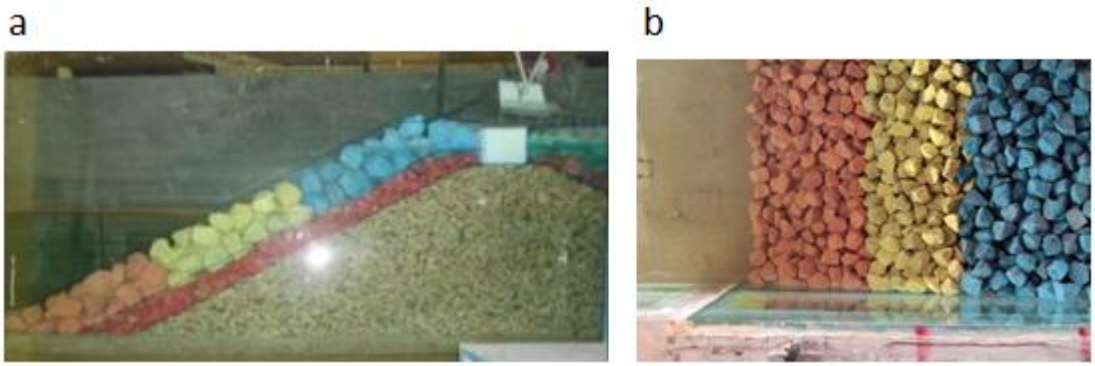

Figure 11 : a) sketch of the experimental setup in the wave flume and b) model overview.

The nominal test conditions are presented in Table 3, where H_s refers to the significant wave height at the toe of the structure and T_p is the peak wave period. ~~Tests 1-7 represent approach A; tests 1-3 and 4-7 represent approach B; tests 1-3, 4-7 and 8-15 represent approach C; and tests 4-7, with rebuilding, represent approach D.~~

Table 3 : Nominal test conditions at structure toe.

Test	Prototype			Model		
	Water Depth, d (m)	T_p (s)	H_s (m)	Water Depth, d (m)	T_p (s)	H_s (m)
1	9.1	10	3.2	0.30	1.83	0.11
2	9.1	10	3.7	0.30	1.83	0.12
3	9.1	10	4.2	0.30	1.83	0.14
4	10.1	11	3.7	0.34	2.01	0.12
5	10.1	11	4.2	0.34	2.01	0.14
6	10.1	11	4.7	0.34	2.01	0.16
7	10.1	11	5.2	0.34	2.01	0.17
Rebuilding						
8	11.1	12	3.7	0.37	2.19	0.12
9	8.1	12	3.7	0.27	2.19	0.12
10	11.1	12	4.2	0.37	2.19	0.14
11	8.1	12	4.2	0.27	2.19	0.14
12	11.1	12	4.7	0.37	2.19	0.16
13	8.1	12	4.7	0.27	2.19	0.16
14	11.1	12	5.2	0.37	2.19	0.17
15	8.1	12	5.2	0.2	2.19	0.17

Two-dimensional damage and overtopping tests for a rock armour slope were performed to represent four approaches: A) a standard cumulative storm build-up (with increasing wave heights) with increasing water level (Tests 1-7); B) a standard cumulative storm build-up with a constant water level (tests 1-3 and 4-7); C) a constant wave period (1-3, 4-7 and 8-15); and D) a standard storm build-up, with a constant water level and with rebuilding (tests 4-7).

Reproduction of the irregular wave tests used a JONSWAP spectrum, whose shape was characterized by a peak enhancement factor of 3.3. Test durations were 1980 s, 2160 s and 2400 s for peak periods of 10 s, 11 s and 12 s, respectively (as to produce approximately 1000 waves per test). For consistency, all tests were repeated at least three times.

The damage was measured without emptying the flume, using a stereo-photogrammetric technique, which allows a complete 3D reconstruction environment, using stereo image pairs as input, taken by two DSLR cameras. This software package (Ferreira, 2006) was able to rectify the distortion introduced by the air-water interface, enabling to survey submerged scenes. Some application and validation are described in Lemos et al. (2017).

The test results of the LNEC tests are reported in Hofland et al. (2017) and Lemos et al. (2018a) and will be presented in the next months in conferences (Fortes et al., 2018) and Lemos et al., 2018b).

3D tests at FEUP (UPORTO)

The purpose of this test series was to obtain high-resolution data on damage to rubble mound structures including 3D effects, namely the impact of short-crested waves and damage to a curved

roundhead section. In addition, a 4.0 m wide trunk section was included to obtain converged statistical values for the damage parameters.

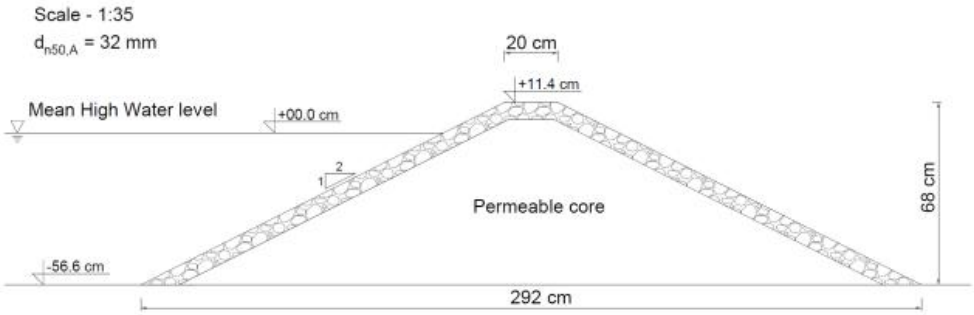

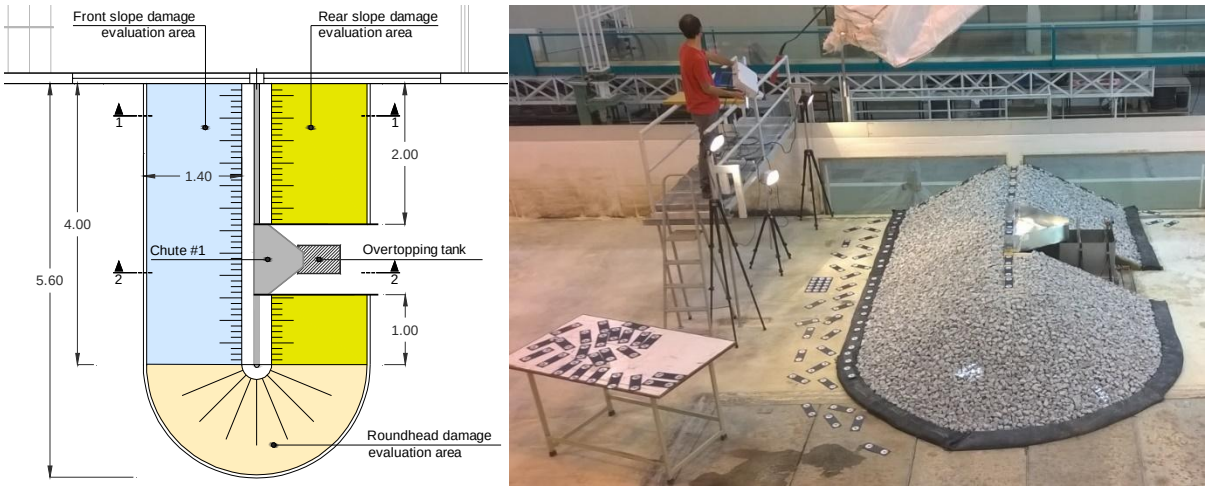

Figure 12 : Model setup in FEUP basin: (top) plan view and (bottom) damage measurement (c) cross-sectionsystems

The tests were carried out in the multidirectional wave basin of the Hydraulics Laboratory of the Hydraulics, Water Resources and Environment Division of FEUP (28.0 m long, 12.0 m wide and 1.2 m deep), which is equipped with a 12.0 m wide segmented wave-maker with active reflection absorption. A reference rubble mound breakwater was reproduced on a geometric scale of 1:35,based on coastal areas with wave conditions which are not depth-limited.

The breakwater model was 5.6 m long, 3.1 m wide and 0.68 m high, Figure 12. The armour layer was composed of a double layer of rock ($2D_{n50}$ thickness), with D_{n50} = 32 mm and D_{n85}/D_{n15} = 1.25, placed on a rubble mound core, with D_{n50} = 11.6 mm. The slope angle was 1:2. The overall crest width was 0.42 m and a 0.10 m wide superstructure was placed at its centre.

The armour was supported by a toe created using geo-bags. The breakwater core was enclosed in a mesh to avoid movement of the core materials, while maintaining the desired level of permeability (~40-50%). A 4.0 m wide trunk section was placed perpendicularly against the straight sidewall of the basin, and a semi-circular roundhead was placed at its other side. The slope angle and the armour layer thickness were equal for all trunk and roundhead sections. The armour layer on the rear side was interrupted to allow the installation of a reservoir to collect the overtopped water, allowing the measurement of the overtopping discharges and volumes. These overtopping discharges were discussed in parallel in the study of Silva et al. (2017).

The damage in the structure was measured using a stereo-photography technique (Raaijmakers et al., 2011). The structure was photographed with a set of hand-held double-cameras after draining the wave basin. Using a typical number of 50 photo pairs, point clouds of measurements were created before and after each test run. These point clouds were filtered and interpolated on a 1x1 mm grid. The post-processing steps are described in Hofland et al. (2011).

The tests performed are listed in Table 4 and a summary of the test results in Table 5. The test program included 16 test runs, including test series on the type of damage (cumulative or non-cumulative), the type of waves (long-crested or short-crested) and the water depth (h) for varying wave conditions (Cond.). All tests, except the ones indicated with SLR, were conducted for a water depth of 0.566 m. The tests with the indication SLR were conducted with a 0.023 m larger water level in order to simulate the effect of sea level rise after a few initial storms (the 60% and 80% test runs).

Table 4 : Test programme UPorto 3D tests (an X indicates a performed test). Model values.

Condition (%) H_s (cm) T_p (s) **Series**	**60%** 7.1 1.29	**80%** 9.4 1.58	**100%** 11.8 1.87	**120%** 14.2 2.18
1: classic approach	X	X	X	X
2: non-cumulative	-	X	XX	X
3: sea level rise	X	X	X +SLR	X +SLR
4: short-crested waves	X	X	X	X

The tests were carried out with irregular waves, either long or short crested. Each test consisted of 1000 waves, generated according to a standard JONSWAP spectrum (peak enhancement factor of 3.3), using the filtered white noise technique. The same temporal sequence of waves was used in the tests having the same peak wave period. In Test Series 4, short crested waves were used ($\cos^2\theta$ spreading function). The local wave steepness was set constant for all tests at $s_p = 0.03$. Hence the fictitious offshore wave steepness $s_{op} = g/2/\pi\ T_p^2$ varied between 0.027 and 0.019 for the lowest and highest wave height, respectively. The surf-similarity parameter ranged between $3.0 < \xi_{op} < 3.6$. Mainly surging breakers can be expected.

The calibration of wave conditions was done without and with the structure. The incident and reflected waves were measured with wave probes placed at a distance of one wave length from the toe of the structure. For tests with long-crested waves, an array of 4 aligned wave probes was used. For tests with short-crested waves, a group of 6 wave probes was used in a CERC6 array (Davis & Regier 1977).

Table 5 : Test results from the tests at UPorto

Series	Run	Damage	Waves	h (m)	Cond.	S	E_{2D}	$E_{3D,1}$	$E_{3D,5}$
S1	R1	Cum.	Long-crested	MHW	60%	0.1	0.02	0.94	0.12
	R2	Cum.	Long-crested	MHW	80%	1.1	0.20	1.20	0.48
	R3	Cum.	Long-crested	MHW	100%	3.4	0.49	1.57	1.06
	R4	Cum.	Long-crested	MHW	120%	12.9	1.08	1.95	1.46
S2	R1	Non-cum.	Long-crested	MHW	80%	0.6	0.11	1.12	0.43
	R2	Non-cum.	Long-crested	MHW	100%	2.6	0.27	1.23	0.82
	R2r	Non-cum.	Long-crested	MHW	100%	3.7	0.47	1.81	1.21
	R3	Non-cum.	Long-crested	MHW	120%	12.7	0.98	1.98	1.53
S3	R1	Cum.	Long-crested	MHW	60%	0.4	0.04	1.12	0.21
	R2	Cum.	Long-crested	MHW	80%	1.4	0.13	1.08	0.51
	R3	Cum.	Long-crested	MHW+SLR	100%	1.5	0.18	1.22	0.52
	R4	Cum.	Long-crested	MHW+SLR	120%	8.9	0.70	2.08	1.63
S4	R1	Cum.	Short-crested	MHW	60%	0.0	0.02	0.77	0.06
	R2	Cum.	Short-crested	MHW	80%	0.4	0.08	0.83	0.25
	R3	Cum.	Short-crested	MHW	100%	1.4	0.22	1.18	0.70
	R4	Cum.	Short-crested	MHW	120%	4.0	0.44	1.85	1.05

For a more in-depth description of the model tests it is referred to De Almeida (2017).

2D Tests at Deltares

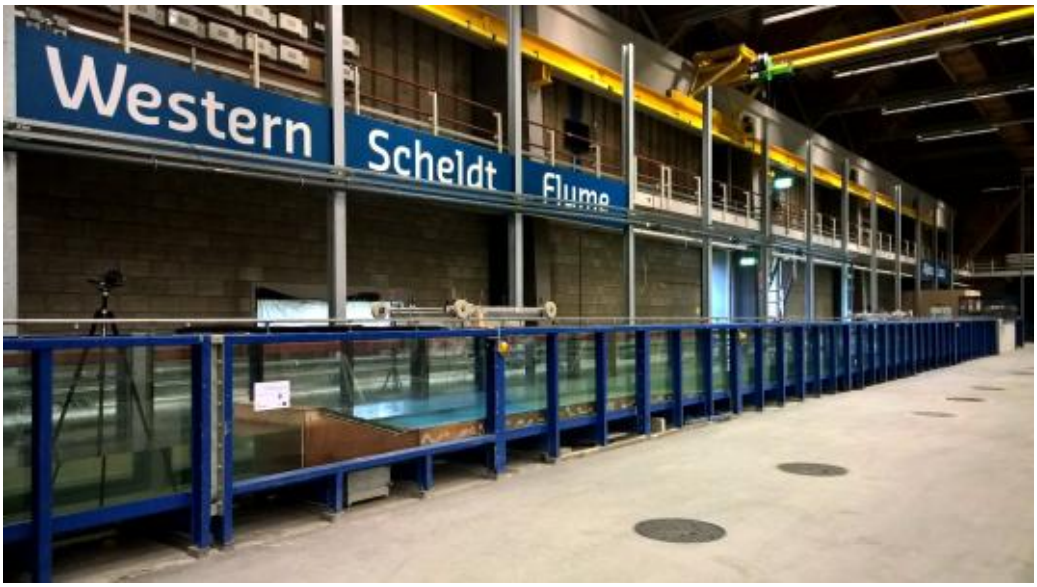

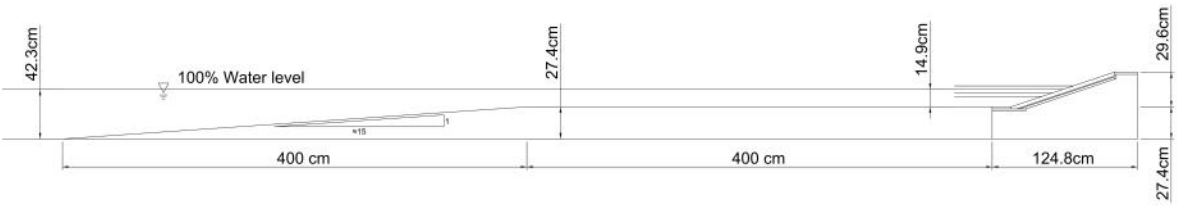

Figure 13 : Model setup in the Scheldt Flume of Deltares.(a) Overview and (b) Cross-section

The Deltares shallow water tests were carried out in the Western Scheldt Flume, and the set-up was based on shallow coastal areas with wave conditions which are depth-limited. This set-up, see Figure 13, allowed to expand the conditions tested in Uporto, including a non-overtopped rubble mound structure with an impermeable core, a 1:3 slope and a foreshore. In addition, the main particularity of these tests for shallow coastal areas is that the generated wave was equal for all test runs, and only the change in the water depth at the toe of the structure defined the incident wave height. This way, the effect of the sea level rise in the damage to the structure was clearly represented. The testing conditions included the following:

- Sea level rise scenarios (in depth-limited conditions)
- Cumulative and non-cumulative damage
- Adaptation alternatives: straight slope and four berm configurations
- Damage variability: repetition tests

During the tests, only the damage to the front slope was evaluated. Incident wave heights were depth-limited since an 8 meters long foreshore was present in this model. The model scale was 1:42 (considering reference wave climate in the Dutch Wadden sea) according to the Froude criterion. In addition, the wave generation equipment included active compensation for the reflected wave at the wave board.

The main characteristics of the model were:

- Model scale: 1:42
- Structure slope: 1:3 rock slope
- Structure total height: 0.296 m
- Structure composition: 2 D_{n50} rock armour layer over a filter and impermeable core
- Armour gradation characteristics: D_{n50}=16.3 mm and D_{n85}/D_{n15}= 1.25
- Filter gradation characteristics: D_{n50} =9.4 mm
- Water levels at toe: from 0.089 m for 60% tests to 0.179 m for 120% tests.
- Freeboards: from 0.207 m for 60% tests to 0.117 m for 120% tests.

The filter material was fixed with poli-pox glue over the impermeable core, which was built as a wooden structure. The test planning included 41 runs divided into six series briefly described below. A summary of the tested conditions are shown in Table 6, where the type of damage (cumulative or non-cumulative), the berm width (B), the berm level (d_b), the water depth at the toe of the structure (h_T), the test condition (Cond.), the generated wave height (Hs,g), the wave height at the toe of the structure (Hs,T) and the peak wave period (Tp) are described.

- Series 1: straight slope with cumulative damage (5 realizations: S1a - S1e)
- Series 2: straight slope with non-cumulative damage (5 realizations: S2a - S2e)
- Series 3: slope with a berm 10D_{n50} wide at the 100% water level with cumulative damage
- Series 4: slope with a berm 5 D_{n50} wide at the 100%water level with cumulative damage
- Series 5: slope with a berm 10 D_{n50} wide at the 80% water level with cumulative damage
- Series 6: slope with a berm 5 D_{n50} wide at the 80% water level with cumulative damage

Table 6 : Test conditions at Deltares

Series	Run	Damage	B (m)	d_b (m)	h_T (m)	Cond.	$H_{s,g}$ (m)	$H_{s,T}$ (m)	T_P (s)
S1	R1	Cum.	-	-	0.089	60%	0.087	0.037	1.27
	R2	Cum.	-	-	0.119	80%	0.087	0.050	1.27
	R3	Cum.	-	-	0.149	100%	0.087	0.062	1.27
	R4	Cum.	-	-	0.179	120%	0.087	0.074	1.27
S2	R1	Non-cum.	-	-	0.149	100%	0.087	0.062	1.27
S3	R1	Cum.	$10D_{n50}$	100%	0.089	60%	0.087	0.037	1.27
	R2	Cum.	$10D_{n50}$	100%	0.119	80%	0.087	0.050	1.27
	R3	Cum.	$10D_{n50}$	100%	0.149	100%	0.087	0.062	1.27
	R4	Cum.	$10D_{n50}$	100%	0.179	120%	0.087	0.074	1.27
S4	R1	Cum.	$5D_{n50}$	100%	0.089	60%	0.087	0.037	1.27
	R2	Cum.	$5D_{n50}$	100%	0.119	80%	0.087	0.050	1.27
	R3	Cum.	$5D_{n50}$	100%	0.149	100%	0.087	0.062	1.27
	R4	Cum.	$5D_{n50}$	100%	0.179	120%	0.087	0.074	1.27
S5	R1	Cum.	$10D_{n50}$	80%	0.089	60%	0.087	0.037	1.27
	R2	Cum.	$10D_{n50}$	80%	0.119	80%	0.087	0.050	1.27
	R3	Cum.	$10D_{n50}$	80%	0.149	100%	0.087	0.062	1.27
	R4	Cum.	$10D_{n50}$	80%	0.179	120%	0.087	0.074	1.27
S6	R1	Cum.	$5D_{n50}$	80%	0.089	60%	0.087	0.037	1.27
	R2	Cum.	$5D_{n50}$	80%	0.119	80%	0.087	0.050	1.27
	R3	Cum.	$5D_{n50}$	80%	0.149	100%	0.087	0.062	1.27
	R4	Cum.	$5D_{n50}$	80%	0.179	120%	0.087	0.074	1.27

The calibration of the wave conditions was done with the foreshore and without the structure. The incident and reflected waves were measured at two locations: at 0.5m from the toe of the structure on foreshore and at 18 m from the toe of the structure (10 m before the start of the 8 meters long foreshore). The measurement of the waves in both locations was done with 3 aligned wave probes.

For a more in-depth description of the model tests it is referred to De Almeida et al. (2017, 2018).

Table 7a presents the measured damage for each test run (S, E_{2D}, $E_{3D,1}$ and $E_{3D,5}$). These damage parameters were calculated considering the erosion of the front slope and include the total 54 D_{n50} width of the model. In addition, the damage to the configurations with a berm can be evaluated at the lower slope (which includes the horizontal berm) and the upper slope. This damage for the upper and lower slope is presented in Table 7b considering the damage parameters S and $E_{3D,5}$.

Table 7a Deltares test results

Series	Run	Damage	B (m)	d_b (m)	Cond.	S	E_{2D}	$E_{3D,1}$	$E_{3D,5}$
S1a	R1	Cum.	-	-	60%	0.2	0.07	1.03	0.18
	R2	Cum.	-	-	80%	1.3	0.13	1.07	0.31
	R3	Cum.	-	-	100%	4.3	0.45	1.46	0.66
	R4	Cum.	-	-	120%	10.9	0.83	2.00	1.25
S1b	R1	Cum.	-	-	60%	0.3	0.05	1.11	0.16
	R2	Cum.	-	-	80%	0.8	0.19	1.05	0.41
	R3	Cum.	-	-	100%	3.5	0.41	1.39	0.68
	R4	Cum.	-	-	120%	11.6	1.03	2.30	1.48
S1c	R1	Cum.	-	-	60%	0.3	0.06	1.12	0.19
	R2	Cum.	-	-	80%	0.5	0.14	1.12	0.30
	R3	Cum.	-	-	100%	3.5	0.38	1.54	0.69
	R4	Cum.	-	-	120%	11.4	0.93	1.98	1.17
S1d	R1	Cum.	-	-	60%	0.2	0.04	1.01	0.15
	R2	Cum.	-	-	80%	0.9	0.17	1.27	0.35
	R3	Cum.	-	-	100%	3.8	0.45	1.51	0.89
	R4	Cum.	-	-	120%	12.0	1.04	2.43	1.37
S1e	R1	Cum.	-	-	60%	0.3	0.11	1.10	0.16
	R2	Cum.	-	-	80%	0.9	0.15	1.22	0.36
	R3	Cum.	-	-	100%	3.2	0.35	1.36	0.71
	R4	Cum.	-	-	120%	11.0	0.99	1.94	1.27
S2a	R1	Non-cum.	-	-	100%	3.0	0.39	1.73	0.68
S2b	R1	Non-cum.	-	-	100%	4.5	0.48	1.53	0.84
S2c	R1	Non-cum.	-	-	100%	4.0	0.41	1.49	0.71
S2d	R1	Non-cum.	-	-	100%	3.3	0.35	1.32	0.74
S2e	R1	Non-cum.	-	-	100%	2.2	0.31	1.46	0.73
S3	R1	Cum.	$10D_{n50}$	100%	60%	0.1	0.03	1.13	0.18
	R2	Cum.	$10D_{n50}$	100%	80%	1.1	0.15	1.11	0.28
	R3	Cum.	$10D_{n50}$	100%	100%	2.0	0.25	1.35	0.44
	R4	Cum.	$10D_{n50}$	100%	120%	2.5	0.25	1.35	0.38
S4	R1	Cum.	$5D_{n50}$	100%	60%	0.4	0.08	0.93	0.15
	R2	Cum.	$5D_{n50}$	100%	80%	0.8	0.13	1.07	0.32
	R3	Cum.	$5D_{n50}$	100%	100%	2.9	0.51	1.40	0.81
	R4	Cum.	$5D_{n50}$	100%	120%	4.8	0.58	1.40	0.86
S5	R1	Cum.	$10D_{n50}$	80%	60%	0.7	0.11	1.09	0.22
	R2	Cum.	$10D_{n50}$	80%	80%	0.7	0.14	1.09	0.28
	R3	Cum.	$10D_{n50}$	80%	100%	0.9	0.16	1.24	0.25
	R4	Cum.	$10D_{n50}$	80%	120%	4.6	0.45	1.30	0.74
S6	R1	Cum.	$5D_{n50}$	80%	60%	0.3	0.04	0.97	0.17
	R2	Cum.	$5D_{n50}$	80%	80%	1.0	0.14	1.11	0.28
	R3	Cum.	$5D_{n50}$	80%	100%	3.2	0.31	1.35	0.68
	R4	Cum.	$5D_{n50}$	80%	120%	4.7	0.53	1.51	0.74

Table 7b Deltares test results – slope with a berm (lower and upper slope)

Series	Run	S TOTAL	S Lower	S Upper	$E_{3D,5}$ TOTAL	$E_{3D,5}$ Lower	$E_{3D,5}$ Upper
S3	R1	0.1	0.1	0.0	0.18	0.18	0.01
	R2	1.1	1.1	0.0	0.28	0.28	0.02
	R3	2.0	1.7	0.3	0.44	0.44	0.20
	R4	2.5	1.5	1.0	0.38	0.38	0.38
S4	R1	0.4	0.4	0.0	0.15	0.15	0.03
	R2	0.8	0.8	0.0	0.32	0.32	0.08
	R3	2.9	2.8	0.1	0.81	0.81	0.18
	R4	4.8	2.9	1.9	0.86	0.86	0.53
S5	R1	0.7	0.6	0.1	0.22	0.22	0.04
	R2	0.7	0.6	0.1	0.28	0.28	0.11
	R3	0.9	0.6	0.3	0.24	0.24	0.18
	R4	4.6	1.2	3.4	0.74	0.31	0.74
S6	R1	0.3	0.2	0.1	0.17	0.17	0.03
	R2	1.0	0.7	0.3	0.28	0.28	0.20
	R3	3.2	1.2	2.0	0.68	0.37	0.68
	R4	4.7	0.1	4.6	0.74	0.24	0.74

2.2.3 Results and discussion (LNEC, FEUP, Deltares tests)

The data collected during the 2D and 3D tests at LNEC, FEUP and Deltares , whose objective was to damage evolution, consisted of stereo photogrammetric surveys of the breakwater sections after each test run (e.g. Figure 14), Lemos et al. (2018), Fortes et al. (2018) and De Almeida (2017).

2.2.3.1 LNEC's results

For all the test surveys a point cloud was created and from each one profiles and surfaces were extracted to assess damage evolution, by calculating both the damage parameter (S) and the damage depth parameters, E2D and $E_{3D,1}$, $E_{3D,5}$, as proposed by Hofland et al. (2011).

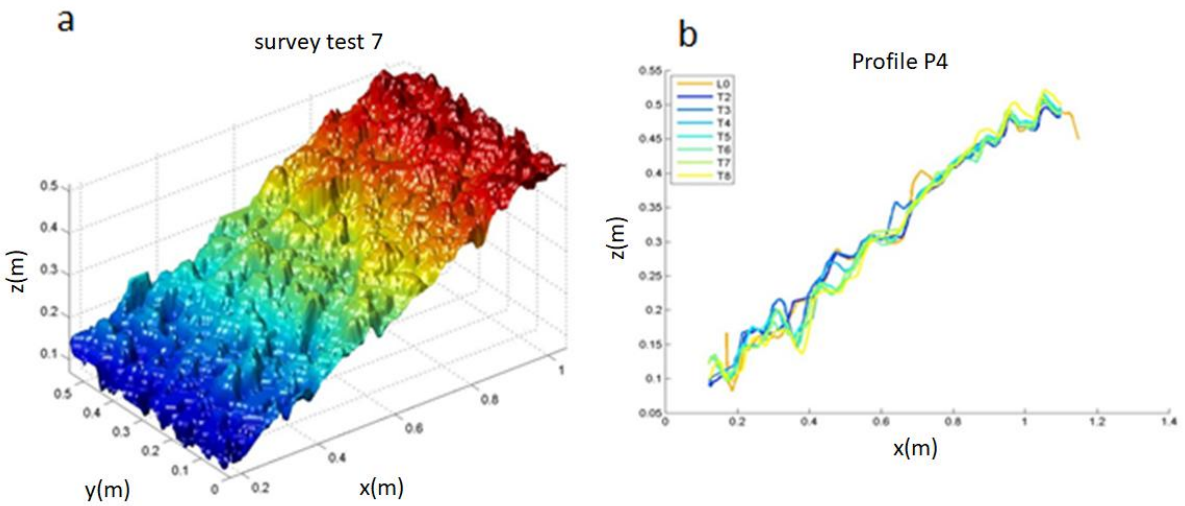

Figure 14 : a) Surface obtained from a stereo photogrammetric surveys b) Profile evolution.

Table 8 shows the damage occurred in each test for storm sequences 1-7 and 8-15 in terms of percentage of displaced blocks over the total number of blocks on the active zone, D.

Table 8 : Percentage of displaced armour units (D) for each storm sequence

1-7	Test	1	2	3	4	5	6	7	
	D (%)	3.2	4.0	4.8	5.6	7.3	9.7	10.5	
8-15	Test	8	9	10	11	12	13	14	15
	D (%)	4.0	4.8	6.5	6.5	7.3	8.9	10.5	11.3

According to the damage classification referred to in the Coastal Engineering Manual (U.S. Army Corps of Engineers, 2006), the cumulative damage at the end of the last test of each sequence corresponds to an intermediate damage (units are displaced but without causing exposure of the under or filter layers to direct wave attack). However, some differences between sequences were found in the damage.

2.2.3.2 FEUP's results

For illustration, Figure 1 and Figure 1 present results obtained in the 3D physical model tests carried out at the FEUP.

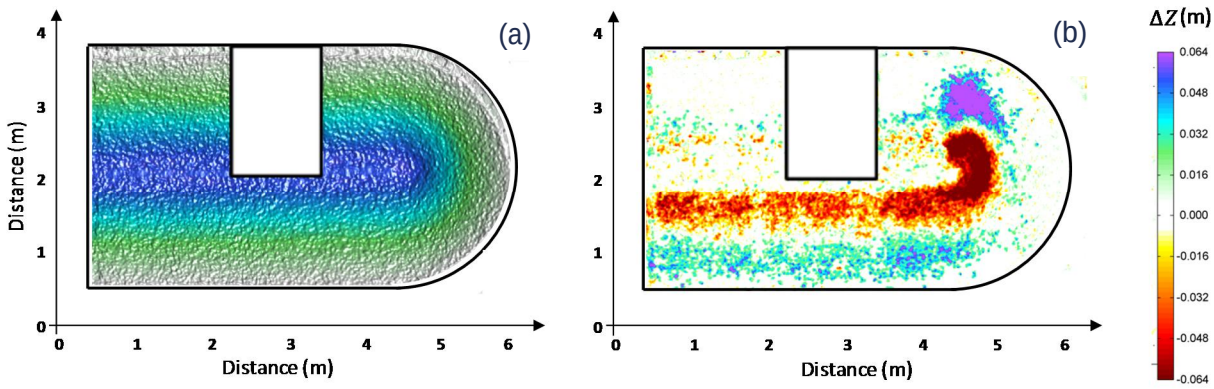

Figure 15 : Initial 3D survey of the breakwater (a) and damage after the tests for a significant wave height equivalent to 120% of the design significant wave height – cumulative damage case (b).

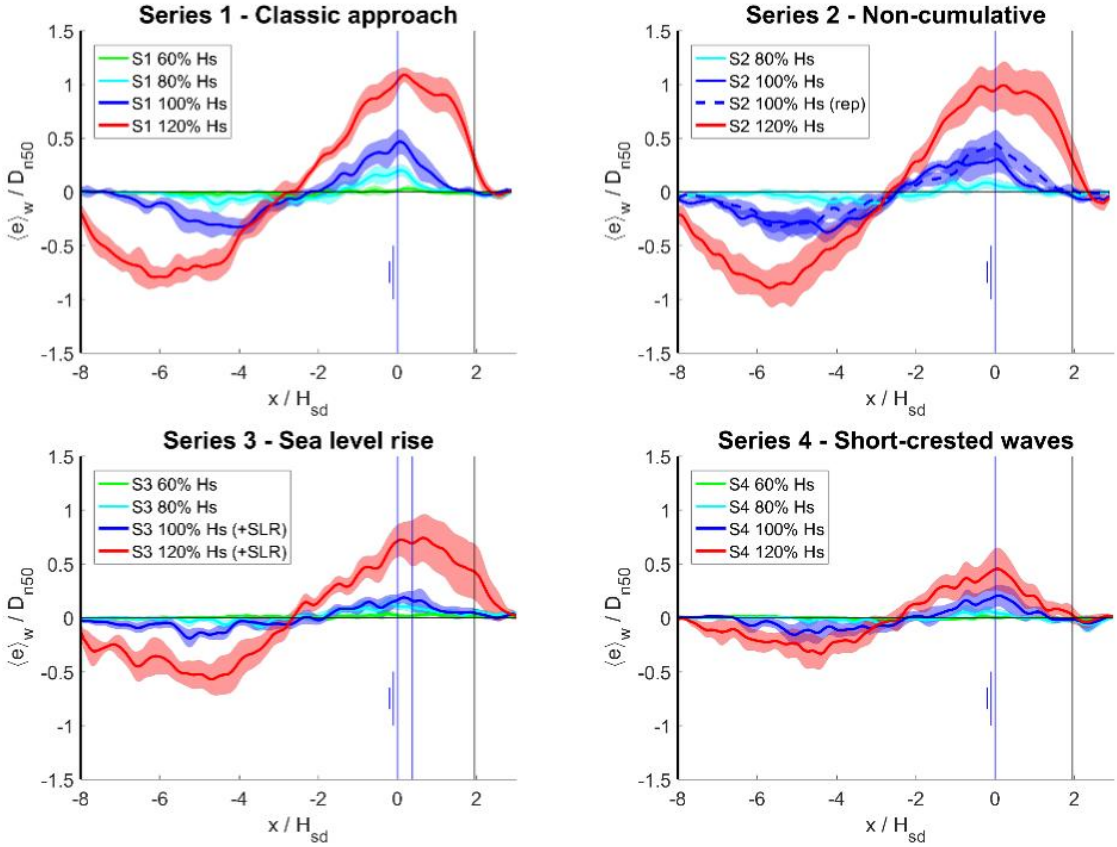

Figure 16 : Width-averaged erosion profiles for the four test series with confidence band (shaded areas). Here x is the horizontal cross-shore coordinate, with its origin at the waterline (Hofland et al., 2011).

In the experiments at FEUP, it was observed that the damage hole was deeper around the water line and that its size increased, as expected, with the significant wave height, extending up to the crest for the 120% wave condition. For the higher water level (with SLR) and equal wave height, less damage was observed in the structure. Moreover, clear differences between "cumulative damage" and "rebuilding" test series were observed. Nevertheless, it is important to mention that significant scatter was also observed in the results from tests carried out under identical conditions. It was also concluded that the damage to the trunk was lower for short-crested waves.

The results for FEUP and LNEC tests, concerning E_{2D} and $E_{3D,5}$ versus S, are depicted in Figure 17. The $E_{3D,5}$ values for the trunk section were obtained considering a circular spatial moving average of $5D_{n50}$ diameter (see definition of damage in section 2.2.2). It can be seen that these values are about two times larger.

LNEC's results, which were based on depth-limited conditions and varying wave steepness, are in good agreement with the FEUP results for waves not deep limited. Those results all follow the E_{2D} FEUP line trend. The scatter in the LNEC result is somewhat larger than of FEUP's results, probably due to the smaller width of the LNEC test section.

It can be seen that those tests give comparable values for E_{2D}, as given in Hofland et al. (2011), for the initial and intermediate damage levels. For the situation where a considerable amount of damage occurs to the crest, the allowed value of S becomes indeterminate, as it was not intended for this case (the damage area can only be determined accurately for a straight slope).

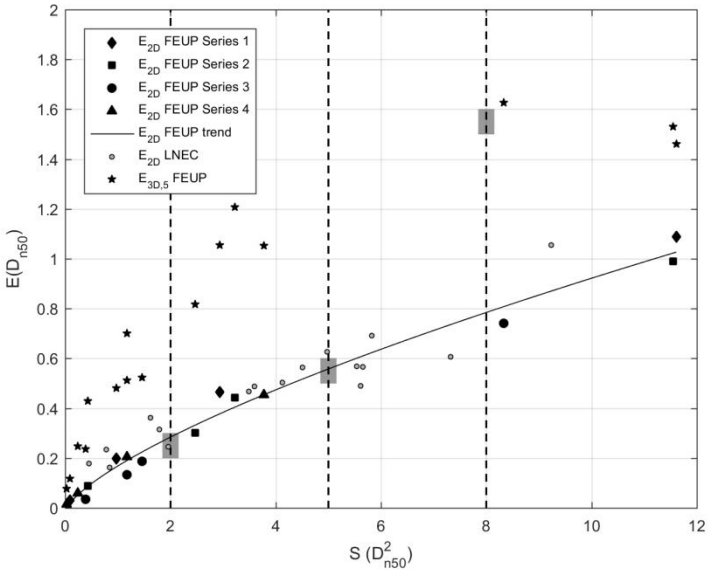

Figure 17 : E_{2D} and $E_{3D,5}$ versus S. Dashed lines and grey areas: design values of S and E_{2D}, respectively.

Please note that Broderick (1983) date) applied S = 2 (equivalent to the local damage depth, E ≈ 0.3) as start of damage, as that was the lowest discernible damage that could be measured. It can be seen that much lower damage quantities (i.e. S ≈ 0.5 or E ≈ 0.1) can be measured using the presently used high-resolution techniques and wide test section.

Incremental damage and cumulative damage

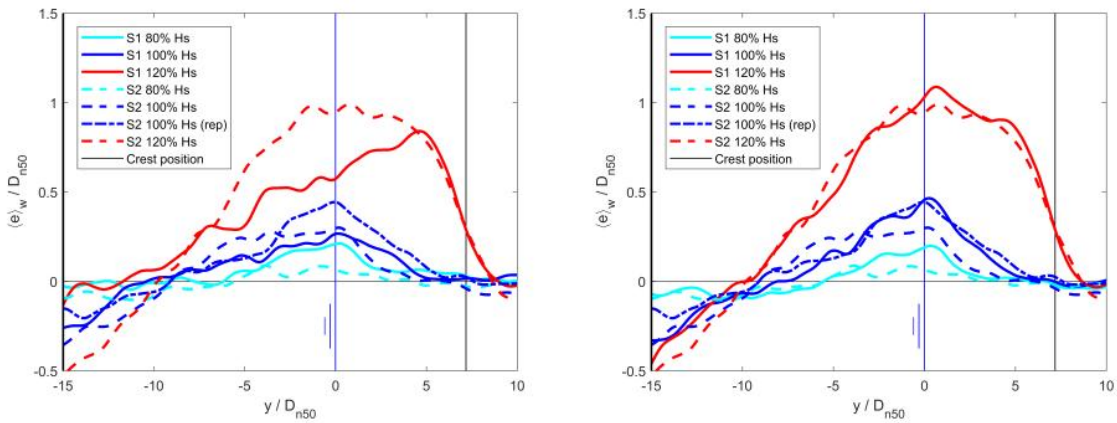

Figure 18 : UPorto tests – Analysis of cumulative (Series 1) and non-cumulative (Series 2) damage. (a) Incremental damage: compared with previous test (b) Standard damage: compared with initial conditions

In Figure 18a the non-cummulative damage results at FEUP from Series 2 are compared with the incremental damage of each test run from Series 1 (which is obtained as the damage recorded between a given test run and the previous test). In this case, it can be seen that the non-cumulative results leads to larger erosion of the rebuilt structure (Series 2), while the cumulative tests show less damage to the already damaged structure (Series 1). In contrast, in Figure 18b the non-cummulative damage results from Series 2 are compared with the standard damage of each test run from Series 1 (which is obtained as the damage recorded between a given test run and the initial conditions for the series). In this case both cumulative and non-cumulative results show similar damage. Furthermore, Deltares test results also showed small variations (from 0% to 5% in measured damage

according to both S and $E_{3D,5}$ parameters) between cumulative (Series 1) and non-cumulative (Series 2) measured damage, see De Almeida (2017). The design values for E_{2D} proposed by Hofland et al. (2011) were partly in line with the experimental results presented and were partly adjusted. The relation between S and E_{2D} did not hold true for non-standard cases, namely: short-crested waves, strongly varying water levels, curved sections like roundheads, etc. It seems better to use a local parameter like E_{2D} (or $E_{3D,5}$) when testing such a structure. The design values for $E_{3D,5}$ appeared to be roughly twice the values as those for E_{2D}. It has to be verified whether these values can be used on configurations like roundheads.

Thus, according to the UPorto and Deltares test results, both testing methods presented similar damage results for rock armoured slopes.

Damage characterization width

The validation of the most suitable characterization width for damage characterization of coastal structures was made considering the UPorto tests carried out in the wave basin and the Deltares tests carried out in a wave flume.

The influence of different characterization widths can be observed in Figure 19 for damage parameters S, E_{2D}, $E_{3D,1}$ and $E_{3D,2}$ for the UPorto tests. Similar results have been obtained for the Deltares tests (see De Almeida, 2017).

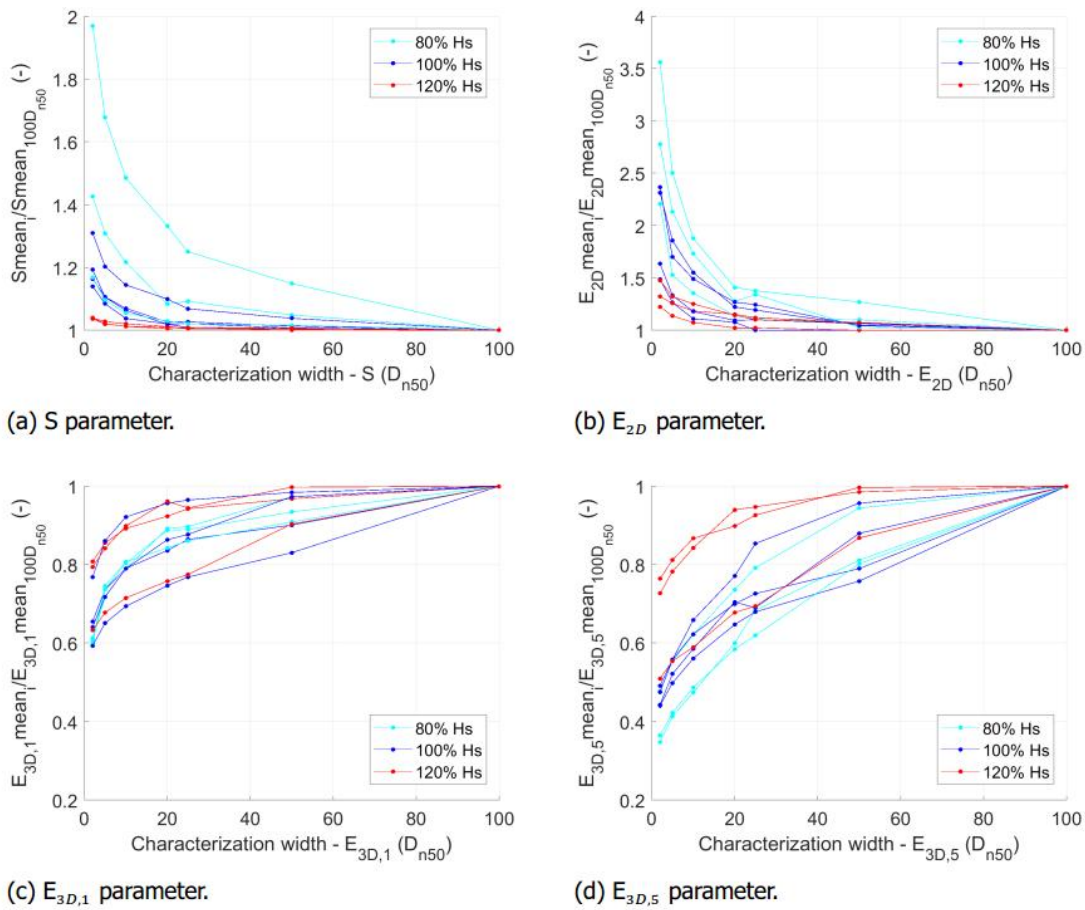

Figure 19 : Characterization width (mean damage) – Uporto test Series 1-3

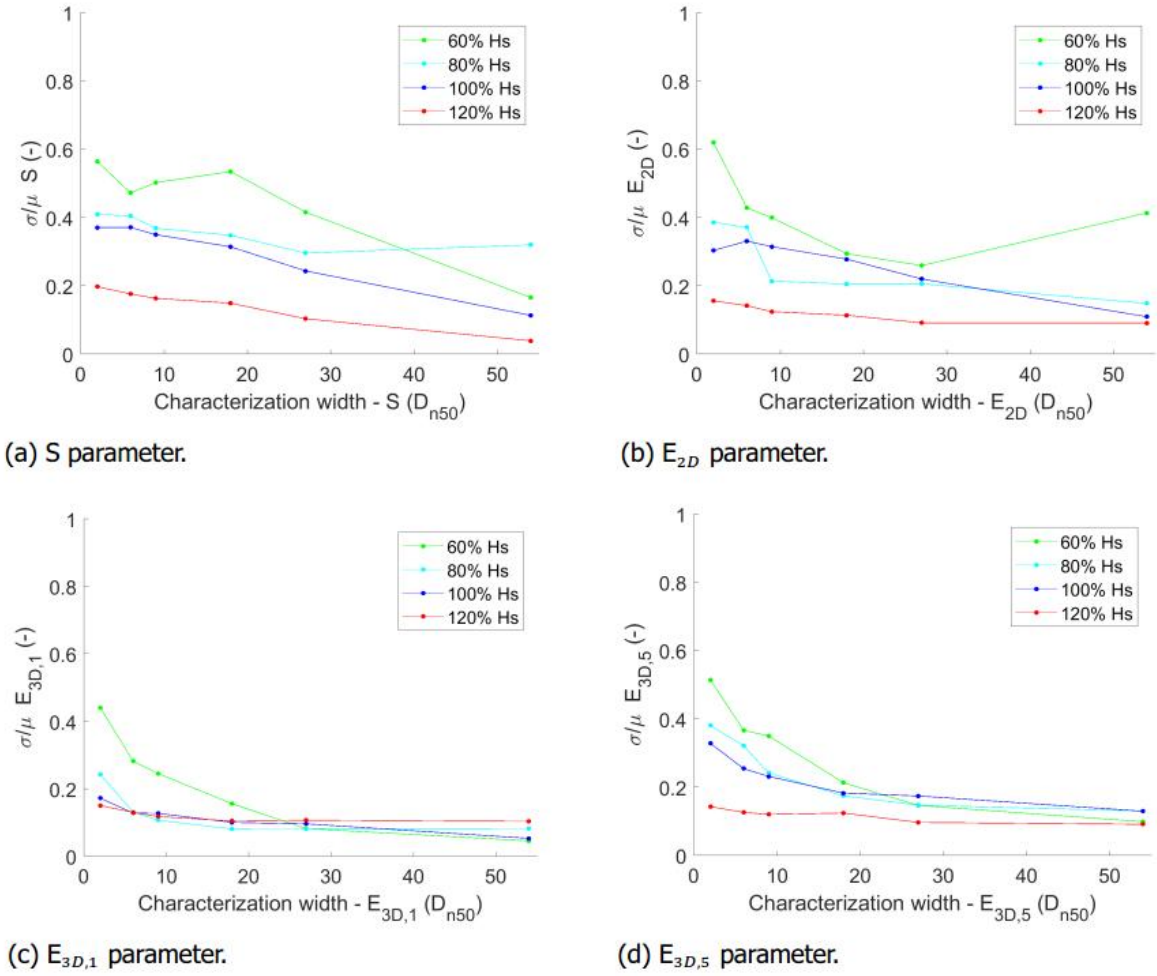

(a) S parameter. (b) E_{2D} parameter.

(c) $E_{3D,1}$ parameter. (d) $E_{3D,5}$ parameter.

Figure 20 : Standard deviation normalized by the mean – Deltares test series 1

The values for each characterization width are obtained as the average of all the values for that given width, being between 50 values for the $2D_{n50}$ width and 1 value for the 100 D_{n50}. This average damage is then normalized by the damage obtained for the 100 Dn50 characterization widths. Regarding the parameters obtained from width-averaged profiles (S and E2D in Figure 20a/b), it can be observed that the measured mean damage reduces with increased characterization width. In addition, two different behaviors for low damage and high damage conditions can be distinguished hereafter :

- High damage conditions (100% and 120%): S and E_{2D} damage parameters become increasingly stable with characterization widths larger than 25 D_{n50}, although considering wider sections will still affect the measured damage.
- Low damage conditions (80%): S and E_{2D} damage parameters do not stabilize with increased characterization widths up to widths of $100D_{n50}$. Thus, a strong characterization width effect is present in the measured damage.

Regarding the E3D,1 and E3D, 5 parameters, it can be observed that the measured damage increases with increased characterization width. For these damage parameters, there is no clear distinction

between the variation in measured damage for low and high damage conditions as observed previously for S and E_{2D} parameters.

The main observation for this damage parameter $E_{3D,m}$ is that the measured damage continues to increase with increasing characterization widths. This suggests that there is no upper limit for the damage to the structure and that when considering wider structures the probability of observing a larger extreme damage will continue to increase. This length effect for the design and characterization of coastal structures should then be taken into account. Thus, the characterization width for this parameter cannot be defined only as a recommended fixed value or limit but will be described as part of a extreme value distribution for damage to coastal structures.

Regarding the parameters obtained from width-averaged profiles of the Deltares tests, see Figure 20 (S and E2D) it can be observed that the increase in the characterization width leads to a general reduction of the variability in the measurements (although for damage parameter E2D and very small damage such as the 60% Hs conditions this pattern is not clear).

Regarding the parameters obtained as the maximum erosion depth observed within a given characterization width ($E_{3D,5}$ and $E_{3D,1}$), the influence of the characterization width in the variability of the results has less scatter than for S and E_{2D}. In these cases ($E_{3D,5}$ and $E_{3D,1}$) and for all damage conditions, there is a reduction of the variability with increased characterization width, especially after roughly $27D_{n50}$.

Comparing the behaviour of all damage parameters, it can be stated that $E_{3D,5}$ and $E_{3D,1}$ damage parameters presents a much smaller variability than S and E_{2D}. Thus, the current study supports the hypothesis that the $E_{3D,m}$ parameters can be considered as the reference for damage characterization.

In addition, Figure 21 compares the variability of cumulative and non-cumulative damage for all four damage parameters. The cumulative damage is part of Series 1 results (run 3 with 100% condition only) while non-cumulative damage is part of the single-test Series 2 results (run 1 with 100% condition). This comparison is also made based on the average deviation from the mean for each characterization width. It can be observed that, besides different damage results, both testing procedures present similar variability in the measured damage according to all damage parameters.

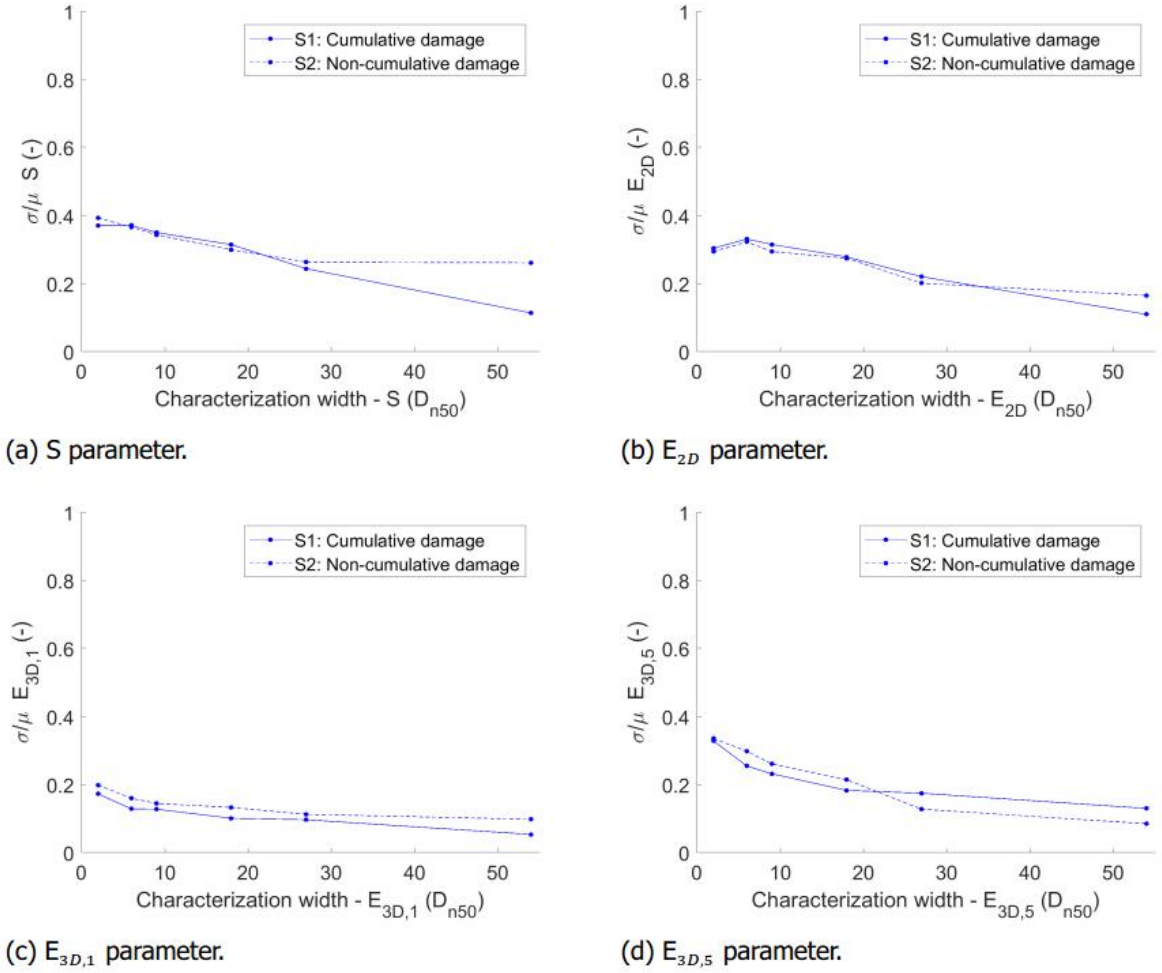

Figure 21 : Standard deviation normalized by the mean – Deltares test series 1 (100%) and Series 2.

Damage limits

The proposed damage limits for a $2D_{n50}$ thick rock armoured slopes are:

- Damage initiation: defined as the condition where a circular hole of 1 D_{n50} diameter and a depth of 1 D_{n50} are observed in the armour layer.
- Intermediate damage: defined as the condition where a circular hole of 1D D_{n50} diameter and a depth of 1.5 D_{n50} are observed in the armour layer.
- Failure limit: defined as the condition where a circular hole of 1 D_{n50} diameter and a depth of 2 D_{n50} are observed in the armour layer.

In order to characterize a given rock armoured coastal structure according to these damage limits, the parameter $E_{3D,1}$ is used as the calibration method. This $E_{3D,1}$ parameter can be described as erosion depth measured in D_{n50} perpendicular to the slope averaged over a circular area of 1 D_{n50} , which allows to capture the damage limits describe above.

A comparison with traditional failure concepts such as Thompson & Shuttler (1975) and Melby & Kobayashi (1998) is given in De Almeida (2017). In contrast, the use of high resolution surveys such as the ones provided by Digital Stereo Photography allows a more precise visualization of the state

of the structure for all damage levels: damage initiation, intermediate damage and failure. In this case all the damage limits can be quantified according to the depth and extension of the damage area.

Thus, considering the structure measurements carried out with high resolution techniques such as Digital Stereo Photography and the damage parameter E3D,1, the proposed damage limits can be defined as:

$E_{3D,1}$ damage limits:

- Damage initiation: $E_{3D,1}$ = 1
- Intermediate damage: $E_{3D,1}$ = 1.5
- Failure limit: $E_{3D,1}$ = 2

From this parameter all the damage limits are calibrated for all other damage parameters, taking into account the relations shown in Figure 22. These figures include all the UPorto and Deltares test results for all damage parameters calculated for a characterization width of 25-27D_{n50}.

$E_{3D,5}$ damage limits:

- Damage initiation: $E_{3D,5}$ = 0.3
- Intermediate damage: $E_{3D,5}$ = 0.8
- Failure limit: $E_{3D,5}$ = 1.3 (90% conf.)

E_{2D} damage limits:

- Damage initiation: E_{2D} = 0.2
- Intermediate damage: E_{2D} = 0.6
- Failure limit: E_{2D} = 1.0 (90% conf.)

S damage limits:

- Damage initiation: S = 1
- Intermediate damage: S = 5
- Failure limit: S = 12 (90% conf.)

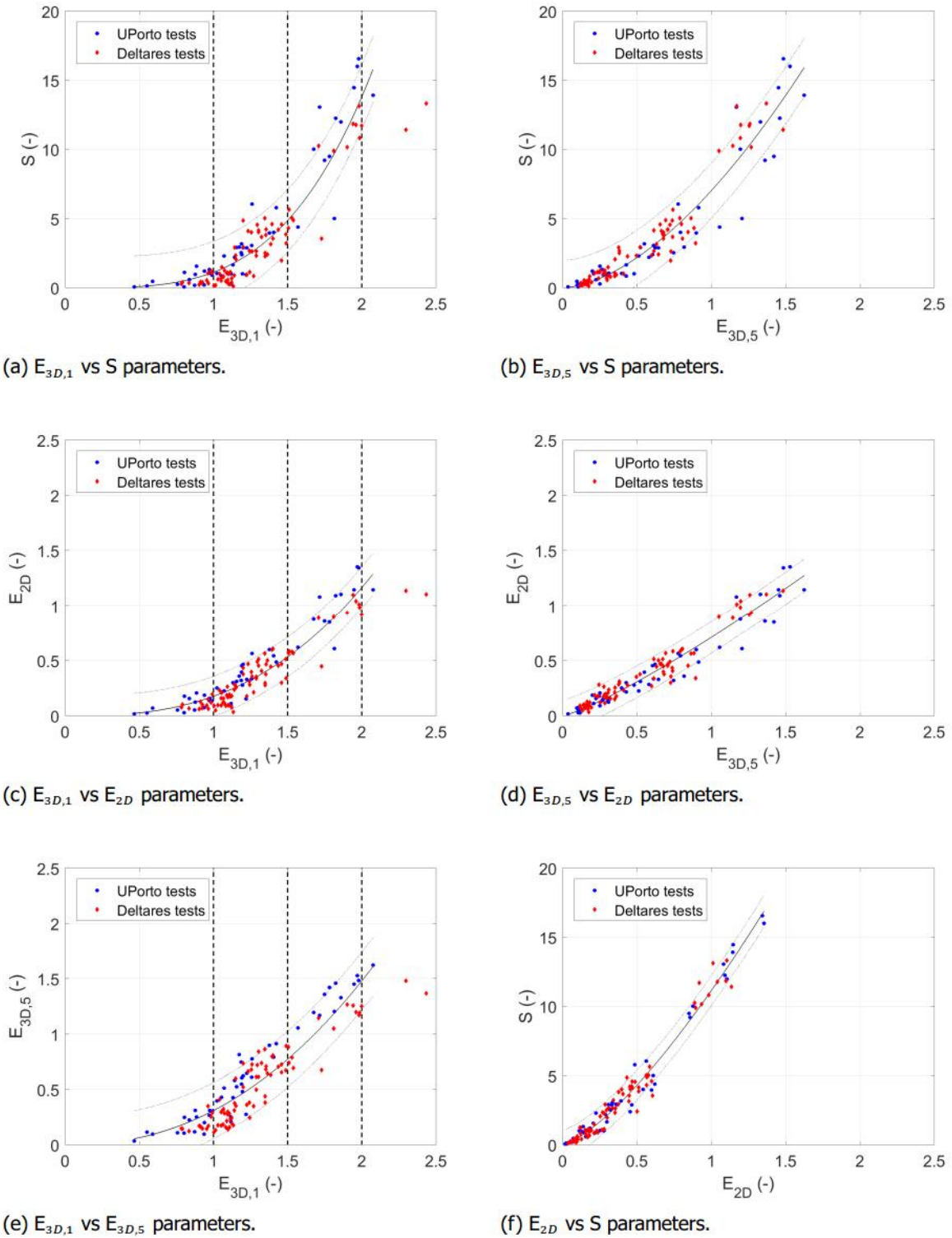

(a) $E_{3D,1}$ vs S parameters.

(b) $E_{3D,5}$ vs S parameters.

(c) $E_{3D,1}$ vs E_{2D} parameters.

(d) $E_{3D,5}$ vs E_{2D} parameters.

(e) $E_{3D,1}$ vs $E_{3D,5}$ parameters.

(f) E_{2D} vs S parameters.

Figure 22 : Comparison of all damage parameters.

An important remark from the previously defined calibrated damage limits is the fact that, according to the available data, they are constant for different slopes (1:2 in UPorto tests and 1:3 in Deltares tests). Nevertheless, this should be further investigated considering larger number of tests and different slope configurations in order to generalize these conclusions.

The found mean damage parameters, standard deviation and 80% confidence limits are given in Table 9a-d.

Table 9a: Damage parameters Deltares tests (mean values)

Parameter	S1 Run1 60%	S1 Run2 80%	S1 Run3 100%	S1 Run4 120%	S2 Run1 100% n-c
$E_{3D,1}$	1.02	1.10	1.37	2.00	1.40
$E_{3D,5}$	0.16	0.32	0.69	1.24	0.70
E_{2D}	0.09	0.18	0.43	1.00	0.42
S	0.3	0.9	3.7	11.4	3.5

Table 9b: Damage parameters Deltares tests (standard deviation)

Parameter	S1 Run1 60%	S1 Run2 80%	S1 Run3 100%	S1 Run4 120%	S2 Run1 100% n-c
$E_{3D,1}$	0.08	0.09	0.13	0.21	0.16
$E_{3D,5}$	0.02	0.05	0.12	0.12	0.09
E_{2D}	0.02	0.04	0.10	0.09	0.08
S	0.1	0.3	0.9	1.2	0.9

Table 9c: Damage parameters Deltares tests (80% confidence interval)

Parameter	S1 Run1 60%	S1 Run2 80%	S1 Run3 100%	S1 Run4 120%	S2 Run1 100% n-c
$E_{3D,1}$	±0.12	±0.13	±0.19	±0.31	±0.23
$E_{3D,5}$	±0.03	±0.07	±0.17	±0.17	±0.13
E_{2D}	±0.03	±0.06	±0.14	±0.13	±0.12
S	±0.2	±0.4	±1.3	±1.7	±1.3

Table 9d: Damage parameters Deltares tests (80% confidence interval in respect to mean)

Parameter	S1 Run1 60%	S1 Run2 80%	S1 Run3 100%	S1 Run4 120%	S2 Run1 100% n-c
$E_{3D,1}$	±12%	±12%	±14%	±16%	±16%
$E_{3D,5}$	±21%	±21%	±25%	±14%	±18%
E_{2D}	±38%	±30%	±32%	±13%	±29%
S	±60%	±43%	±35%	±15%	±38%

From Table 9 two conclusions can be drawn:

- Damage level: it can be observed that for the most energetic wave conditions (120% in Series 1 run 4), and associated larger damage levels, all parameters present small variation for the damage prediction. For the rest of the test runs and damage levels a

significant difference is observed, where damage parameters $E_{3D,1}$ and $E_{3D,5}$ leads to smaller variability while the results of E_{2D} and specially S present a large variation in the predicted damage.

- Damage parameters: it can be observed that damage parameter $E_{3D,1}$ presents the smallest variations in the predicted damage, followed by $E_{3D,5}$ with also small deviations. Damage parameter E_{2D} present reduced variability for large damages and large variations for smaller damages, while damage parameter S present also reduced variability for large damages but extremely large variations for smaller damages.

The study on the variability of damage parameters can then be summarized as follows: large damage conditions presents smaller variability in the results, while for small damage conditions the parameters $E_{3D,1}$ and $E_{3D,5}$ shows smaller variability than S and E_{2D}.

Based on the findings of this study, the damage parameter $E_{3D,5}$ is considered as the most suitable to be used as an universal damage parameter for the characterization of coastal structures based on the following considerations:

- Low bias error: the damage to the structure is clearly captured, without including hidden erosion present in the parameters that consider width-averaged profiles.
- Low random error: this parameter describes the damage to the structure with very low variability, what increases the confidence in the measured and expected damage.
- Distinguish damage range: the different states of damage to the structure can be recognized according to the limits established.
- Constant value for different structures: for all structure configurations this parameter can be used without any modification.

Current status of research

Please note that the analysis of the here reported test results is still ongoing. The analysis of the FEUP tests is restricted so far to the breakwater trunk section. The damage to the roundhead, to the rear slope and the overtopping measurements has not been analyzed so far. Furthermore, the damage parameters were only determined for the front slope. The analysis of the berm tests at Deltares (structural adaptation alternatives to sea level rise) is currently still ongoing First results are planned to be published in the CoastLab2018 Conference.

2.2.4 Recommended protocol

Damage to coastal structures consisting of rubble mound rock can be described via counting of rocks, or profile measurements. This protocol treats damage quantification by profile measurements, and more specifically high-resolution profile measurements. For the more classical techniques for measuring armour damage reference is made to manuals like the Hydralab III manual (IAHR, 2011) or the Rock manual (CIRIA et al, 2007). The knowledge in this chapter is based on Hydralab+ experiments at LNEC, UPorto, and Deltares (Hofland et al. 2017, De Almeida 2017, De Almeida et al. 2018, Van Gent et al 2018). This protocol has been written while the analysis of the tests is still ongoing; more analysis, and possibly more tests, will follow. Therefore, it is advised to use the protocol with care.

Measuring damage to structures

The high-resolution techniques discussed here typically have a resolution of 1 to 10 mm in both horizontal directions. This means that the erosion of a structure can be viewed up to the level of detail of a single stone. Typical equipment that can be used to obtain high resolution data in laboratories are terrestrial laser scanning (Rigden & Stewart, 2012; Molines et al., 2013; Puente et al., 2014) underwater laser scanners, structure-from-motion (Westoby et al., 2012, Todd et al., 2016) and stereo photography. In general, the laser scanning has the advantage over the terrestrial laser scanning that it requires less post-processing due to the fact that it directly gives measurements of elevation at all measured points (be it or not on a regular cartesian x-y grid). Nevertheless, the laser scan equipment requires some (huge) initial investment, and needs regular calibration. Stereo photography requires more post-processing (since the conversion of image-pairs to x-y-z points is an additional step), but it typically requires much cheaper equipment and the calibration can be done (sometimes automatically) during the measurement. Also the light conditions need to be controlled for a stereo-photogrammetric measurement. Both techniques have accuracies from 1 to 10 mm per point. However, since many points are averaged to obtain the (averaged) damage numbers, the random error decreases as the number of points increases, and therefore the accuracy of the end result can be significantly improved.

The employed stereo-photogrammetric techniques can be used while a (still) water layer is present in the flume or basin (Raaijmakers et al., 2012; Lemos and Santos, 2012).

Damage numbers

Damage to rubble mound structures is classically based on either the number of rocks that are displaced during a test /storm (damage number N_{od}, i.e. the number of displaced units per width D_n across the armour face), or by the area of the cross-section of the damage hole (non-dimensional erosion area $S= A_e/D_{n50}^2$, Broderick, 1983). Modern scanning methods can be used to obtain the latter type of damage definition, but also to obtain local damage estimates. Melby & Kobayashi (1998) give various approaches to describing damage to a trunk cross-section. The characteristic dimensions of a 2D (trunk) erosion hole are made dimensionless by the nominal rock diameter, D_{n50}. Besides the damage parameter, S, they also calculate the dimensionless erosion depth. Hofland et al. (2011, 2014) propose the local damage depth, E, which is different than the erosion depth of Melby & Kobayashi (1998) due to the inclusion of a spatial filter (circular moving average) of the erosion pattern, such that it is applicable to a variety of non-standard 2 and 3-D rubble mound structures.

Quantitative damage numbers can be obtained from high-profile measurements of the rubble mound structure elevation before (z_{before}) and after (z_{after}) a test run or test series:

$$S_m = \frac{\langle e \rangle_{w=mDn50}}{D_{n50}}$$

$$E_{2D,m} = \frac{max_x(\langle e \rangle_{w=mDn50})}{D_{n50}}$$

$$E_{3D,m,n} = \frac{max_{x,y}(\langle e \rangle_{R=nDn50})_{w=mDn50}}{D_{n50}}$$

where the (always positive) local erosion depth is defined as $e = max[\,(z_{\text{before}} - z_{\text{after}})cos\alpha\ ;\ 0\,]$, α is the structure slope, $\langle\ \rangle_{w...=}$ is a spatial average over the width of a flume (in the alongshore direction), $\langle\ \rangle_{R=...}$ is a (moving) spatial average over a circular area with radius R, m and n are integers, and Dn50 is the nominal diameter of the armour rock for which 50% of the rock mass is smaller. max_x is a maximum over the (cross-shore) x-direction and $max_{x,y}$ is a maximum over an area spanning the alongshore and cross-shore horizontal area.

Characterization extent

The spatial extent over which the damage numbers are averaged determines the accuracy of the result, which is discussed further below. The advised characteristic extent over which the scans should be taken (averaged) are, for the 2D damage numbers, a width greater than $20D_{n50}$ (m=20). Larger averaging widths reduce the scatter and bias in the measured 2D damage numbers. Repeated tests (with rebuilding of the damage) can be used to effectively increase the tested width, so the averaged profiles of two tests with a $20D_{n50}$ width are expected to be equivalent to one test with a $40D_{n50}$ width.

For the 3D damage parameter, E3D, a characterization width larger than $20D_{n50}$ (m=20) is also recommended. For the radius over which the spatial moving average is done, a value of $5D_{n50}$ is proposed for investigating a rubble-mound breakwater. If a larger size is used, this will potentially decrease the determined damage, such that no real damage is measured. If the averaging area is decreased, the measured values will increase, but the scatter in the results will increase as well. However, it will typically be applied in situations with dissimilar conditions along the coast which means that the chosen extent should be selected with care.

Normative values

In e.g. CIRIA et al. (2007), damage levels (, S), are proposed for certain structure types, such as 'initial damage' and 'failure'. These design values are different for each slope angle that is used. These are given in Table 10 below for a 1:2 slope. The normative damage depth values that were found in the HYDRALAB+ tests are also given in Table 10 for comparison. The normative numbers that are proposed below are based on a $25D_{n50}$ wide 2D structure. Hofland (2011) suggests that E_{2D} will give constant design values for different slopes.

Table 10 : Suggested design values for damage parameters of rock armoured rubble mound breakwaters

Damage state	S (cot**α**=2)	E_{2D}	$E_{3D,5}$
initial	1	0.2	0.3
intermediate	5	0.6	0.8
failure	12	1.0	1.3

Accuracy of damage numbers

For the 2D profile damage numbers De Almeida (2017) shows that the calculated damage number E_{2D} and S can have a positive bias of 10% to 20% for an averaging width of roughly $20D_{n50}$. This means that with larger characterization widths the measured damage will continuously decrease. The random error (scatter) in the measured damage decreases when a larger characterization width is applied.

An important finding of De Almeida et al. (2018) is that the damage parameter E_{3D} measured along a long trunk section (or with many repeated measurements) has an extreme value distribution. This means that when the measurement section is increased, typically a larger damage number is measured – just as on a real breakwater the probability of damage will increase when the structure becomes longer. Thus, for these parameters a characterization width larger than 20 D_{n50} is also recommended but associated with an extreme value distribution.

Non-standard and 3D structures

In order to cope with climate change and sea level rise induced issues, Burcharth et al. (2014) envisage that coastal structures can be adapted in a variety of ways, by adding extra layers, berms (Van Gent, 2013) or detached submerged breakwaters, or by increasing the crest levels. These and other adapted structures will have to be evaluated for their main functions, which usually comprises damage measurements (stability). For the trunk sections of these adapted structures that do not consist of a straight slope with a standard armour layer thickness, the damage parameter E_{2D} might be applied as it gives a local damage number. For sections where the hydraulic attack or structural properties change over the alongshore direction (e.g. a curve or a roundhead), the parameter E_{3D} might be applied. It is still unclear how the characterization width must be chosen for these conditions, but the values in the table might serve as a first indication of the allowed damage. On a roundhead, the area with the largest attack can be rather small, such that the characterization width is also rather small, so repeated tests are advised. The allowed damage that was found for roundheads was in the same order as given for E_{3D} in the table (Hofland *et al.*, 2014).

Test sequencing (rock)

Tests with increasing wave conditions of 60%, 80%, and 100% were conducted (Hofland et al., 2017), resulting in a cumulative damage build-up (no rebuild in between test). Additional tests were performed with a newly built slope. In these tests with the usual, increase in wave height in consecutive tests, no significant difference was found in damage profile between the test with an initial straight slope and with cumulative damage. Although further corroboration is required, it indicates that for a rock slope where the stability is obtained by gravity on the single elements (and no interlocking) the maximum tested wave condition is decisive.

2.3 OVERTOPPING EVENTS IN BREAKWATERS: COMPARISON OF 2D PHYSICAL EXPERIMENTS AND EMPIRICAL FORMULAE

2.3.1 Objective description

Reliable prediction of wave run-up/overtopping and structure damage is a key task in the design and safety assessment of coastal and harbor structures. Run-up/overtopping and damage figures should be below acceptable limits, both in extreme and in normal operating conditions, to guarantee the stability of the structure and the safety of people and assets, both on the structure and behind the structure. The mean-sea-level rise caused by climate change and its effects on wave climate may increase run-up/overtopping events and make the existing coastal and harbour structures more vulnerable to damage. Accurate estimates, through physical modelling, of the statistics of overtopping waves for a set of climate change conditions, are needed.

The use of physical (scale) models allows the simulation of extreme events as they are now, and as they are designed to be under different climate change scenarios. The experimental work developed at LNEC within HYDRALAB+, TASK 8.2 of RECIPE, entitled "Damage characterization under variable and unsteady test conditions", considers 2D damage and overtopping tests for a rock armor slope, with four different approaches to represent storms: a standard cumulative storm build-up (with increasing wave heights) with increasing water level; a standard cumulative storm build-up with a constant water level; a constant wave period; and a standard storm build-up, with a constant water level and with rebuilding.

A comparison of measured (using physical model tests) and predicted (using empirical formulae) mean overtopping discharges and individual overtopping volumes at a given cross-section of a rubble mound breakwater were performed (Mendonça et al, 2017a,b,c, 2018).

2.3.2 Tests and experiments

LNEC´s experiments were performed at the Ports and Maritime Structures Unit (NPE) of the Hydraulics and Environment Department of LNEC, in a wave flume (COI 1) approximately 50 m long, with an operating width of 80 cm and an operating water depth of 80 cm.

The flume is equipped with a piston-type wave-maker that combines both irregular wave generation and dynamic absorption of reflected waves through the use of two wave gauges located in front of the paddle (AWA0 & AWA1, in Figure 23). Ten additional resistive-type wave gauges were deployed along the flume and an additional gauge was placed on the model armour layer slope to measure run-up levels. Data acquisition of surface elevation of all 13 gauges was made at a frequency of 25Hz.

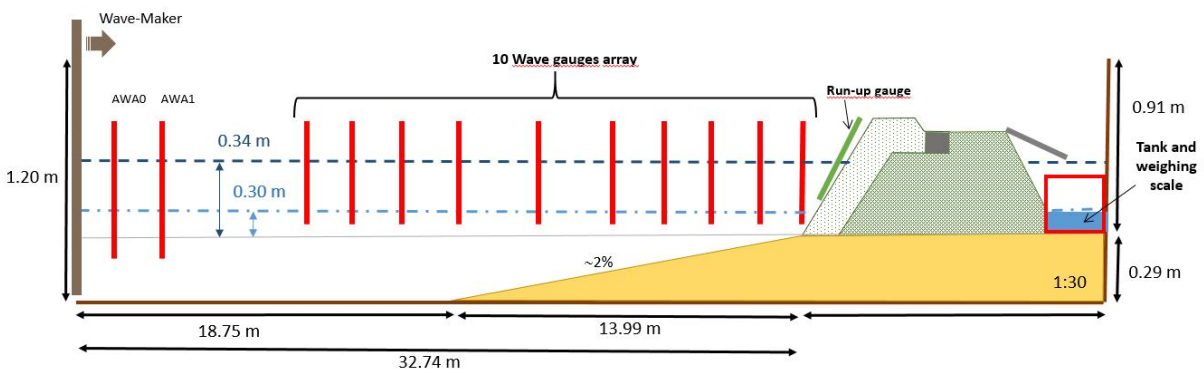

Figure 23 : Sketch of the experimental setup in the wave flume (dimensions for a 1:30 scale and for the minimum and maximum water levels).

The equipment used to collect the overtopping water consisted on a tank, located at the back of the structure. The water was directed to the tank by means of a 40 cm wide chute. The overtopping tank was placed over a weighing scale (KERN KXS-TM), which also allowed the measurement of the overtopping variation to be taken. The measured data was collected at a frequency of 1Hz (Figure 24).

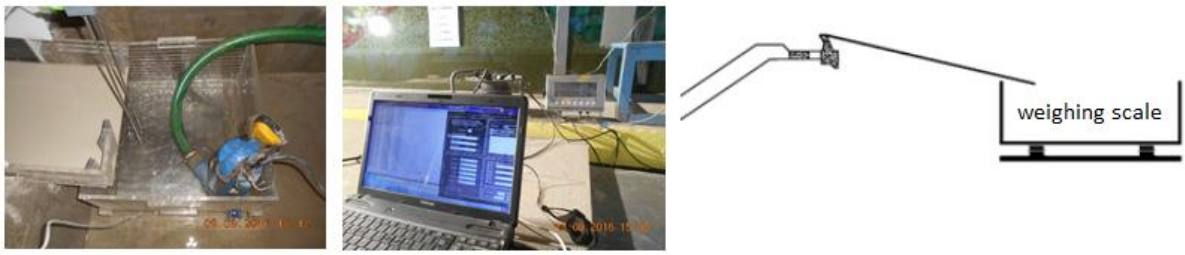

Figure 24 : Setup for overtopping measurement.

The breakwater model was built and operated according to Froude's similarity law, with a geometrical scale of 1:30, to ensure reduced scale effects (wave heights should lead to values of the Reynolds number Re>3x10^4). The breakwater cross-section at prototype scale is presented in Figur.

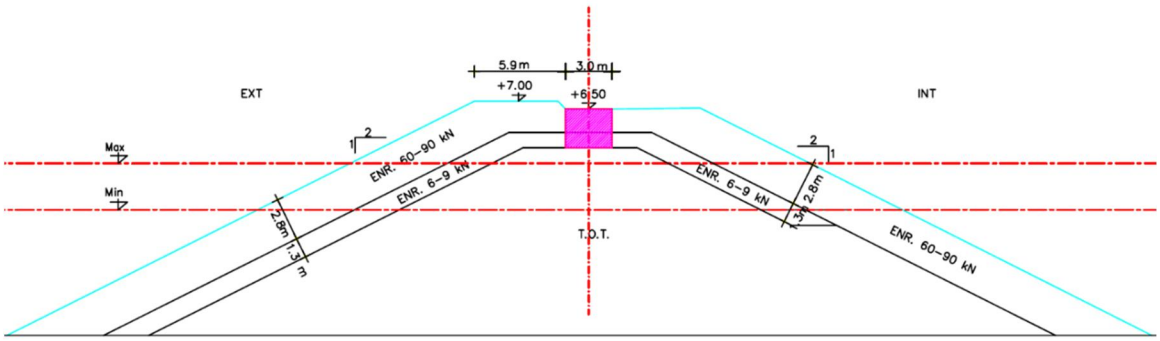

Figure 25 : Breakwater cross-section at prototype scale (natural seabed at -8.1 m (CD)).

Two-dimensional damage and overtopping tests for a rock armour slope were performed to represent four approaches: A) a standard cumulative storm build-up (with increasing wave heights) with increasing water levels; B) a standard cumulative storm build-up with a constant water level; C) a constant wave period; and D) a standard storm build-up, with a constant water level and with rebuilding.

Reproduction of the irregular wave tests used a JONSWAP spectrum, whose shape was characterized by a peak enhancement factor of 3.3. Test durations were 1980 s, 2160 s and 2400 s for peak periods of 10 s, 11 s and 12 s, respectively (as to produce approximately 1000 waves per test). For consistency, all tests were repeated at least three times.

The nominal test conditions are presented in Table , where H_s refers to the significant wave height at the toe of the structure and T_p is the peak wave period. Tests 1-7 represent approach A; tests 1-3 and 4-7 represent approach B; tests 1-3, 4-7 and 8-15 represent approach C; and tests 4-7, with rebuilding, represent approach D.

Table 11 : Nominal test conditions at structure toe.

Test	Prototype			Model		
	Water Depth, d (m)	T_p (s)	H_s (m)	Water Depth, d (m)	T_p (s)	H_s (m)
1	9.1	10	3.2	0.30	1.83	0.11
2	9.1	10	3.7	0.30	1.83	0.12
3	9.1	10	4.2	0.30	1.83	0.14
4	10.1	11	3.7	0.34	2.01	0.12
5	10.1	11	4.2	0.34	2.01	0.14
6	10.1	11	4.7	0.34	2.01	0.16
7	10.1	11	5.2	0.34	2.01	0.17
Rebuilding						
8	11.1	12	3.7	0.37	2.19	0.12
9	8.1	12	3.7	0.27	2.19	0.12
10	11.1	12	4.2	0.37	2.19	0.14
11	8.1	12	4.2	0.27	2.19	0.14
12	11.1	12	4.7	0.37	2.19	0.16
13	8.1	12	4.7	0.27	2.19	0.16
14	11.1	12	5.2	0.37	2.19	0.17
15	8.1	12	5.2	0.2	2.19	0.17

2.3.3 Results and discussion

The physical experiments resulted in a data set containing mean overtopping discharges values for around 80 experiments. Different wave conditions were assessed and the total and individual overtopping volumes were analyzed and compared with existing empirical prediction methods (EurOtop, 2016). Main results are presented in Mendonça et al. (2017a, b).

Figur shows the computed and the measured non-dimensional mean overtopping discharges, $q/(gH_{m0}^3)^{0.5}$, versus the non-dimensional freeboards, R_c/H_{m0}, for test conditions 2 to 6 (note that for test 1 no overtopping events were determined). The computed values have been obtained both using the mean discharge equation (with the mean of the roughness factors of the tests, $\gamma_{f\,mod} = 0.544$; continuous line) and the 90%-confidence band (dotted lines) suggested in EurOtop (2016). The figure shows that the empirical formula provides good predictions of the mean overtopping discharges measured in the experiments, with all data points falling within the 90% confidence band of the empirical formulae. For values of $q/(gH_{m0}^3)^{0.5} < 10^{-5}$ the predictions are less reliable and correspond to mean overtopping discharges less than 0.5 l/s/m (test 2), for which some scale effects are usually expected.

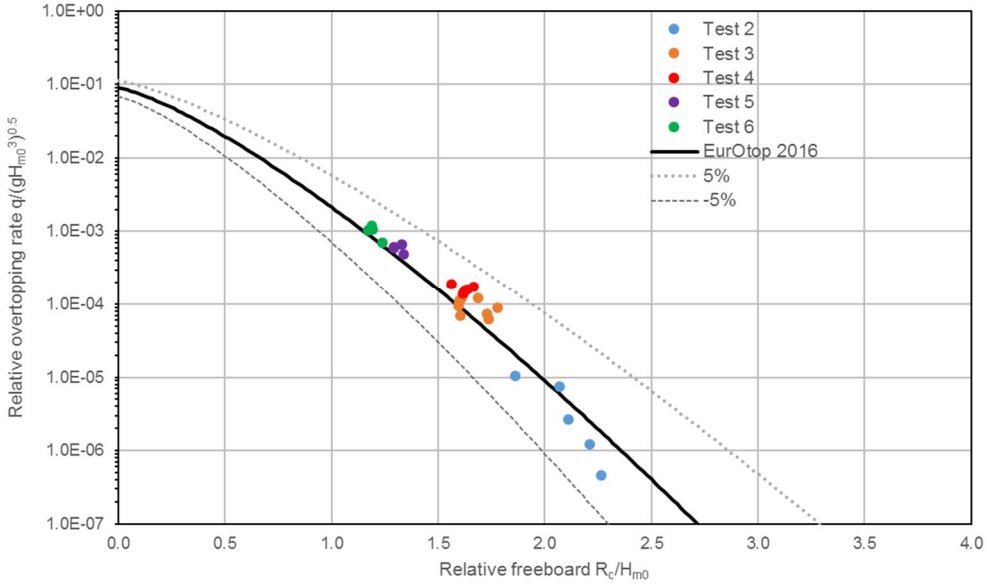

Figure 26 : Computed (mean discharge equation obtained with $\gamma_{f\ mod} = 0.544$ and 90%-confidence band; EurOtop, 2016) and measured non-dimensional mean overtopping discharges, $q/(gH_{m0}^3)^{0.5}$, versus non-dimensional freeboards, R_c/H_{m0}, for test conditions 2 to 6.

The individual overtopping volumes, V_i, measured for each test are shown in Figure , non-dimensional overtopping volume (individual volume divided by the average of the individual volumes of the test), $V_i/V_{average}$, is plotted against probability of non-exceedance of each individual volume in the test (relative to the number of waves), P_{ov}. Figure shows that the probability that the maximum individual volume is not larger than approximately eight times the average of the test volumes is 100%.

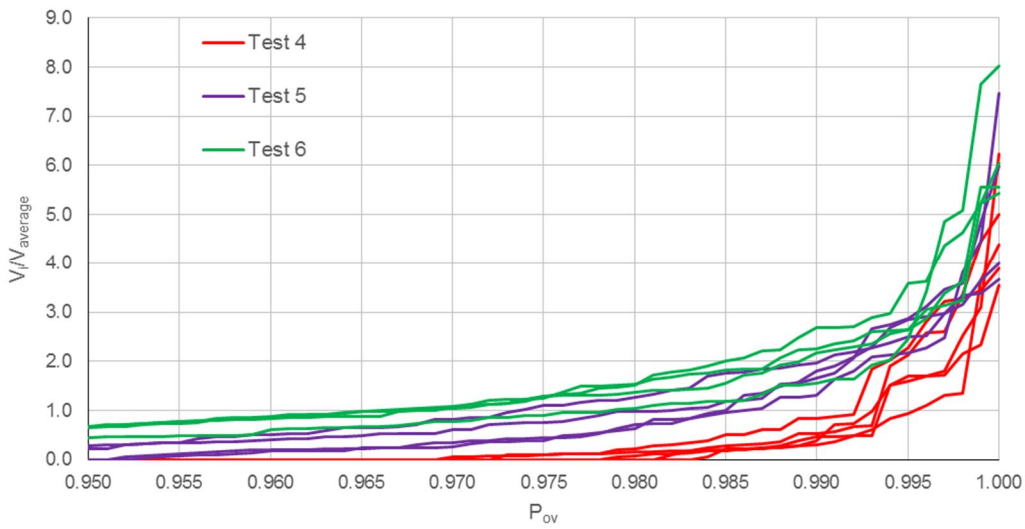

Figure 27 : Measured non-dimensional individual overtopping volumes, $V_i/V_{average}$, versus the probability of non-exceedance, P_{ov}, for test conditions 4 to 6.

Figure 28 shows computed and measured Weibull shape factors, b, for rubble mound structures versus non-dimensional mean overtopping discharges, $q/(gH_{m0}T_{m-1,0})$. It shows that for a relative discharge $q/(gH_{m0}T_{m-1,0}) < 5\text{x}10^{-5}$ the average value of b is about 0.85, with almost no scatter in the

data, suggesting that a *b* value of 0.85 can be used to describe overtopping of individual wave volumes. Data are in close agreement with the computed values of *b*.

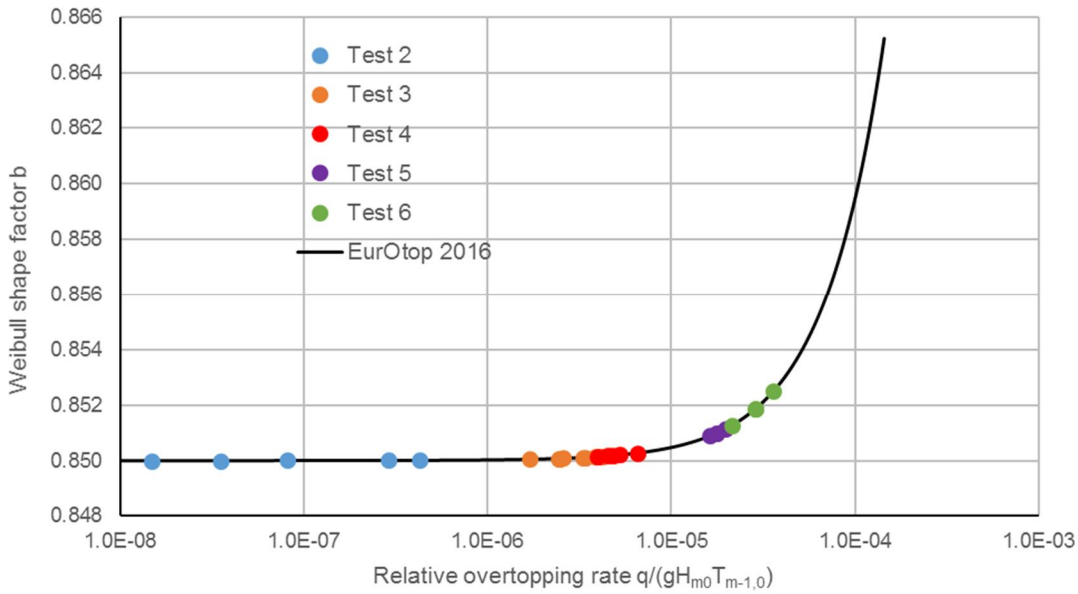

Figure 28 : Computed (Eq. 5; EurOtop, 2016) and measured Weibull shape factors, b , for rubble mound structures versus non-dimensional mean overtopping discharges, $q/(gH_{m0}T_{m-1,0})$.

Figure gives computed and measured percentage of overtopping waves versus the non-dimensional crest height, A_c*D_n/H_{m0}^2. The test data are in good agreement with the empirical prediction given by the EurOtop Manual (EurOtop, 2016). However, the presented tests (Tests 4, 5 and 6) cover a limited range of overtopping percentages, with maximum values of about 9%.

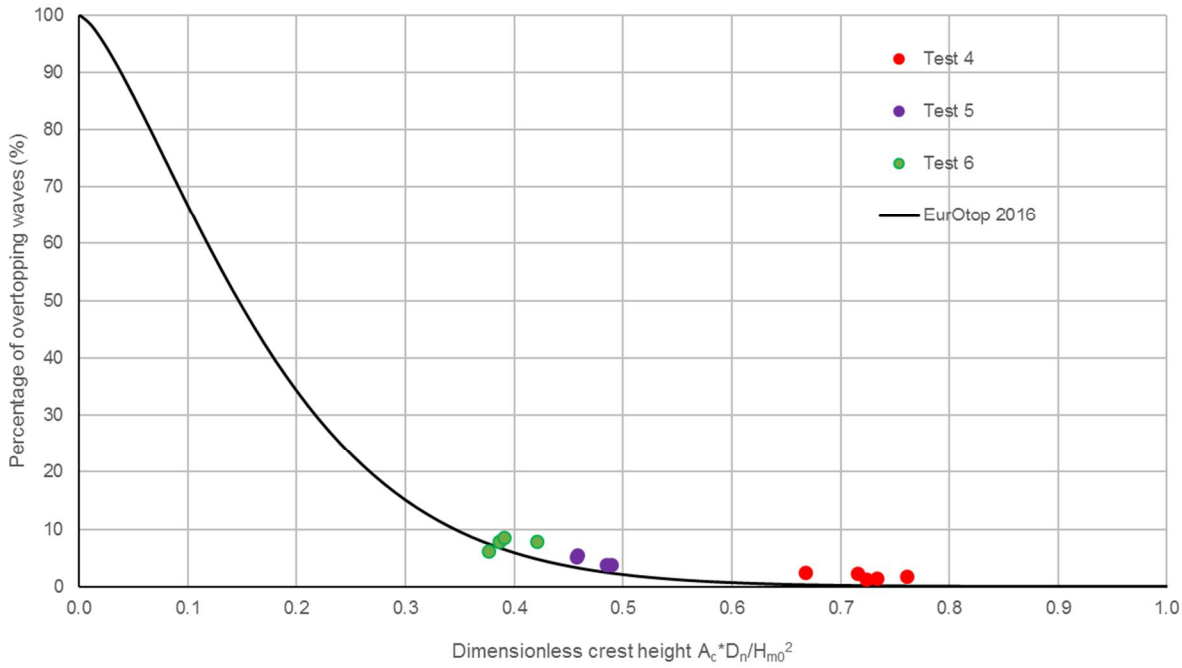

Figure29 : Computed (EurOtop, 2016) and measured percentage of overtopping waves, P_{ov}, for rubble mound breakwaters versus relative (armor) crest height and armor size ($R_c \leq A_c$).

2.3.4 Recommended protocol

To study run-up and overtopping events in breakwaters, the following steps should be examined:

1. Model scale ratios

The largest possible model scale must be selected for the available flumes to ensure that the dominant forces are well represented (consideration of Froude scaling or others, as Reynolds and Weber).

2. Selection of representative sea states

The specification of sea states should be determined based on statistical analysis of wave conditions at the site and consideration of the test objective, considering the same total return period.

Two-dimensional damage and overtopping tests for a rock armor slope, to represent climate change scenarios, can be represented considering the following approaches:

A) a standard cumulative storm build-up (with increasing wave heights) with increasing water level;
B) a standard cumulative storm build-up with a constant water level;
C) a constant wave period; and
D) a standard storm build-up, with a constant water level and with rebuilding.

The parameters - significant wave height (H_s) and peak wave period (T_p) - were considered at the toe of the structure.

A JONSWAP spectrum, with a peak enhancement factor of 3.3, is used for the irregular wave tests.

3. Duration of time series

Analyzing damage and overtopping under climate change scenarios may imply the implementation of longer time series to ensure that the low frequency band of the spectrum (associated with long waves) is well represented, as to obtain enough information to derive design values, i.e. values with a well-defined probability, since the rate of overtopping can greatly vary within the sequence.

Previous tests by Reis et al. (2008) and Romano et al. (2015) suggest that for rubble mound breakwaters mean overtopping discharges can generally give a stable prediction from tests of only 500 waves. Reis et al. (2008), however, remind us that information obtained from only a single test is limited, as mean discharges will vary even for the same wave and structure characteristics. Tests repetition should be performed.

Sounder information on mean discharge may be given by deploying several short duration tests with different time series rather than using a single long duration test.

Having this in mind, LNEC's test durations were 1980 s, 2160 s and 2400 s for peak periods of 10 s, 11 s and 12 s, respectively (which reproduced approximately 1000 waves). All tests were repeated at least three times to provide reliable, robust estimates of the structure´s load/response.

4. Absorption system

Breakwaters are highly reflective when exposed to long (and short) waves and active absorption systems (absorbing wave-makers) can assist reducing re-reflection of waves on the wave-maker, and consequently, changing the wanted wave regime one wants to impinge the structure. For these kind

of tests, an active absorption system should be always considered. In LNEC's tests, the AWASYS active wave absorption system was used.

5. Wave run-up and overtopping

Wave run-up should be assessed through use of resistive-type wave gauges or step-gauges (pressure sensors embedded in the mound slope) and photographic techniques.

Wave overtopping should be assessed by collecting the overtopping water in overtopping trays or tanks and measuring the overtopped water volume or mass: mean overtopping and individual overtopping.

For each test, mean overtopping should be measured, considering the total volume of overtopped water, per time and per width of the tray, $m^3/s/m$, plotted as in Figure 26.

Moreover, it is also quite important to assess the number of overtopping events with a wave gauge at the crest of the breakwater (Figure 24 : 24) or by continuous water level measurements (volume or mass) within the overtopping tray (Figure 30).

The wave gauge installed in the tank to identify each overtopping wave, must remain submerged throughout the test.

Attention should be paid to the process of emptying the tank where the water is weighted. Since, for some wave conditions, the tank will be filled several times in a test, a pump, placed in the tank, will pump the overtopped water to additional tanks placed next to the flume. These tanks can be used to confirm the total overtopped water in each test.

The measurement of the individual overtopping (V_i) was measured identifying the increments of water in time (on Figure 30) and the average of the individual volumes of the test is then calculated. Non-dimensional overtopping volume (individual volume divided by the average of the individual volumes of the test), $V_i/V_{average}$, is calculated.

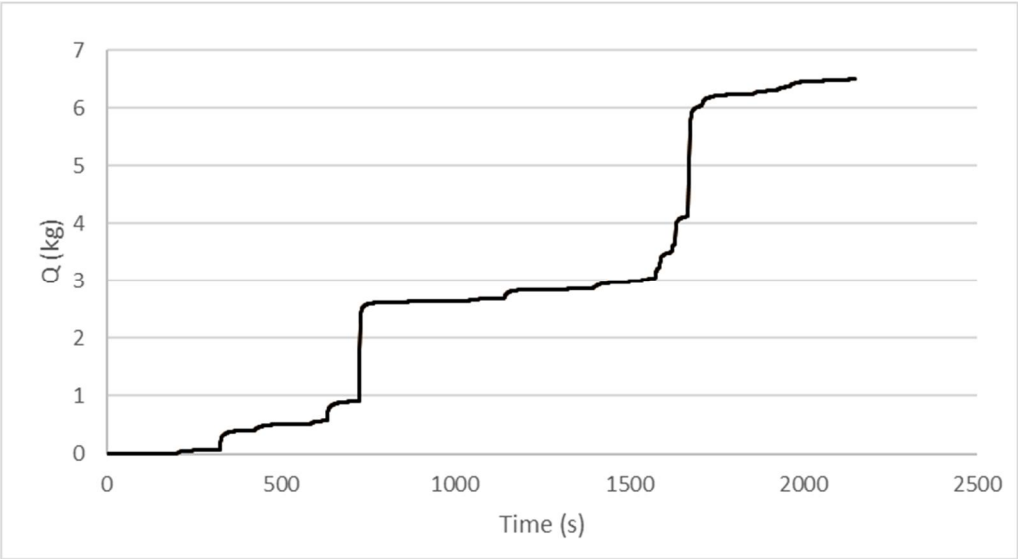

Figure 30 : Example of individual overtopping measurements with the weighing scale.

The probability of non-exceedance of each individual volume in the test (relative to the number of waves, 1000 waves), P_{ov} , can be calculated for each test.

The relation between the probability of the maximum individual volume and the average of the test volumes is observed by plotting $V_i/V_{average}$ against P_{ov} as in Figure 27.

6. Empirical formulae

Physical model tests are required when dealing with the stability of important structures such as breakwaters. Also empirical formulae can benefit from these tests as they can be checked and corrected against obtained test data:

- The mean discharge, for rubble mound slopes, can be estimated with Eurotop (2016) formulation: the influence factor (γ_f) to account for dissipation induced by the structure slope roughness and permeability is calculated for each test and the average value of all the tests is used in the formulation.
- The peak volumes (Vmax) and anticipated number of overtopping waves (Now) can be estimated with Eurotop (2016) methods, together with the distribution of individual overtopping wave volumes.

Understanding future changes in flood risk from waves overtopping seawalls or other structures is a key prerequisite for effective management of coastal defences. Occurrences of economic damage or loss of life due to the hazardous nature of wave overtopping are more likely nowadays than before, and coastal managers and users are now more aware of health and safety risks. Lowering the overtopping risk is therefore a key requirement for the design, management and adaptation of coastal structures, particularly as existing coastal infrastructures will be assessed for future sea conditions. There is also a need to warn or safeguard individuals of potentially dangerous overtopping waves on coastal defences or seaside promenades which should not be ignored.

The desire to reproduce the exact chronology of events may lead to much larger test durations and the need to include tidal level variation during the long experimental tests (i.e., the tidal wave during wave attack). This requires the development of new systems to control the filling and the emptying process of experimental facilities (variable and controlled flow rate, since the velocity of the tidal level rise and fall is not constant). It also requires the analysis of the effects in the operation of other equipment whose performance is influenced by the water level, namely the dynamic/active wave absorption systems which are based on real time measurements of the surface water elevation in two gages in front of the wave-maker paddle, and even in some passive wave absorption systems sensitive to the water level changes.

In addition, if the consideration of long-term effects is of interest, the impact of marine growth and of concrete strength variation on, e.g., rubble mound block stability, should be fully analyzed and the simulation of wind effects in the laboratory should also be improved (e.g., mean and gusts wind effects).

The measurement of structure damage must preferably be obtained without emptying and refilling the flume or basin, which can take a considerable period of time. Therefore, the measurements should be able to be performed through the water surface. Often mechanical profilers are still the preferred measurement device but new methods (terrestrial laser scanners, underwater laser scanners and stereo photogrammetry) can be used to scan the surface of coastal structures in order to obtain more precise measurements of damage (erosion). With these techniques, the surface can be obtained with millimetre resolution and sub-millimetre accuracy.

2.4 OVERTOPPING EVENTS IN BREAKWATERS: A FOCUS ON VERY LOW WAVE OVERTOPPING DISCHARGES FOR BREAKWATERS

2.4.1 Objective description

Wave overtopping is one of the critical responses for most linear coastal structures such as seawalls and breakwaters. For robustly designed and constructed harbour breakwaters, wave overtopping can be quite substantial without causing problems as the wave transmission will often be more important than the overtopping discharges per se, and will be analyzed alongside wave transmission through the harbour entrance.

But for coastal seawalls, or reclamation breakwater with infrastructure close behind, then the land-use immediately behind the defense structure may require overtopping to be limited to quite low values with a mean discharge as low as $q < 1$ or 10 $ls^{-1}m^{-1}$ (0.001 to 0.01 $m^3s^{-1}m^{-1}$).). Even with these mean overtopping discharges, individual overtopping volumes may be hazardous to people or unprotected equipment.

Overtopping discharges can be estimated using empirical methods, such as the EurOtop overtopping prediction manual (see EurOtop, 2016), however the most robust prediction method is to use physical model tests at an appropriate scale. The use of such tools are described by Allsop (1994), EurOtop (2016), Hughes (1993), Wolters et al. (2007, 2009).

2.4.2 Tests and experiments

The 2D model tests at HR Wallingford measured wave overtopping on a simple (smooth) 1:2 slope at a nominal scale of 1:20 with two different crest levels equivalent to 20m above bed level (structure A1) and 24m (structure A2). The tests were carried out in one of HR Wallingford's wave flumes, which is 50m long, 1m deep and 1m wide. No approach slope or bathymetry was used, so depths at the structure toe were the same as at the wave paddle. The relatively deep water was chosen to remove any shallow water effect on wave conditions with any consequential distortions to overtopping results, and to simplify the test section. Collection chutes from the test section to the measurement tanks varied between 0.8m to 6.7m (in prototype) width to accommodate a wide range of discharges with three tank sizes.

Most tests were run with water levels of 14m and 15m (in prototype), (19 and 35 tests respectively), and nine tests using a water level of 16m, all levels are referenced to the seabed. The target wave conditions were $H_s \approx 0.8$ to 3.7m, with extreme testing to $H_s \approx 4.8$m. The mean wave periods (Tm) ranged from 5s to 13s. The suggested conditions gave a wave steepness of s_{0m} ~0.06 (storm sea), 0.035 (ocean waves), and 0.01 (swell) for deep water. Tests were run for 500 or 1000 waves, although one test used multiple simulations with changed seed (starting point in an infinite long sequence) to give 10 x 1000 wave samples. This is particularly important for very low discharges. The sequence of the test conditions is not significant since there is no cumulative effect in overtopping. The order of tests was therefore defined according to convenience.

Mean overtopping discharges, q, measured during testing were compared with predictions given by the empirical formulae from the EurOtop 2 Manual (EurOtop, 2016). The number of overtopping waves, N_{ow}, and the individual overtopping volumes, V_{ow}, were also determined.

Test conditions were calibrated in the flume before construction of the test section, to minimize the corruption of incident waves by reflections. Calibration was an iterative process. The amplitude of the signal driving the wave generator was adjusted until the spectral significant wave height measured at the calibration point was within ±5% of the target significant wave height. The waves

were non-repeating wave sequences, with durations equal to 1000 T_m, of the target spectrum, required for a statistically significant sample for wave calibration analysis. The calibrated wave conditions are presented in Table 12.

2.4.3 Results and discussion

The overall test results for the 1:2 smooth slope obtained are shown in Figure 31 where dimensionless discharge ($q^*=q/(gH_{m0}^3)^{0.5}$ is plotted against dimensionless freeboard (R_c/H_{m0}). The data are grouped by steepness for analysis. The data are plotted together with the EurOtop 2 predictions, (equation 5.18) and upper and lower 5% confidence bands. Data obtained below $q^* = 10^{-8}$ are considered to be equivalent to 'no overtopping', since the measuring instruments are unable to detect variations smaller than this limit. It is noticed that all of the very low overtopping data points are associated to low steepness wave conditions, $s_{0m} < 0.03$.

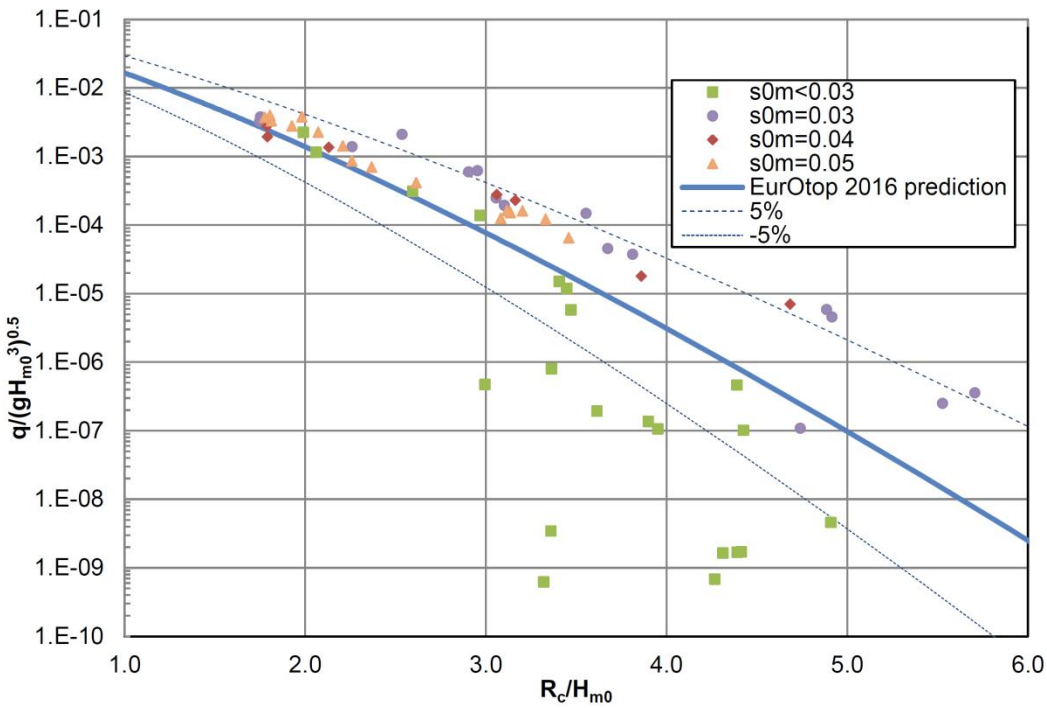

Figure 31 : Dimensionless overtopping discharges against dimensionless freeboard, Figure 3 from Silva et al. (2017)

After running the main test conditions, various repetitions were performed for those wave conditions resulting in very low overtopping discharges. Some repetitions were carried out with a different duration (1000 or 10 000 waves) and others with a different seed. The overtopping results (see Figure 32) from these repetitions illustrate inherent uncertainties associated with very low overtopping discharges. Taking as example WC13, the original wave condition and its exact repetition result in no overtopping, but when starting at a different position in the 'parent' sequence (using a different seed) the measured overtopping was at least three orders of magnitude larger. The same type of observation was done with WC23 and WC14, although the difference is about one order of magnitude. A long duration test was performed for WC23 (10,000 waves). Firstly one sample of long duration was analyzed and then 10 shorter samples of 1000 waves. One sub-sample in WC23 yield a discharge which is 10 – 100 times greater than the other sub- samples.

Table 12 : Calibrated wave conditions.

Incident condition	SWL (m)	H_{m0} (m)	S_m (-)	T_m (s)	T_p (s)
WC01	16	1.6	0.036	5.32	5.90
WC02	16	2.2	0.036	6.26	6.89
WC03	16	0.8	0.010	7.16	7.87
WC04	16	1.2	0.010	8.77	10.3
WC05	15	2.8	0.062	5.37	5.90
WC05J02	15	2.8	0.062	5.37	5.90
WC05J12	15	2.8	0.062	5.37	5.90
WC05J01	15	2.8	0.062	5.37	5.90
WC05J06	15	2.8	0.062	5.37	5.90
WC06	15	1.6	0.036	5.32	5.90
WC07	15	3.7	0.060	6.31	6.89
WC08	15	2.2	0.036	6.26	6.89
WC09	15	4.8	0.060	7.16	7.87
WC10	15	2.8	0.035	7.16	7.87
WC10J12	15	2.8	0.035	7.16	7.87
WC10J01	15	2.8	0.035	7.16	7.87
WC10J06	15	2.8	0.035	7.16	7.87
WC11	15	0.8	0.010	7.16	7.87
WC12	15	3.0	0.035	7.42	10.3
WC13	15	1.4	0.010	9.48	10.3
WC14	15	2.8	0.010	13.37	14.8
WC15	14	2.8	0.062	5.37	5.90
WC16	14	1.6	0.036	5.32	5.90
WC17	14	3.7	0.060	6.31	6.89
WC18	14	2.2	0.036	6.26	6.89
WC19	14	0.8	0.010	7.16	7.87
WC20	14	2.8	0.060	5.46	7.87
WC21	14	4.8	0.036	9.26	7.87
WC22	14	4.0	0.036	8.45	10.3
WC23	14	1.4	0.010	9.48	10.3
WC24	14	2.8	0.010	13.37	14.8
WC25	14	2.2	0.015	9.62	10.3

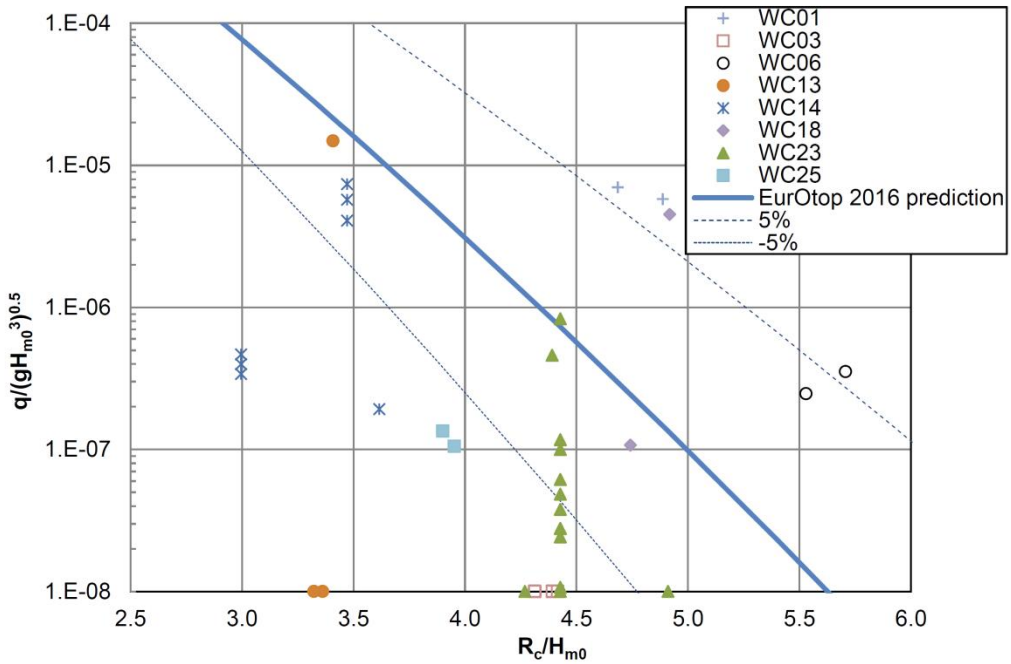

*

Figure 32 : Wave overtopping data – expanded (repeated wave conditions). Figure 5 from Silva et al. (2017)

2.4.4 Recommended protocol

In designing and operating such physical models to quantify low overtopping discharges, a number of key steps may be helpful:

a) The test conditions should take account of the appropriate range of water levels, wave heights and wave periods. The most relevant combinations will likely be developed from a Joint Probability Analysis (JPA) which will derive combinations (usually of water level and wave height) that all have the same total return period. An example is shown in Figure 33.

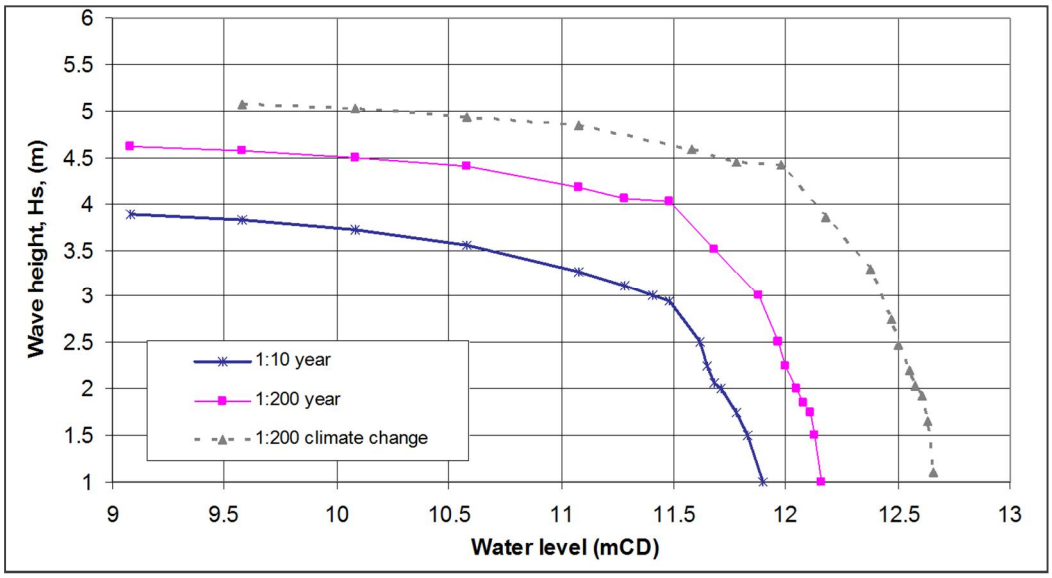

Figure 33 : Example JPA for a higher-tidal-range site (UK), Figure 6 from Allsop & Hawkes (2016)

b) The expected mean overtopping discharges (q) should be estimated for each combination of test conditions from the JPA using appropriate empirical formulae, e.g. as in the EurOtop manual. These calculations may require the structure to be simplified to fit the configuration for which the formulae are valid. (Alternatively, the user might prefer using a Neural Network or similar tool that could be valid for a larger number of structure configurations.) These values of q give two critical pieces of information: (i) they can be used to identify which combinations of test condition are most likely to give the greatest overtopping; and (ii) they estimate the ranges of discharge that may need to be measured.

c) Calculate peak volumes (V_{max}) and the anticipated number of overtopping waves ($N_{ow\%}$) using methods in the EurOtop manual.

d) Measurement tanks and instruments should be devised to accept the total volume of water expected over 1000 waves at an appropriate resolution. This may require a range of measurement tanks, and of overtopping collecting chute widths. The tanks should be equipped with methods to record wave-by-wave volumes (V_i), see example in Figure 34. It can be helpful to install an event detector at the crest of the structure to identify each individual overtopping wave and determine N_{ow}. The information from the detector can be cross-checked against the data collected in the tank to determine individual volumes.

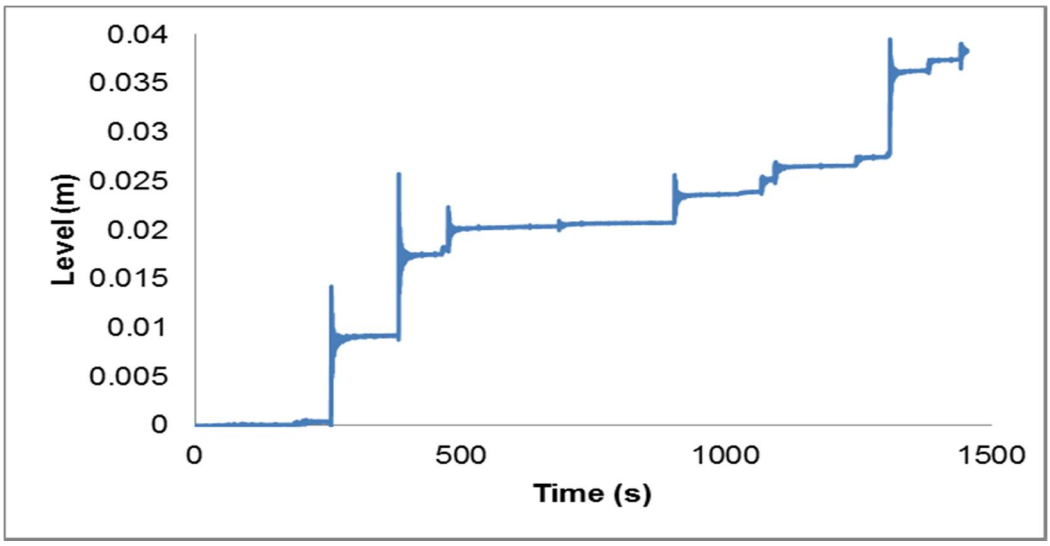

Figure 34 : Example overtopping measurements, wave-by-wave, Figure 6 from Silva et al. (2017)

e) Design the test length using estimates of the anticipated number of overtopping waves ($N_{ow\%}$). The default test duration should be 1000 waves ($1000T_m$), but for $N_{ow\%}$ > 10% then shorter tests ($500T_m$) may be sufficient. For very low overtopping, $N_{ow\%}$ < 0.5%, longer tests may be run, say 10,000 waves. These long tests must NOT use wave sequences that repeat during that duration.

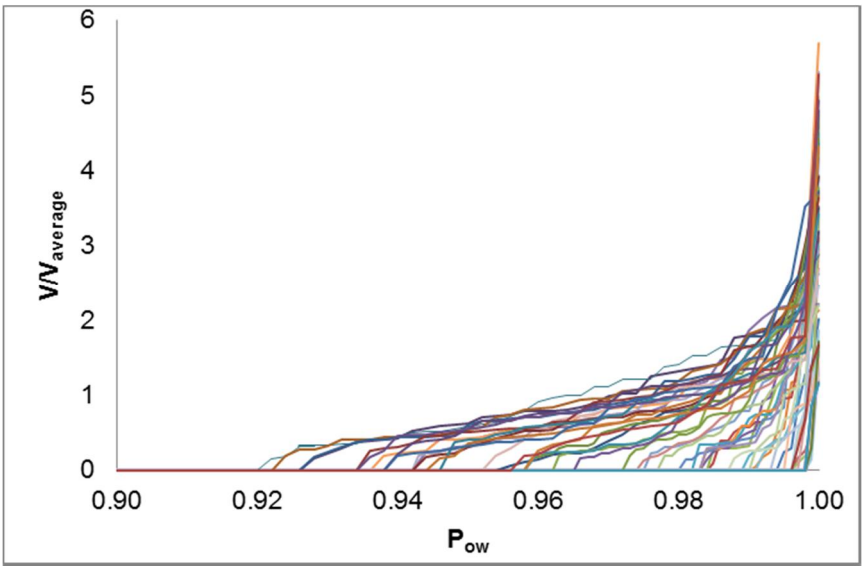

Figure 35 : Dimensionless overtopping volumes against non-exceedance probability, Figure 7 from Silva et al. (2017).

f) Run model tests for test duration as in e). Measure q and V_i. Plot dimensionless mean overtopping against dimensionless freeboard as in Figure 31. Compare measurements against simple prediction made in b) above. If the divergence between simple prediction and the measurement requires, then use the comparison to adjust future test conditions.

2.5 OVERTOPPING EVENTS IN BREAKWATERS : IMPROVING THE ESTIMATION OF OVERTOPPING DISCHARGES IN BREAKWATERS USING VIDEO IMAGERY

2.5.1. Objective description

Coastal structures, like breakwaters and revetments, are designed to allow for a certain maximum overtopping rate for design conditions. Due to sea level rise, the difference between the level of the crest and the sea water will decrease, while wave conditions increase due to the rise in water depth. These changes potentially threaten the stability of coastal structures worldwide.

For risk and safety assessment or design studies, the roughness of the front slope is a key parameter in determining the overtopping rates for coastal structures. Capel (2015) showed that due to an increase in flow depth, i.e. the thickness of the run-up tongue, the effective roughness of the front slope reduces. The roughness of the front slope is not a constant factor, but reduces for larger overtopping rates due to an increase of flow depth. The present roughness values, as given for instance in the EurOtop manual, are therefore only valid (and sometimes conservative) for mild overtopping rates of 0.1 to 1 $Ls^{-1}m^{-1}$.

A correct assessment of the overtopping rates is a key parameter when it comes to risk and safety assessment. In many areas, governmental organizations are willing to allow increased overtopping rates when the risk to casualties or damage to properties is limited. This could mean that crest levels are not adjusted in response to sea level rise. However, in the decision-making process, correct values of overtopping should be available. Using typical roughness values, which are only valid up to overtopping rates of 1 $Ls^{-1}m^{-1}$, are likely to underestimate these overtopping rates and may lead to poor decisions with possible negative consequences in the future.

In this study, the possibilities of deriving flow depths and bore speeds along a coastal structure from high speed video imagery are explored. Automated semantic segmentation techniques are used to detect the instantaneous flow dept, bore speed of the wave run-up of individual waves, which potentially provides all parameters to validate the individual overtopping quantities per wave and the roughness parameter as a function of flow depth on complex structures. Semantic segmentation is a form of image classification that is widely used in computer vision science. It aims to subdivide images or videos in meaningful (semantic) regions.

2.5.2. Tests and experiments

A series of 27 tests in the Scheldt Flume at Deltares is used in this study. The tests were characterized by a breakwater with smooth slope that was exposed to approximately 1000 waves. Between the different tests the water levels (3), wave height (3) and wave steepness (3) varied. In addition, the same series of 27 tests (and 6 repetitions) with the same wave forcing and similar breakwater shape, but with a rubble mount slope and crest wall, was used to widen the applicability of the automated semantic segmentation techniques to more turbulent waves. These tests were used for model training, but model testing focused on the smooth front slope tests as a tighter model/data comparison was possible.

2.5.2.1. Data acquisition

High-speed video footage captured at 150 Hz through the glass flume wall was obtained from a single camera placed on a tripod approximately 1 m from the flume (Figure36). A flow depth measurement at the breakwater crest is used to order the waves on impact. From the top 100 waves with largest flow depth in each test 50 waves are used in the analysis.

Figure 36 : Snapshot from high-speed video footage. Red dots are reference points for calibrating the images.

2.5.2.2. Data pre-processing

The high-speed video footage of a single test is split into individual wave recordings. For each wave, the video footage from 1 s prior to 1 s after the recorded impact peak is taken, resulting in 50 sequences of 2 s (or 300 frames) videos of individual waves per test.

The per-wave videos are subsequently converted to 300 timestacks with the vertical dimension and time preserved, but the horizontal dimension discarded (Figure 37, left). By using timestacks rather than the full video footage, segmentation algorithms can be much simpler (2D vs. 3D), but relations between adjacent pixels in horizontal direction are effectively discarded in favour of relations in time.

A random subset of 225 timestacks is manually annotated. Manual annotation implies that the position of the water level is manually indicated. In this study, the manual annotation involves tracing the water level with a green marker (Figure 37, middle). A simple algorithm[1] then converts the manual annotation to a binary mask indicating what part of the timestack corresponds to the passing wave and what part of the timestack does not (Figure 37, right). The binary masks provide the *ground truth* based on which the semantic segmentation algorithm can be trained and/or tested.

[1] The algorithm converts the green tracer into a binary mask using a threshold for the greeniness. The greeniness is the ratio between the intensity of the green channel with respect the total intensity of a pixel. The area between the first and last pixel above threshold in each row/column of pixels is included in the mask.

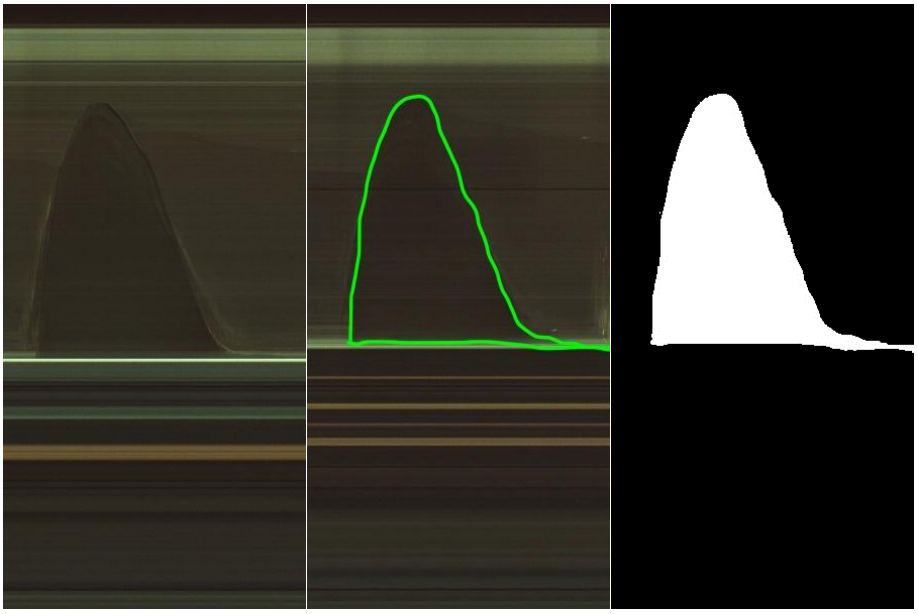

Figure 37 : Examples of a 300x600 timestack. Vertical axis is in space, horizontal axis is in time. Left panel: original timestack. Middle panel: manual annotation. Right panel: resulting binary mask.

2.5.2.3. Model training

The annotated timestacks are used for training a segmentation model. In this study, two types of segmentation models are considered: a Logistic Regressor (LR) following the workflow described in Hoonhout et al. (2014, 2015a, 2015b), and a deep image segmentation model (i.e. neural network) based on the Segnet network layout and pretrained with VGG weights. The deep learning segmentation model appeared to provide better results on tests with smooth slopes and is used in the remainder of this document. The LR might still be considered for permeable/ rough structures. The keras toolbox is used to construct and train the deep image segmentation model.

The deep image segmentation model consists of various hidden convolution and pooling layers that derive abstract features from pixels, neighbouring pixels, neighbouring clusters of pixels and ultimately the image as a whole (Figure 38). The dimensionality of the layers increases with depth of the network, ultimately describing the entire image in a limited set of high dimensional functions.

The high dimensional functions are subsequently used to describe the binary segmentation classes “wave” and “no wave” by adding one or more densely connected layers to the neural network of which the dimensionality decreases with depth (Figure 38).

Training of the model is done by supplying the input (pixel intensities) and output (classes) of the neural network and applying forward/backward inference and learning. The process aims at finding the weights associated with the network nodes that best describe the transformation from input to output.

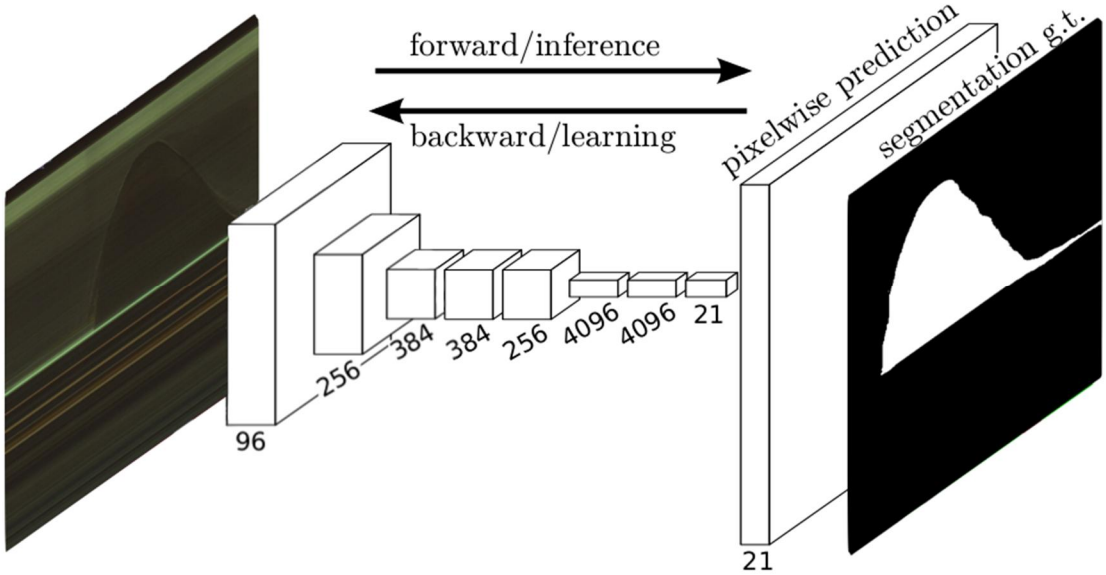

Figure 38 : Schematic of deep image segmentation. From the original image (left) a set of neural network layers describe the image in a decreasing number of functions with increasing dimensionality. The pixelwise prediction of the segmentation classes is obtained using one or more densely connected layers (right).

Deep learning is highly computationally intensive. Therefore, deep image segmentation models cannot reasonably be computed on ordinary computers. GPU enabled machines at Amazon EC2 were rented to perform the computations, resulting in a speedup up to a factor 20 compared to ordinary CPU-enabled machines. The costs of training a single model with its current limited complexity are in the order of 1 hour or $1.

2.5.2.4. Model testing

25 from the 225 annotated timestacks are not used for training, but for testing only. Therefore, a non-exhaustive comparison between model predictions and manual annotations can be made.

In addition, a model/data comparison is made by deriving physical parameters, like bore speed, flow depth, overtopping duration and overtopping volume, for all waves in the dataset. Comparing these physical parameters with the measured quantities in the flume, also provides insight in the performance of the algorithm.

In each timestack, the passing wave is detected by the algorithm and thus the time-variation in local flow depth is determined. For each wave, the maximum local flow depth at the breakwater crest is then compared to the measured maximum local flow depth in the flume.

Stacking all detected flow depth time series for each point along the flume axis, provides us with a continuous spatiotemporal description of the flow depth. From these spatiotemporal flow depth descriptions, time-averaged bore speeds, time-averaged flow depths and overtopping durations are determined.

The time-averaged bore speed per wave ($\bar{v}$ [m/s]) is estimated from rising part of the 2-cm flow depth contour in the spatiotemporal description of the flow depth. It is assumed that the 2-cm flow depth contour is a good proxy for the instantaneous position of the bore front. The slope of the linear fit of this contour is then an estimate of the speed of the bore

front. Only linear fits with an RMSE of less than 3 cm in the horizontal bore front position are taken into account.

The overtopping duration per wave (T [s]) is similarly estimated as the period between the up and down crossing of the 2-cm flow depth contour at the onset of the breakwater crest (origin of the reference frame). This period represents the time that a significant runup tongue (> 2 cm) is present at the breakwater crest.

The time-averaged flow depth per wave ($\bar{h}$ [m]) is estimated by averaging the instantaneous flow depth at the onset of the breakwater crest over the overtopping duration T.

The product of these three parameters, which are visually described in Figur, is assumed to provide us with an estimate of the overtopping volume per wave (q [m^3/m]):

$$q \approx \overline{v \cdot h} \cdot T$$

The cumulative overtopping volume for all waves in a test is then compared to the total overtopping volume as measured in the flume.

2.5.3. Results and discussion

The results are ordered based on several test properties that can be derived from the test identification code. The test identification code has the following form:

AXWXTXYY

and constitutes of the following code parts:

Code part	Description	Values	Interpretation
AX	breakwater design	AX, BX	
WX	slope roughness	X = 0	smooth slope
		X > 0	rubble mount
TX	water level	X = 1	h = 0.80 m
		X = 2	h = 0.75 m
		X = 3	h = 0.70 m
YY	wave steepness and significant wave height	YY = 01	s_{0p} = 0.015 and H_{m0} = 0.08 - 0.12m
		YY = 02	s_{0p} = 0.015 and H_{m0} = 0.08 - 0.12m
		YY = 03	s_{0p} = 0.015 and H_{m0} = 0.08 - 0.12m
		YY = 04	s_{0p} = 0.025 and H_{m0} = 0.10 - 0.14m
		YY = 05	s_{0p} = 0.025 and H_{m0} = 0.10 - 0.14m
		YY = 06	s_{0p} = 0.025 and H_{m0} = 0.10 - 0.14m
		YY = 07	s_{0p} = 0.040 and H_{m0} = 0.12 - 0.16m
		YY = 08	s_{0p} = 0.040 and H_{m0} = 0.12 - 0.16m
		YY = 09	s_{0p} = 0.040 and H_{m0} = 0.12 - 0.16m

The main idea behind the test conditions is based on achieving similar overtopping quantities for XYY=01, XYY=04, XYY=07 and for XYY=02, XYY=05, XYY=08 and for XYY=03, XYY=06, XYY=09. This means that the wave height increased for imposed lower water levels as well as imposed larger wave steepness.

Note that increasing water level classes indicate a decrease in the imposed water level. Also note that the nine values for YY, indicating the wave steepness and height, in fact constitute

a matrix that defines three wave steepness classes as well as three wave height classes that are used in the remainder of this chapter:

	wave height class	1	2	3
	wave height [m]	*0.08 - 0.12*	*0.10 - 0.14*	*0.12 - 0.16*
wave steepness class	*wave steepness [-]*			
1	*0.015*	YY = 01	YY = 02	YY = 03
2	*0.025*	YY = 04	YY = 05	YY = 06
3	*0.040*	YY = 07	YY = 08	YY = 09

2.5.3.1. Results

200 out of 225 annotated images, including both rubble mount and smooth cases, were used to train the deep image segmentation model. 25 images can therefore be used to test the capabilities of the algorithm to reproduce the manual annotations. This test shows that the deep image segmentation model predicts 98.2% of the pixels correctly with respect to manual annotations. The accuracy of the model is slightly higher for the tests with a smooth slope.

About 120.000 timestacks from 1356 waves in 27 experiments with a smooth slope were analysed. The waves that were not analysed were not recorded due to technical limitations in the acquisition procedure or were not in the top-100 waves with largest impact. All of the analysed timestacks provided sensible results in the sense that a wave-like shape was detected.

A spatiotemporal description for each wave can be obtained by stacking the water level positions detected in each timestack corresponding to a single wave. Figure 39 visualizes the largest waves from the 9 tests with a smooth slope and maximum still water level, but varying wave steepness and significant wave height.

Figure 40 visualizes the underlying raw data, being the waves detected in the timestacks. In the upper panel, the waves are coloured based on their wave steepness class. The rainbow-effect suggests that steeper waves generally result in lower flow depths at the breakwater crest. The middle panel in Figure 40 depicts the same data coloured by wave height class. In this figure, the rainbow-effect is reverted, which suggests that higher waves generally result in higher flow depths at the breakwater crest. The lower panel in Figure 40 again depicts the same data coloured by water level. The absence of a rainbow-effect suggests that the water level is less important to the flow depth at the breakwater crest.

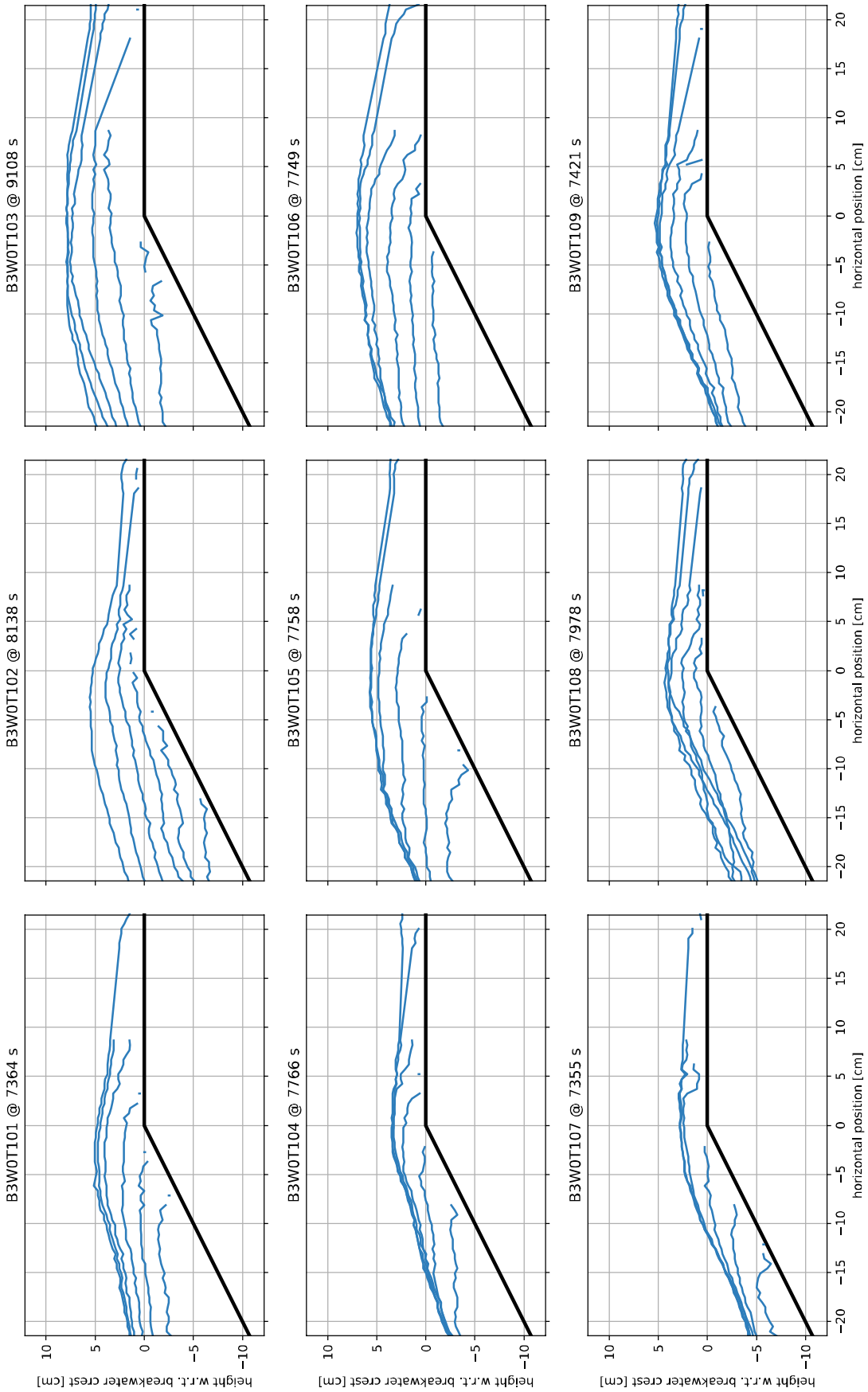

Figure 39 : Examples of waves detected by the deep image segmentation algorithm. Each subplot depicts 6 frames from the total of 60 frames obtained in the 0.4 s before the maximum flow depth was recorded at the physical measurement location.

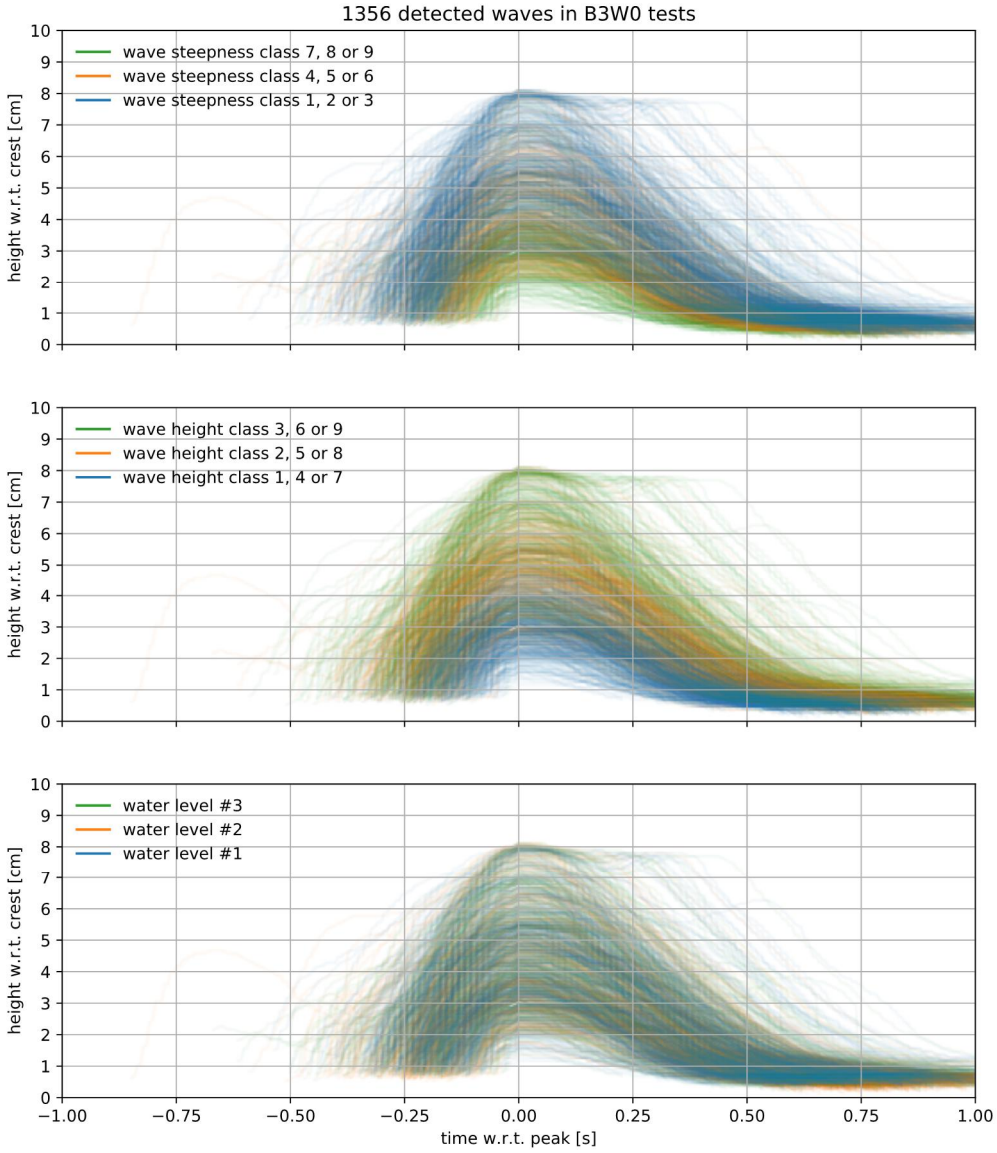

Figure 40 : Waves detected at the breakwater crest. Upper panel: coloured by wave steepness class, with wave steepness increasing in order blue, orange, green. Middle panel: coloured by wave height class, with wave height increasing in order blue, orange, green. Lower panel: coloured by water level class, with water levels decreasing in order blue, orange, green.

Figure 41 visualizes a per-wave comparison between video-based measurements and physical measurements. The figure depicts the maximum flow depth per wave per test as obtained from video-based measurements compared to the physical measurements. The figure shows that video-based measurements in general compare well to physical measurements, but overestimates the flow depth occasionally. In 15 cases the deviation between video-based and physical results exceeds 2 cm. In all cases a splashing wave is visible in de raw video data, which is included in the flow depth in the video-based results, but not in the physical measurements. Smaller overestimations might be caused by air intrusion. Air bubbles cause underestimation of the actual flow depth in the physical measurements, but not in the video-based measurements. Also note that the video-based and physical measurements are not exactly co-located as the physical measurement device is not visible in the video data. The video measurements are obtained seaward compared to

the physical measurements, which can explain the structural overestimation of the video measurements as well as the scatter around the diagonal.

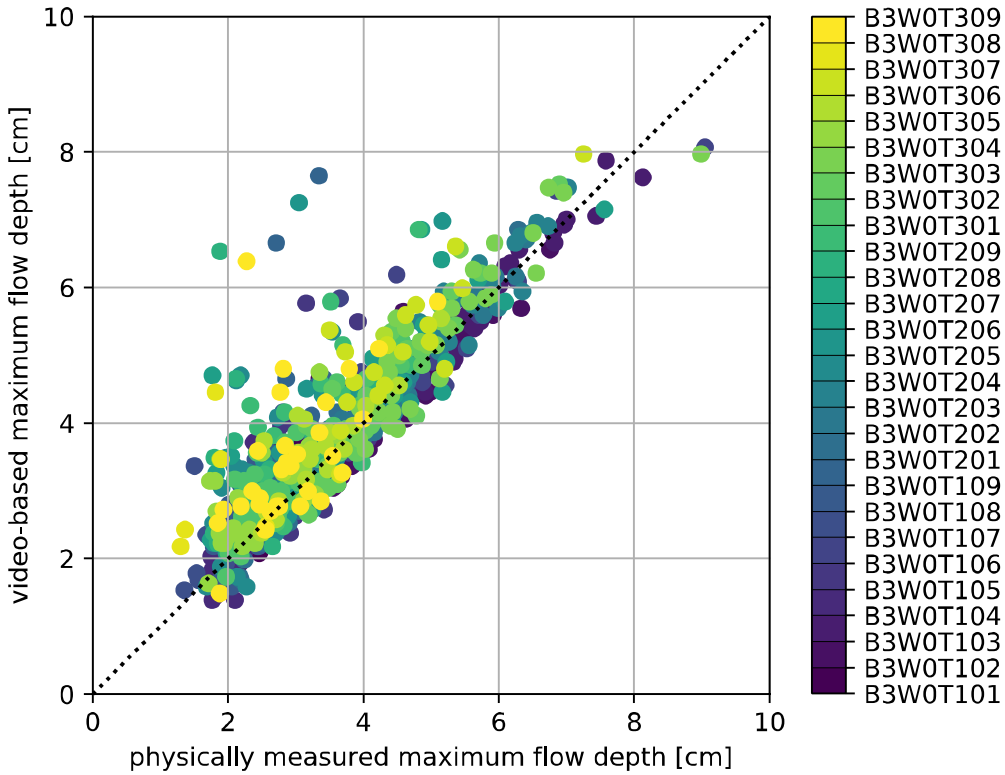

Figure 41 : Water levels detected from video vs. physically measured flow depths at breakwater crest for the tests with smooth slope.

Figure 42 visualizes the test-averaged maximum flow depths grouped by wave height, water level and wave steepness class. The figure indicates again that the highest wave height (class 3) shows the highest flow depth at the breakwater crest. Slight variations between tests with equal wave height class, but increasing wave steepness seem to be visible, indicating that increasing wave steepness results in a lower flow depth at the breakwater crest. No dependency on the water level can be observed.

The dependencies of the video-based flow depth (upper panels in Figure 42) at the breakwater crest to wave height, wave steepness and water level compare well to the physically measured dependencies (lower panels in Figure 42). The mean absolute error (MAE) between the video-based and physically measured flow depths accumulates to 4 mm. The MAE increases with decreasing wave steepness (3 mm to 7 mm) and is reasonably consistent over the wave height and water level classes. The root-mean-square error (RMSE) accumulates to 7 mm.

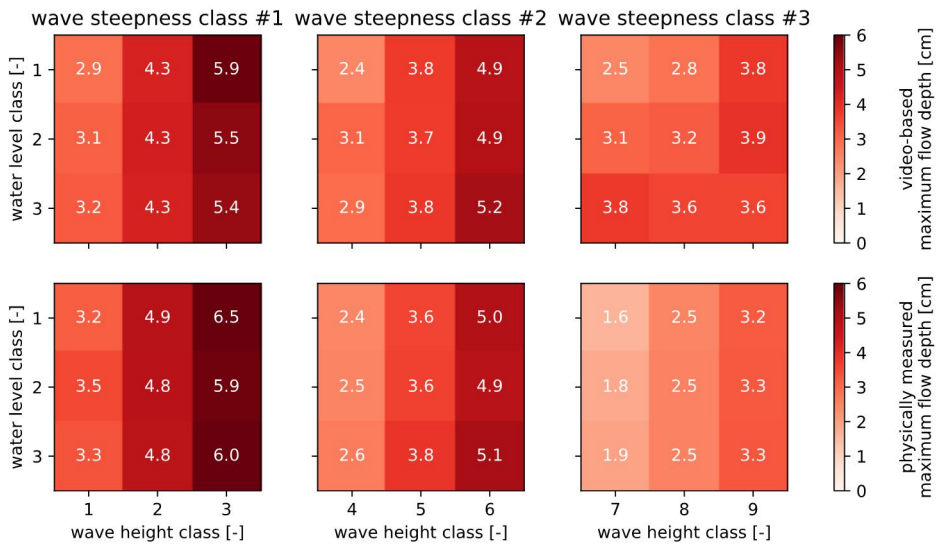

Figure 42 : Test-averaged video-based (upper panels) and physically measured (lower panels) maximum flow depths at breakwater crest grouped by imposed boundary condition classes. Only the top-50 waves with highest impact are included in the averages.

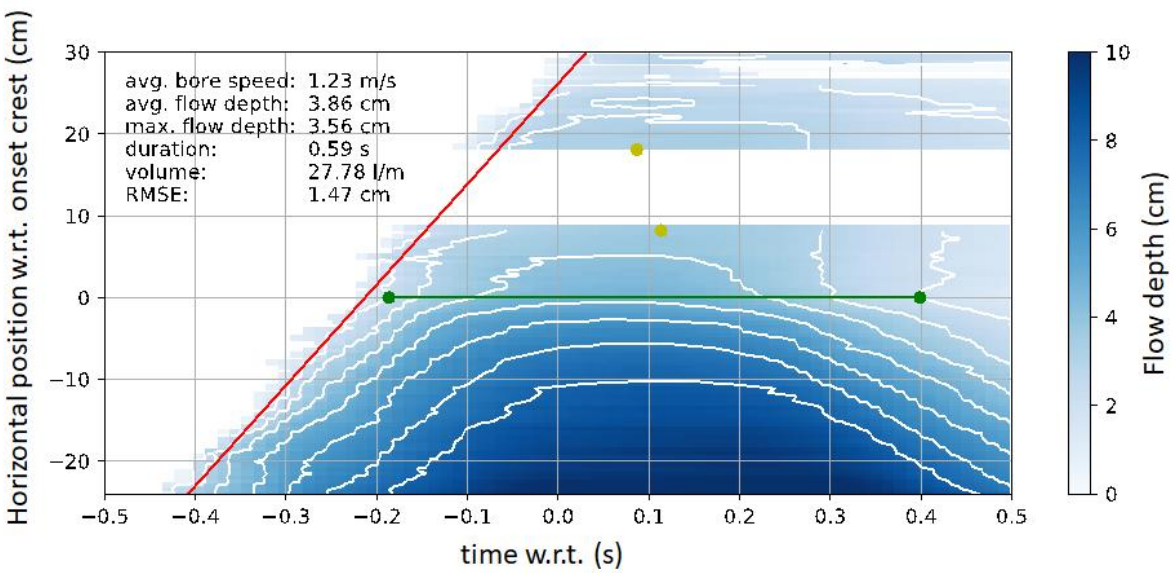

Figure 43 : Spatiotemporal variations in flow depth (blue shading and white contours) of a single wave (B3W0T101, wave No. 9) and derived quantities bore speed (red line slope: linear fit through 2 cm flow depth contour), overtopping duration (green line length: maximum distance between up- and down-crossing of 2 cm flow depth contour through the origin of the vertical axis) and maximum flow depth in the vicinity of the physical measurement location (yellow dots). Horizontal cross-sections of the blue flow depth shading just below the green line are depicted in Figur 40.

The flow depth time series depicted in Figure 40 are all detected just in front of the breakwater crest. However, the algorithm provides flow depths time series on every position along the flume axis. If all flow depth time series of an individual wave are stacked, a spatiotemporal description of the flow depth in an individual wave is obtained (Figure 43). From this spatiotemporal description, physical parameters per wave, like the time-averaged

bore speed, overtopping duration, time-averaged flow depth and ultimately the total overtopping volume are derived.

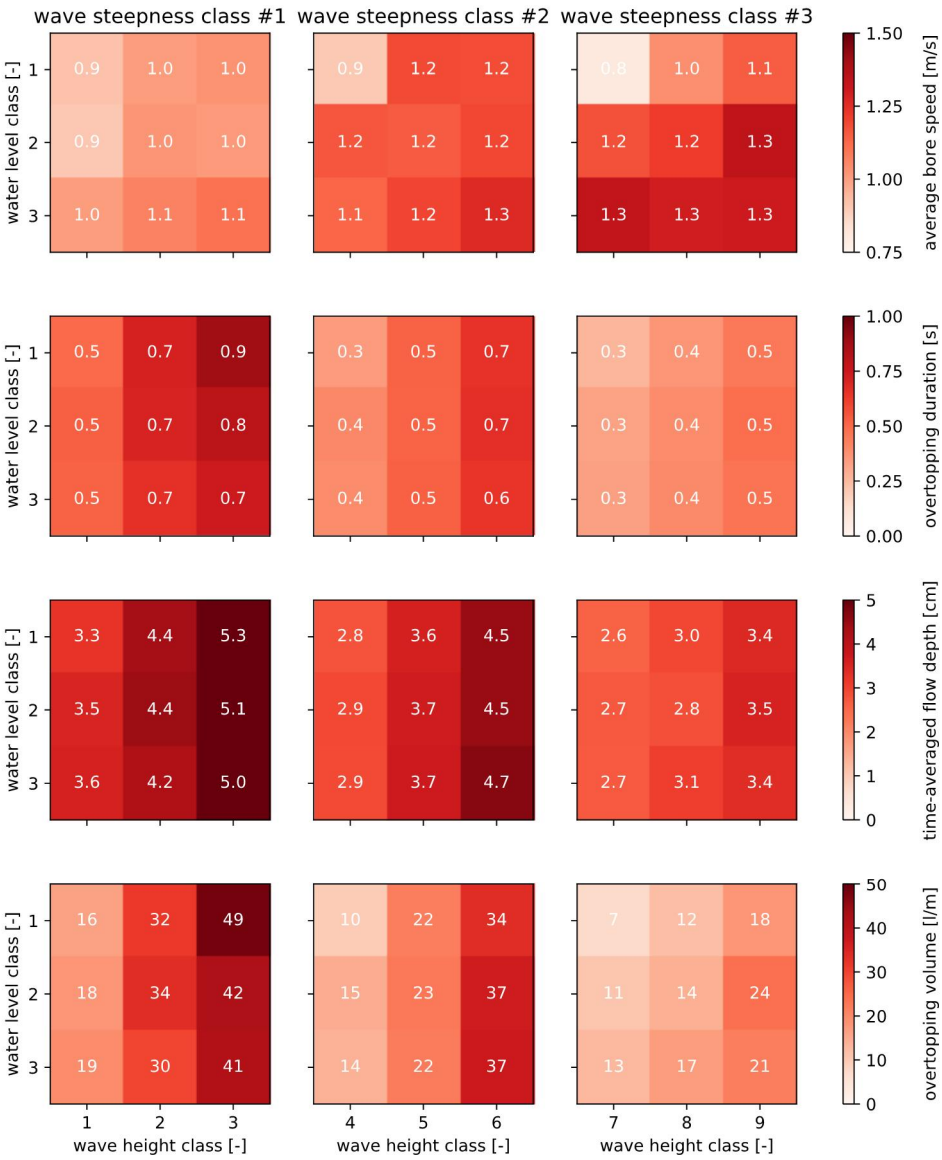

Figure 44 : Test-averaged per-wave physical parameters derived from video and grouped by imposed boundary condition classes. First row: per-wave averaged bore speed derived from a linear fit through the 2-cm flow depth contour (slope of red line In Figure 43). Second row: overtopping duration derived from the maximum distance between up- and down-crossing of the 2-cm flow depth contour through the origin of the horizontal flume position (i.e. onset breakwater crest; length of green line in Figure 43). Third row: average flow depth at the breakwater crest during overtopping derived from averaging the instantaneous flow depth (blue shading in Figure 43) during overtopping (green line in Figure 43). Fourth row: overtopping volume per wave derived from the product of the per-wave average bore speed, overtopping duration and average flow depth at the breakwater crest.

Figure 44 depicts the test-averaged time-averaged bore speed, overtopping duration, time-averaged flow depth and overtopping grouped by wave height, water level and wave steepness class. The overtopping volume seems predominately dependent on wave height

and steepness and dominated by the overtopping duration and time-averaged flow depth. The time-averaged bore speed also seems to be dependent on water depth, suggesting that bore speed is less important to the total overtopping volume of an individual wave.

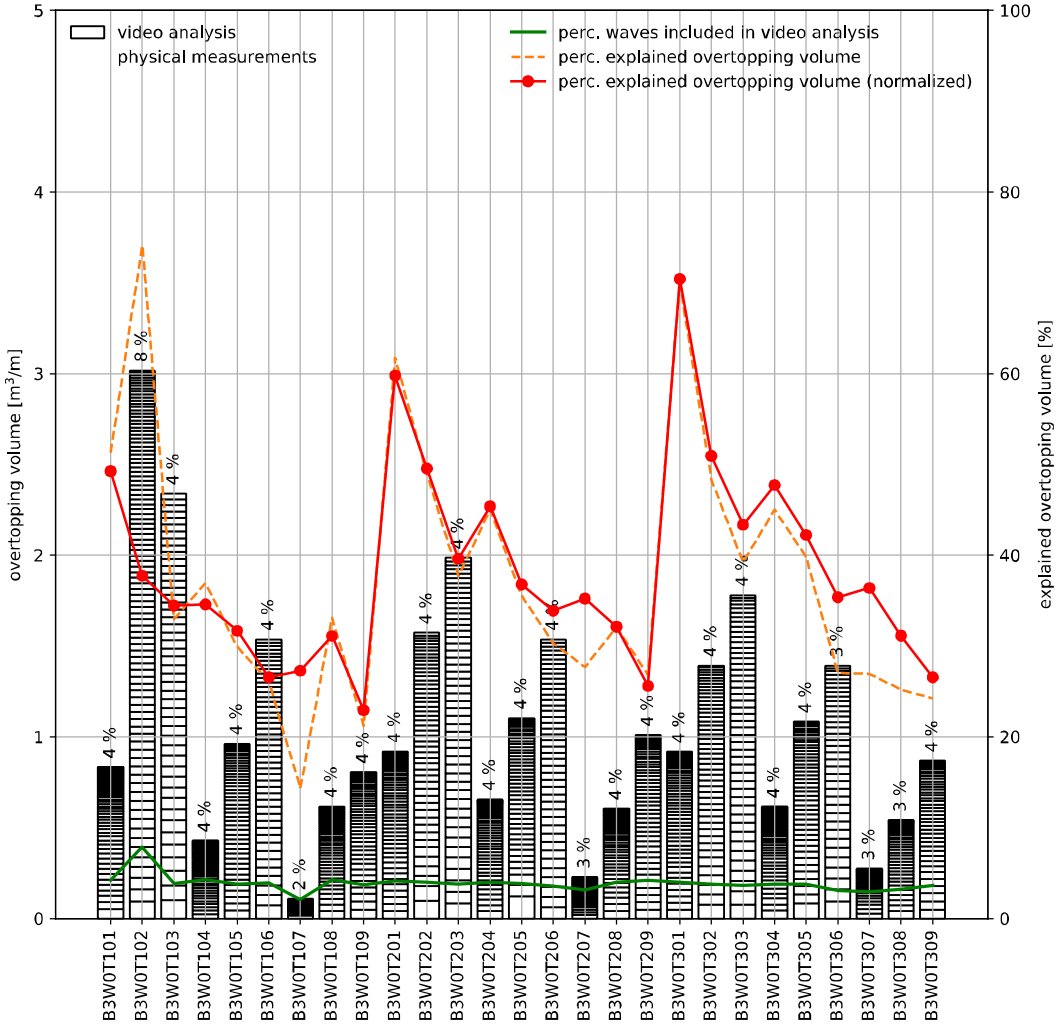

Figure45 : Cumulative overtopping volumes per test as derived from video and physically measured. The green line and percentages on top of each bar indicate the fraction of waves in a test that are included in the video analysis, which is used to normalize the fraction of explained overtopping volumes (orange dashed line) to 4% (~50 waves) for all tests (red line).

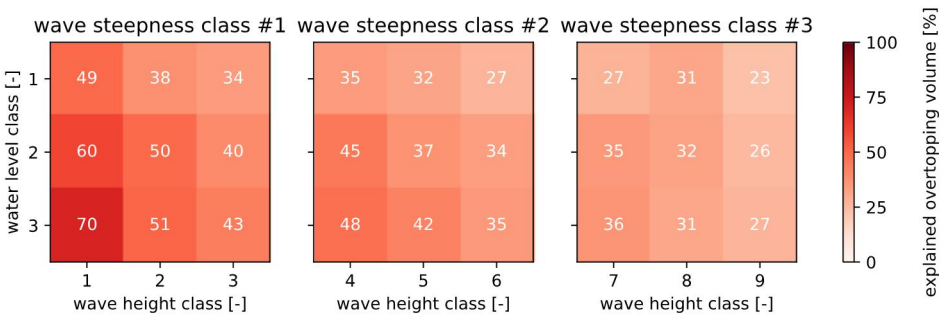

Figure 46 : Test-averaged percentage of overtopping volume explained by top-50 waves with largest impact in video analysis compared to physical measurements. This figure depicts the same data as the red line in Figure 45.

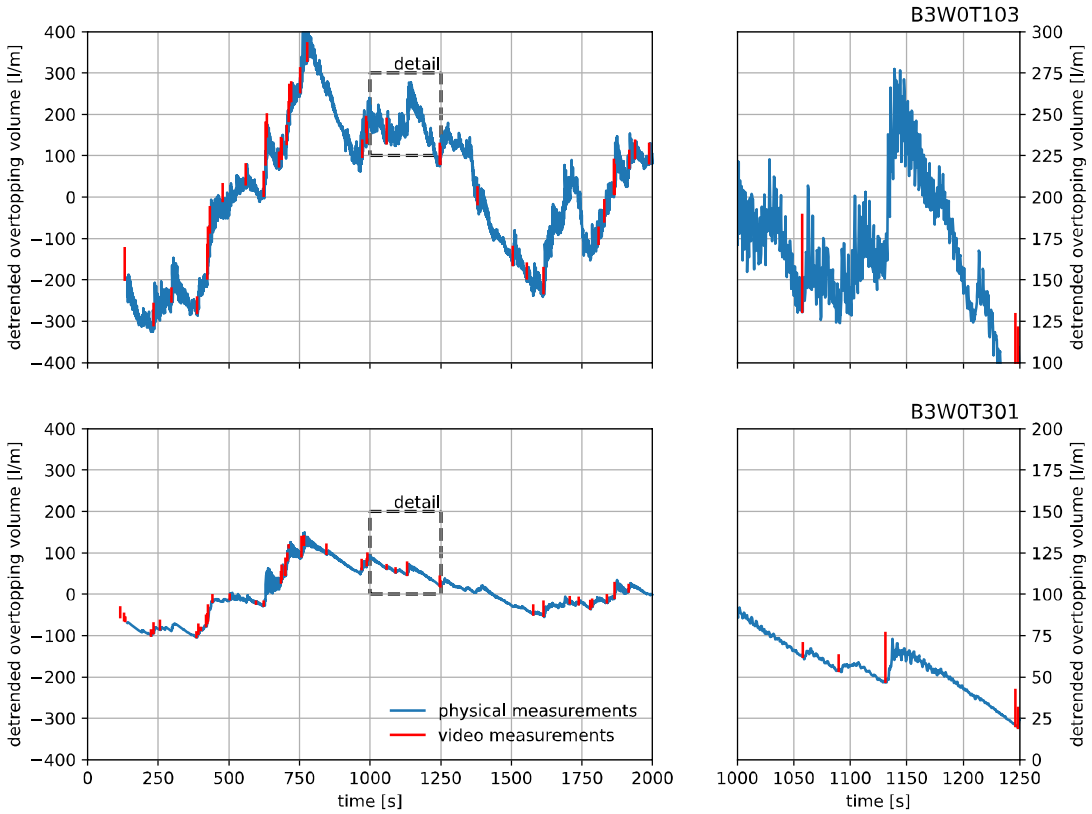

Figure 47 : Comparison between physically and video-based measured overtopping volumes in time for two tests. Upper panels: result for test B3W0T103 with a low explained overtopping volume of 34% shows significant overtopping events that are not included in the video analysis. Lower panels: result for test B3W0T301 with a high explained overtopping volume of 70% shows hardly any missed overtopping events and reasonable similarities between the video based overtopping volume (length vertical red lines) and the physically measured overtopping volumes (steps in blue line). Note that the physically measured overtopping time series is detrended for better comparison. Therefore, inclining sections correspond to relatively large overtopping events, horizontal sections correspond to average overtopping events and declining sections roughly correspond to no overtopping events.

All overtopping volumes associated with individual waves within each test are summed and compared to the total measured overtopping volume in a test (Figure 45). The 50 analysed waves per test explain 25% to 70% of the total measured overtopping volume, depending on the imposed boundary conditions. Note that the 50 analysed waves are taken from the top-100 waves with largest flow depth. Assuming that large flow depths relate to large overtopping volumes, this dataset is therefore expected to explain 50% of the measured overtopping volume at most.

The percentage of explained overtopping volume increases with decreasing wave steepness, wave height and water level (Figure 46). This suggests that the frequency of overtopping (i.e. the number of waves contributing to the total overtopping volume) increases with wave steepness, wave height and water depth and the 50 analysed waves are insufficient for an accurate overtopping volume estimate in the majority of the tests.

A discrepancy between physically and video-based measurements can also be expected if the assumption that overtopping volumes can be estimated through the product of the time-averaged bore speed, overtopping duration and time-averaged flow depth, appears to be false. However, the estimated overtopping volumes would likely be more random and no

correlation between the explained overtopping volume and the imposed boundary conditions would be expected. Moreover, visual comparison between physically measured overtopping volume time series and the video-based overtopping volumes suggests that the explained overtopping volume is low in tests where significant overtopping events are missed in the analysis and high otherwise (Figure 47).

2.5.3.2. Discussion

The first application of an automated semantic segmentation algorithm in the Deltares facilities is briefly discussed based on performance and applicability. Performance refers to the workings of the algorithm compared to the expectation or requirements. Applicability refers to the usefulness of the algorithm in practice.

2.5.1.1.1 Performance

Based on a limited number of 225 ground truth samples an algorithm is trained that can detect wave-like shapes from timestacks. Both the pixel accuracy that was tested against a dedicated test set as well as the comparison between video-based and physical measurements provide confidence in the performance of the algorithm.

The deep image segmentation algorithm performed excellent on the video data from the reference tests with a smooth slope. Given the pixel accuracy of 98.2%, it can be questioned whether differences between the video-based and physical measurements are actually errors in the video detection algorithm, or inaccuracies in the physical measurements. However, the most prominent source of error is likely to be the differences in measurement location. Video-based results are obtained just seaward of the physical measurement location. Especially high waves tend to peak just in front of the breakwater, regularly exceeding the upper side of the flume window. At the breakwater crest the waves break or spread across the crest, resulting in lower water levels more landward.

The performance of the deep image segmentation algorithm on the rubble mount tests (not shown) was reasonably well. However, the algorithm tends to classify splashing waves and water drops as waves, resulting in an overestimation of the local water level. The absolute mean error is consequently much higher compared to the tests with a smooth slope. From this first application of deep learning, numerous improvements to the algorithm are still at hand. It is therefore expected that results will improve significantly for more turbulent waves by expanding the training dataset and optimizing the network design and inference.

2.5.1.1.2 Applicability

The applicability of the algorithm is mainly dependent on the degree of automation, its robustness during execution and its time consumption. None of these aspects have been investigated in this study in particular, but a non-exhaustive summary is given for future reference.

The deep image segmentation algorithm appeared to be highly robust, but also highly computational intensive. Only by using GPU enabled machines, model training could be performed within a few hours. In the case of deep learning, no pre-processing of the images

is required as all features are trained along with the model. The computational effort is therefore fully applicable to the model training and thus a one-time effort. Segmentation of unseen timestacks only takes a few seconds, making the deep learning approach particularly interesting for real-time application.

The current algorithm is also highly parallelizable. For example, if multiple cameras are used to cover a larger section of the flume, or a higher measurement frequency is used to extract more advanced physical parameters, a computational cluster of cloud could be used for processing without many changes to the algorithm.

For further applications of automated semantic segmentation algorithms, the collection of ground truth data is paramount. Collection of ground truth data has two objectives: 1) to expand the applicability to various types of tests without training a model for each separate test, and 2) to provide data for detailed testing of the algorithm by first comparing detected wave shapes with manually annotated wave shapes that have not been used for algorithm training. Also, the monitoring of the algorithm performance on ground truth data is important to ensure confidence in the algorithm over time.

2.5.4. Recommended protocol

This study suggests that a real-time operational application of an automated deep image segmentation algorithm to detect local water depths and overtopping volumes in a wave flume is feasible. The required measurement protocol is defined in 5 steps:

1. Collect video data of the area of interest.
    a. Video data should be taken from the flume side, perpendicular to the flume wall. A flume with transparent walls is therefore required.
    b. Markers on the flume wall can be used to keep a fixed reference frame at all times. The centre of mass of circles with a contrasting colour is easy to detect (e.g. red dots on a white background).
    c. Measurement frequency should be chosen such that a passing wave is captured in a sufficient number of frames. 20 frames per wave are a good starting point.

    In our case the video covered about 50 cm of the flume, of which 25 cm was our area of interest for overtopping. With bores traveling up to 1.5 m/s, a single bore was in the field of view for 0.25 / 1.5 = 0.17 s. Therefore, we needed a measurement frequency of at least 20 / 0.17 = 117 Hz.

    d. Optimize the data stream. Most high-speed cameras allow for image masking, preventing areas of the image that are not of interest to be written to disk.
2. Convert the video footage to timestacks.
    a. Determine the periods of interest in the video footage.

    In our case we used 50 waves from the top-100 waves with maximum flow depth at the breakwater crest.

b. Extract timestacks for these periods using a fixed time frame. One timestack for each pixel location along the flume axis can be extracted, but this might not be necessary for an accurate description of the flow depth in space.

In our case we used a time frame of 2 seconds or 300 frames around the peak flow depth for each wave. We used one timestack every 10 pixels along the flume axis or 0.5 cm.

c. Optimize the data stream. Using JPEG images rather than PNG results in a slight quality loss, but saves significant amounts of storage space and bandwidth.

3. Segmentate the timestacks using the deep image segmentation algorithm. The result is a binary image with the same size as the original timestack and indicating what pixels do belong to the wave and what pixels do not.

4. Extract spatiotemporal flow depths from the binary images.

   a. The contour of the mask is of interest. Therefore, a contour algorithm is applied to the binary image. From all detected contours, the largest is taken.

   b. All points in the largest contour are ordered based on time. For each moment in time, the highest point that is part of the contour is taken. For all moments in time that are not in the contour description, a *NaN* value is used. The result is a time series of the local water level.

   c. All time series of all timestacks corresponding to a single wave are stacked in order to obtain a spatiotemporal description of the water level per wave.

   d. Subtract the bed level from the water level to obtain a spatiotemporal description of the local flow depth.

5. Extract physical parameters from the spatiotemporal flow depths (Figure 43).

   a. The time-averaged bore speed can be estimated by determining the slope of a linear fit of the rising part of a representative flow depth contour in space and time.

   In our case we used the 2-cm flow depth contour as this was the smallest contour that allowed for a proper linear fit. It therefore represents the steady head of the runup tongue.

   b. The overtopping duration can be determined by measuring the period between the up and down crossing of a representative flow depth contour at a location of interest.

   In our case we used the 2-cm flow depth contour up and down crossing with the onset of the breakwater crest (origin of the reference frame). The location is chosen arbitrarily.

   c. The time-averaged flow depth can be determined by averaging the flow depth over the overtopping duration at a location of interest.

   d. The overtopping volume at a location of interest can be estimated from the product of the time-averaged bore speed, the overtopping duration and the time-averaged flow depth.

2.6 WAVES – ICE – STRUCTURE INTERACTIONS

There are three parts in Loads on Structure and Waves in Ice (LS-WICE): ice fracture under wave actions, wave attenuation/dispersion in broken ice covers, and ice-structure interaction under wave conditions. A range of monochromatic waves propagated through level ice, continuous or cut into regular pieces. Wave measurements were monitored with pressure transducers and ultrasound sensors. Results from the data analysis are useful for developing tools for field applications.

2.6.1 Objective description

The study comprises the following objectives:

- Determination of the dampening effect of ice on wave propagation (Cheng et al., 2017);
- Analysis of the motion behaviour of ice floes in waves;
- Analysis of ice-breaking due to waves (Herman et al., 2017a,b);
- Measurement of combined ice and wave loads on a structure (Tsarau et al., 2017).

2.6.2 Tests and experiments

The test program was executed in open water without ice and for four different ice sheets. Each of these tests had different purposes. The open water case was performed to characterize the wave tank behaviour and to calibrate all sensors. Ice sheet no. 1 was constructed to perform the break-up test. Ice sheets no. 2 and no. 3 were used to test wave attenuation and dispersion under different monochromatic waves. Ice sheet no. 4 was produced to test ice-structure interaction in the presence of a wave field. A cylindrical structure (0.69 m diameter) was anchored in a fixed location in ice sheet no. 4 to measure the ice and wave forces acting on the cylinder.

The wave field was monitored by two types of sensors: ultrasound and pressure, one determined directly the surface elevation and the other the dynamic pressure which was related to the surface elevation. The ultrasound sensors were UltraLab (model ULS Advanced USS 13-HF, IP65, M30x1.5). The pressure transducers included ten BD (model LMP307, 0.1 bar range), and two Omega (PX437 and PX438, range 0.14 bar range). A Qualisys Motion Capture System together with markers that were placed on the ice along the central axis of the tank to monitor the motion of ice surface. In order to record the time evolution of the ice breaking pattern, large parts of the ice sheet were continuously monitored with an AXIS camera mounted at the ceiling and two sideward-looking GoPro cameras mounted at the walls. Additionally, static images of the entire ice sheet were taken with a Canon EOS 550D digital reflex camera after two tests in which major ice breaking was observed in order to determine the resulting floe-size distribution (FSD).

2.6.3 Results and discussion

The ice sheet no. 1 was used for the breakup test. For a constant wave period, the wave amplitude was increased stepwise until a major breakup of the ice sheet occurred. Subsequently, a number of combinations of wave period and amplitude values were used to obtain further breakup into smaller ice floes. After each significant breakup event, high-resolution images of the ice sheet were taken in order to determine the resulting FSD. An example result of the FSD analysis is shown in Figure 48 (see also Herman et al., 2017a, b).

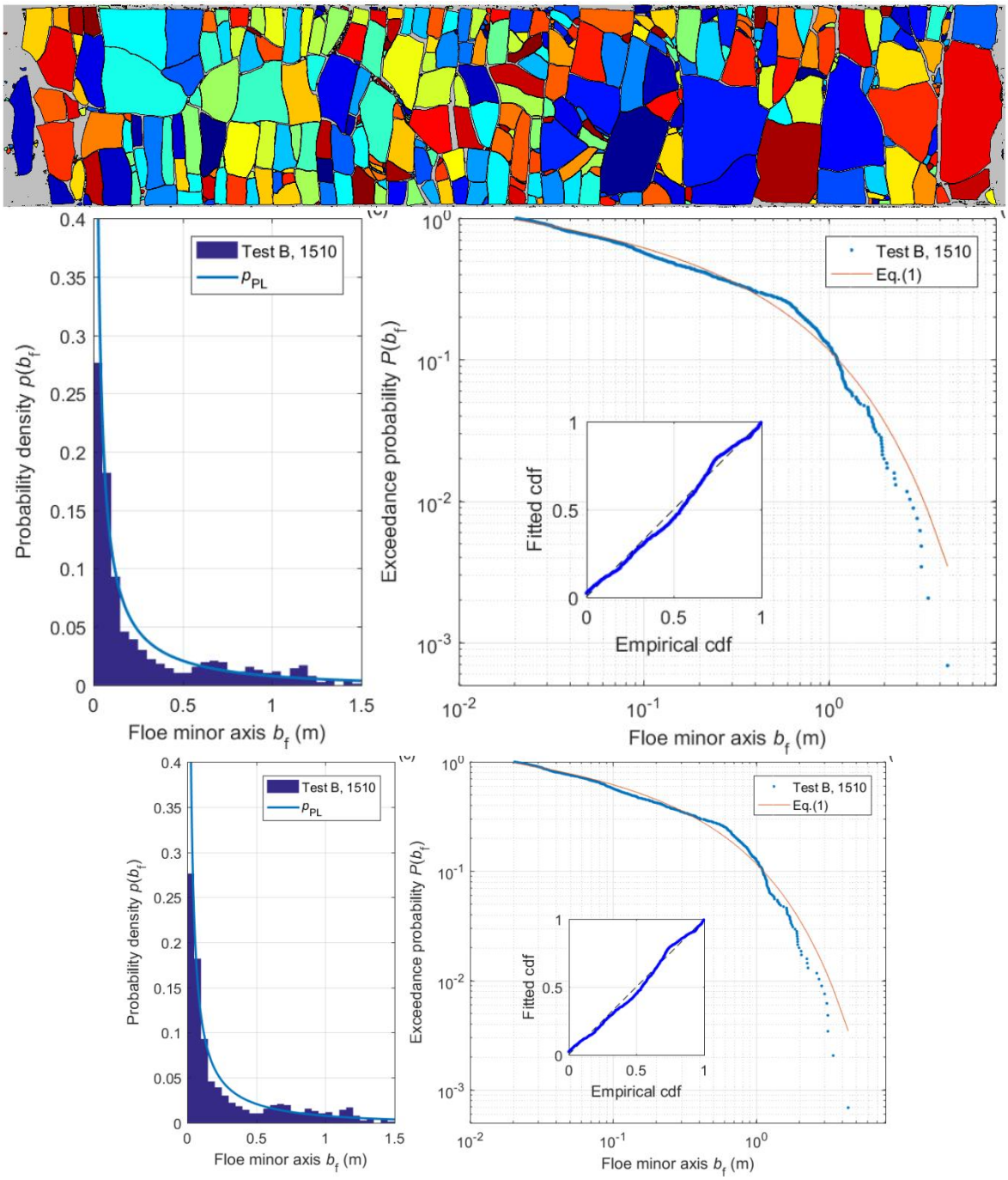

Figure 48 : Example results of the FSD analysis in ice broken by waves: ice-floe map obtained from digital images of the ice sheet (top); corresponding pdf and cdf of floe sizes (bottom).

The resulting data set is one of the very few existing data sets on ice broken by waves, in which both wave and floe-size information is available, together with video recordings of the breaking process itself. This type of data is necessary to answer a longstanding question about the relationships between the wavelength and sea ice properties on the one hand, and the dominant floe size resulting from flexural ice breaking on the other hand. Theoretical and numerical studies suggest that the ice thickness and elastic modulus determine the floe size, whereas many parameterizations of the wave-induced sea ice breaking make an assumption that wavelength is the only variable determining the maximum floe size. Comprehensive data sets like this one are necessary to solve

this issue. At the same time, the results demonstrate that even data from tests performed under controlled laboratory conditions are often difficult to interpret due to many hard-to-eliminate effects (see further section 2.6.4).

For ice sheet no. 2 and 3, wave dispersion and attenuation were measured. Figure 49 shows an example of the change of wave speed and amplitude when the floe sizes change. These data help to device an empirical formula to predict the floe size effect on wave speed and attenuation level in all scales. Presently there is no such formula available.

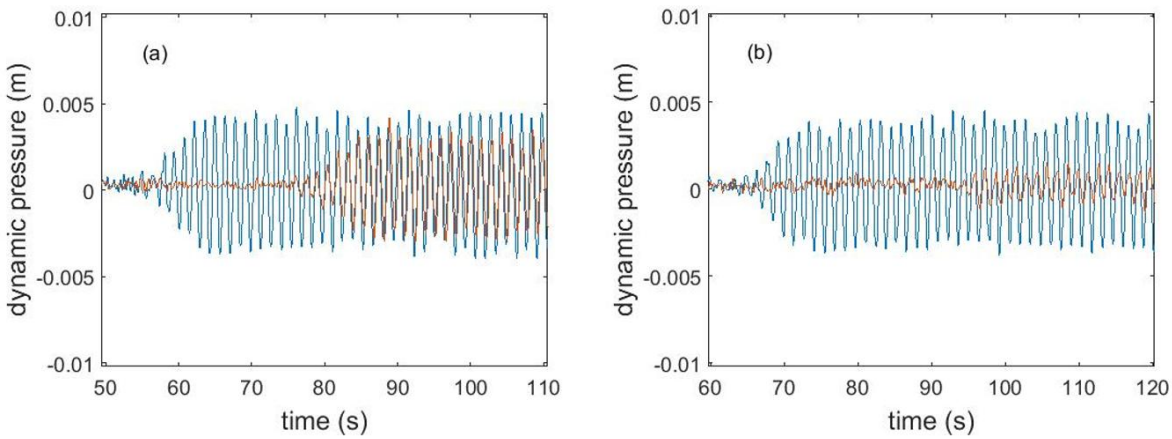

Figure 49 : Time series of two pressure sensors for a 1.4s wave through regular floes of size: (a) 1.5 m (b) 0.5 m.

For ice sheet no. 4, both the response of a wave-driven ice floe near the structure and the forces on the structure due to both waves and ice impacts were measured. Figure 50 shows the experimental setup and an example of typical time series obtained from the measurements.
It was found that the surge response amplitude operator (RAO) of the ice floe due to waves was not significantly different from test 1 for all considered wavelengths. The variation of this RAO was not sufficient to solely account for the variation of the impact forces on the structure and impact occurrence in the experiment. Floe-floe collisions seemed to affect impact occurrence as well. Among the parameters influencing the impact force, the following were identified:

- wave height and period (also wavelength for shallow water);
- ice-floe kinematics in waves, including momentum exchange due to floe-floe interaction;
- interaction area between the structure and the ice floe.

The effect of ice properties were not assessed in this study. A major difference of this experiment compared to previous experiments on impacts of a wave-driven ice mass on a structure is the utilisation of a wave tank that was fully covered with ice floes, instead of considering only one isolated ice mass and a structure as in some previous studies. Full ice coverage ensures a better representation of MIZ conditions and enables floe-floe interactions to be represented as well as the wave dispersion effects of ice-covered water.

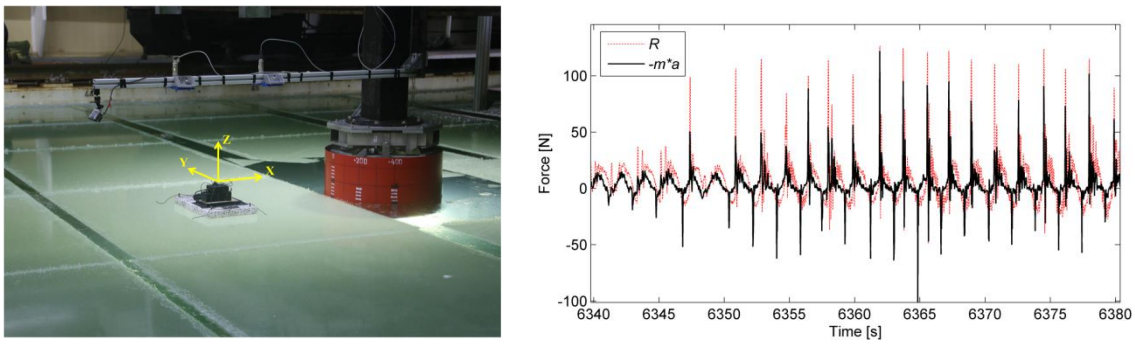

Figure 50 : Experimental setup for measuring combined ice and wave loads on a structure (left) and an example of the measured load history (right) in one of the tests: the surge force on the structure (in red) and the inverse surge force on the ice floe (in black).

2.6.4 Recommended protocol

1. Our results from the breakup test shows that in similar tests it is recommended to use relatively short wavelengths – sufficiently short so that only insignificant wave energy reaches the down wave end of the ice sheet. This would reduce the effects of reflection from the end of the tank such that they become negligible. In our tests, relatively long waves were used and the attenuation was weak, therefore the reflected waves had a significant influence on the breaking patterns, making the analysis and interpretation of the results difficult (in the initial phases of the experiment, cracking was observed not at the ice edge, but in the middle of the ice sheet, and those initial events influenced the evolution of the FSD throughout the experiment). Appropriate wavelengths can be determined in preliminary attenuation tests with a continuous ice sheet and very low wave amplitudes (in order to prevent undesired breaking).

2. The Qualisys system is very valuable for measuring the vertical motion of sea ice, and thus wave attenuation (in our experiments, the Qualisys data are less noisy than the data from the pressure sensors). However, at high ice concentrations, i.e., when the amplitude of the horizontal motion of ice floes is constrained, the data cannot be used to obtain information on floe collisions. In this case, when instantaneous floe accelerations are large, but displacements very small, accelerometers placed on the ice are the only reliable source of information on floe collisions. This is relevant for estimating the restitution coefficient of ice floes, and thus for estimating energy losses due to inelastic collisions of ice floes, which is one of the (poorly understood) mechanisms contributing to wave attenuation in broken ice sheets.

3. There are many theoretical studies of how an ice cover might attenuate waves and change their dispersion relation. For example, Squire (2007) provided a review of the theories up to that publication time. These theories have only been partially confirmed by a number of field experiments. Meylan et al. (2014) reported attenuation in the order of 10^{-5} (m^{-1}) in the Southern Ocean marginal ice zone. Doble et al. (2015) reported attenuation in the order of 10^{-3} (m^{-1}) in the Weddell Sea. The ice conditions of these two studies were very different from each other, and also very different from the much earlier study of Wadhams et al. (1988), in which they reported several field studies in the Arctic marginal ice zone including Bering and Greenland Seas. The range of attenuation was from 10^{-5} – 10^{-4} (m^{-1}). These studies strongly suggested that wave attenuation is a result of the combination of ice type and floe sizes. Data on wave speed change is very difficult to obtain in the field. To isolate ice

effect on wave propagation from other mechanisms such as wind wave generation, nonlinear wave-wave energy transfer, and wave breaking, laboratory studies are necessary. The present study demonstrated a systematic approach to determine floe size effect on wave propagation. Attenuation from other mechanisms such as turbulence under ice covers, and ice floe interactions, need to be carefully studied in the laboratory in the future.

4. Detailed results of this study are being prepared for a journal publication. Wave-ice interaction may include many physical mechanisms as discussed in Shen and Squire (1998). In this experiment, the total attenuation from all processes present in the experiment is measured. Likewise, wave dispersion data are also the result of coexisting mechanisms. The dataset can potentially be used in many future studies.
5. To scale up the results from a laboratory size wave and floes to the field, we need to determine the dominant length scales that can link the laboratory to the field conditions.

Publications already appeared in the literature are listed in the references (Cheng et al., 2017, Herman et al., 2018, Tsarau et al., 2017).

2.7 VELOCITY MEASUREMENTS IN HIGHLY VARIABLE SPACE AND TIME FLOWS

2.7.1 Objective description

The technical challenge in this part of the project is to carry out velocity measurements in a flow with highly variable space and time scales. To analyse such flows, double-averaging, i.e. temporal averaging (classical Reynolds-averaging) combined with spatial averaging, is often required (Nikora et al. 2007). Time-averaging is easy to carry out with classical measuring tools (ADV, LDV, PIV). In turn, space-averaging in a plane can be performed easily with a PIV technique, provided the length scale over which the space-averaging has to be performed is smaller than the camera field of view. Volume-averaging is much more difficult to implement in practice. It is possible to use tomographic 3D-3C PIV (three-dimension-three-component), but this method requires a very complex apparatus and the size of the measuring volume cannot easily exceed 10 cm^3 (e.g. Schröder et al. 2011, Gao et al. 2013). Single-point measurement systems like ADV or LDV can also be used for space-averaging, when measuring over a sufficiently refined mesh, but the measurement time can be excessively long. Another way to perform volume-averaging is PIV scanning, with a number of different approaches being developed over recent years (Brücker 1996, Liberzon et al. 2004, Albagnac et al. 2014). The objective here is to present a new technique for 3D-2C PIV scanning which is relatively simple to set-up and yields accurate and reliable results. In addition to a classical 2D-2C PIV system, this technique requires a linear motor with accurate positioning and a telecentric lens for the camera. One advantage of this 3D-2C PIV scanning technique is that the measuring time is relatively short, compared to space-averaging with single-point measuring devices. However, the processing time (including pre-processing of the PIV image, PIV correlation and post-processing of the vector fields) is significant and has to be done using a computing center.

Note that combining space- and time-averaging yield a large volume of data, especially if the space and time scales of the flow vary across a broad spectrum. Once the technical difficulties relative to the experimental set-up have been overcome, data storage is in fact often the limiting factor, at almost all levels of the measurement chain (local camera storage, local computer storage, long-term data storage).

In the frame of Hydralab+, the 3D-2C PIV scanning technique was used to investigate complex flows in an open channel flume. The flows were designed to model an overflowing river with a smooth main channel adjacent to a rough floodplain.

2.7.2 Tests and experiments

The experiments were performed in a 26 m long and 1.1 m wide glass-walled open-channel flume at IMFT, Toulouse. The flume has a constant slope of 3.1 mm/m. As sketched in Figure 51, one half-side of the bed is smooth glass and the other side is covered with an array of cubes of side h = 40 mm and arranged in square configuration. The elementary pattern of this arrangement in the xy-plane is a 91.5 x 91.5 mm^2 square, yielding to a solid volume fraction of n = 0.19. We note x the longitudinal direction parallel to the bed, y the transverse direction with y = 0 at the interface between the array and the smooth bed (the width of the array being 6 entire length of the elementary pattern) and z the normal to the bed, with z = 0 at bed level.

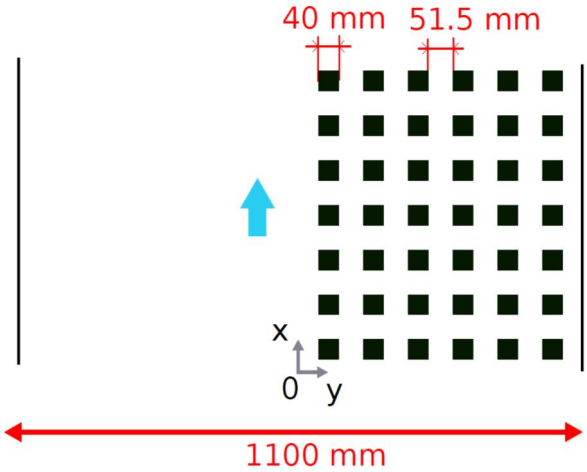

Figure 51 : Top view of the channel bed configuration.

Velocities in the longitudinal (*u*) and vertical (*w*) directions are measured using scanning Particle Image Velocimetry (scanning PIV). The measurement setup, placed at x = 19.5 m from the channel inlet, is sketched in Figure 52. A continuous laser mounted on a telecentric lens generates a parallel laser sheet of 2.7 mm thickness. The laser sheet enters from the bottom of the channel after being reflected by a mirror orientated at 45°. This 45°-mirror is mounted on a linear motor that can travel with high speed and high positioning accuracy in the *y*-direction. The laser sheet in the *xz*-plane is viewed by a camera placed at the side of the flume. A second telecentric lens mounted on the camera objective prevents parallax effects on the image, i.e. for different *y*-positions of the mirror the image calibration (pixel-to-millimetre conversion) is unchanged. The water is seeded with 60 µm polyamide particles with a density of 1.03.

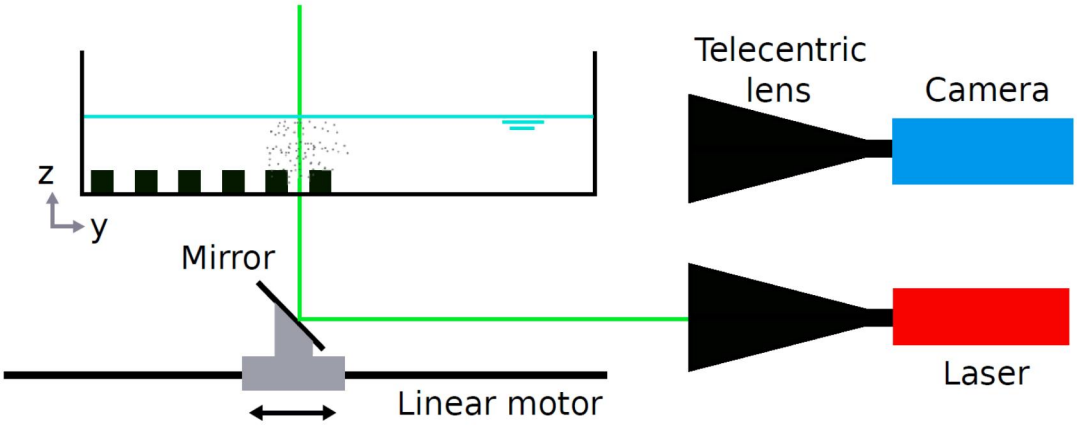

Figure 52 : Set-up of the first campaign.

This arrangement enables a three-dimension-two-component (3D-2C) velocity measurement. The frame rate of the camera and the travelling velocity of the linear motor were chosen such that the two laser sheets of two consecutive frames overlapped (see below). The PIV correlation is then computed between these two successive frames. Measurement accuracy is reduced as the overlap that exists between the two consecutive frames is decreased, because fewer particles will be present in both frames. However, a high degree of overlap results in more images for the same scanning length, which creates data storage problems. Thus, a compromise had to be made and an

overlap of 85 % was chosen. Figure 53 shows the rate of false vector with increasing overlap. For 85 % overlap, the false vector rate is comparable to a classic 2D-2C PIV (100 % laser sheet overlap).

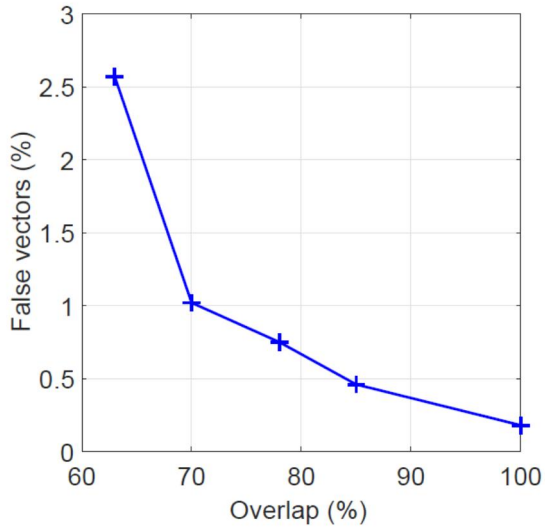

Figure 53 : Rate of false vectors.

If we note *e* the laser sheet thickness and *dy* the displacement of the laser sheet between two frames, then the overlap *B* is defined by $B = (e - dy)/e$. The frame rate *f* of the camera is calculated by $f = U_f/dl$, where U_f is the typical flow velocity and *dl* is the displacement of a particle between two frames, corresponding to a chosen pixel displacement (e.g. 15 pixels). In the time delay $dt = 1/f$ between two frames, the laser sheet must travel a distance *dy*, thus the motor velocity is given by $U_{mot} = dy/dt = fe(1 - B)$.

In this configuration, it is necessary to trigger the camera with the motor. In practice, the motor is first accelerated along a velocity ramp before reaching the constant velocity U_{mot}. As soon as the motor velocity reaches the plateau U_{mot} – which must occur at the *y*-position expected by the operator – the motor sends a signal to the camera to begin the frame acquisition. This triggering is relatively easy to set up. It is also possible not to trigger the camera if there is a marker on the image (e.g. a border) for identifying the *y*-position of the first frame.

Because the depth of focus of the camera telecentric lens was limited to 200 mm, the cross-section was divided in four parts, in each of which a scanning measurement was made. These four measuring volumes were then merged together to get the complete cross-section. Note however that for technical reasons the region $y > 410$ mm could not be measured; moreover, because of reflection of the laser sheet on the free-surface, the last top 15 mm near the free-surface could not be measured too. The measuring volume is about 200 mm long in the *x*-direction.

Three test cases were investigated, with different cube submergences: two submerged cases with $D/h = 2$ and 1.5 (test cases S2 and S1), where *D* is water depth; and an emergent case with $D/h = 0.8$ (test case E). Table 13 summarizes the flow conditions for the three test cases: total discharge *Q*, subsection bulk velocity $U_{Q,i}$ (i=a for the cube array and i=s for the smooth part), as well as Froude and Reynolds numbers in each subsection.

For each test case, about 110 scans of the measuring volume have been made. Each scan can be considered as a statistically independent sample since the time between two scans exceed the highest time scale of the flow. These 110 samples were sufficient to obtain relatively good converged values of mean velocities and Reynolds stress tensor components.

The PIV images were processed with a free software developed at IMFT called C-PIV-IMFT. This is a classical PIV correlation algorithm using fast Fourier transform. The software C-PIV-IMFT is parallelised such that the calculation time can be considerably reduced if a high number of processors are available. The data were processed with the academic regional computing center *Calmip* (https://www.calmip.univ-toulouse.fr). For this first campaign, about 3 million images were processed (including not only scans, but also fix-plan measurements), corresponding to a data volume of 6 To. Using 240 processors in parallel, the calculation time was about 150 hours. With a single processor, the equivalent calculation time would be 36000 hours = 1500 days.

Table 13 : Flow conditions of the three test cases S2, S1 and E.

Test case	D/h	D (mm)	Q_{tot} (Ls^{-1})	$U_{Q,a}$ (cms^{-1})	$U_{Q,s}$ (cms^{-1})	Fr_a	Fr_s	Re_a	Re_s
S2	2	80	45.5	23.7	78.9	0.28	0.89	78 500	252 400
S1	1.5	60	26.2	16.8	66.1	0.17	0.86	32 000	158 500
E	0.8	32	10.5	11.4	52.8	0.12	0.94	8 700	67 600

A second campaign investigated the same three test cases as in the first campaign, but this time the laser sheet was horizontal. The aim was to have access to the lateral component of the velocity *V*. The lateral velocity is particularly important in these flows since strong coherent structures with vertical axes are present at the interface between the smooth bed and the cube array. The corresponding set-up is sketched in Figure 54. Compared to the set-up of the first campaign, two other mirrors were needed: one for deflecting the laser sheet in a horizontal plane and the other one for viewing the laser sheet with the camera at the side of the flume.

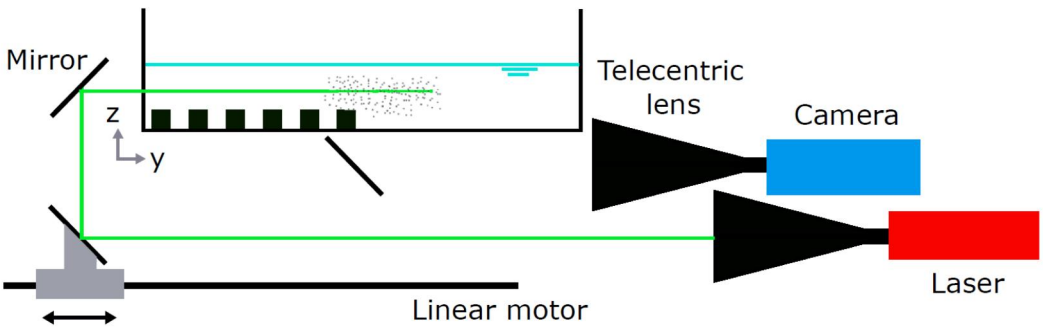

Figure 54 : Set-up of the second campaign.

From the metrological point of view, another technique was used for this campaign. The laser was a two-cavity pulsed laser. The frequency of the two-pulse shot was adjustable, as well as the time

delay between the two cavities. This solution enables to decouple the choice of the frequency of the frame-doublets f_D and the choice of the delay *dt* between the two frames of the same doublets.

The advantage of this variant is that a reduced number of images can be taken for the same scanning period. The drawback is that the triggering is more difficult. For the present case, motor, camera and laser must be synchronized simultaneously. The easiest solution is probably to choose one element (for example the motor) to trigger the other two elements, but this is not always possible due to the operation of the different devices. In our case we used a frequency generator coupled with frequency dividers to trigger the three elements.

In this experiment, 2000 scans of the measuring volume were obtained for each flow, with the same data volume as the first measurement campaign. This corresponds to 2000 statistically independent samples, which improved the convergence of the mean velocity and Reynolds stress fields compared to the first campaign.

2.7.3 Results and discussion

The scanning PIV measurements enable a complete overview of the flow organization in the channel cross-section to be obtained. Figure 55 shows the distribution of longitudinal velocity and longitudinal turbulence intensity in the cross-section for the three test cases. Both quantities are spatially averaged in the longitudinal direction along a pattern length. The spatial average here is intrinsic, i.e. achieved only on the volume of fluid (Nikora et al. 2008). The flows investigated are characterized by a mixing layer that develops at the interface between the smooth bed and the cube array which is generated by the high difference in velocity between these two flow regions. The mixing layer induces strong turbulence production at the interface, which can be clearly seen on Figure 55 (right).

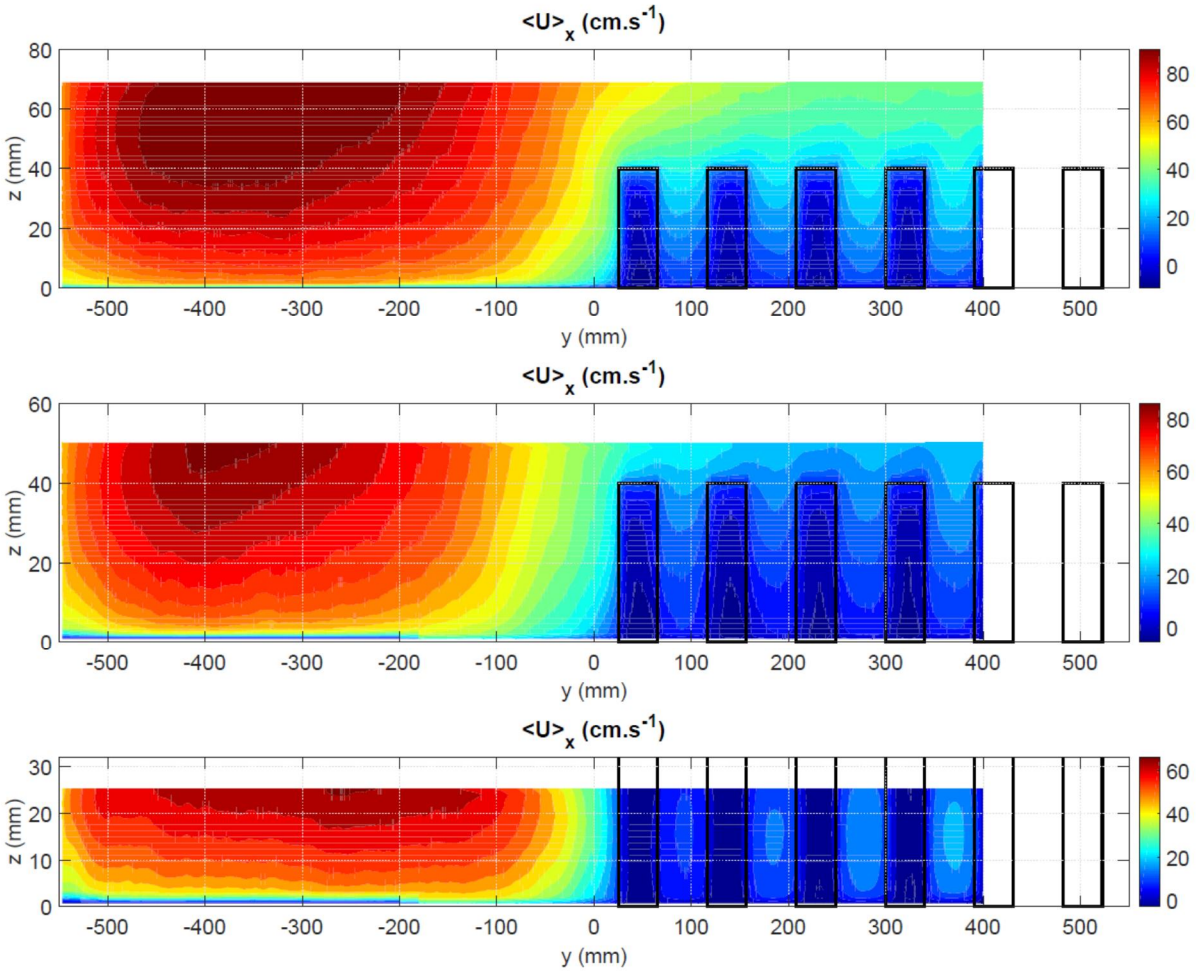
<U>x (cm.s-1)
z (mm)
y (mm)
<U>x (cm.s-1)
z (mm)
y (mm)
<U>x (cm.s-1)
z (mm)
y (mm)

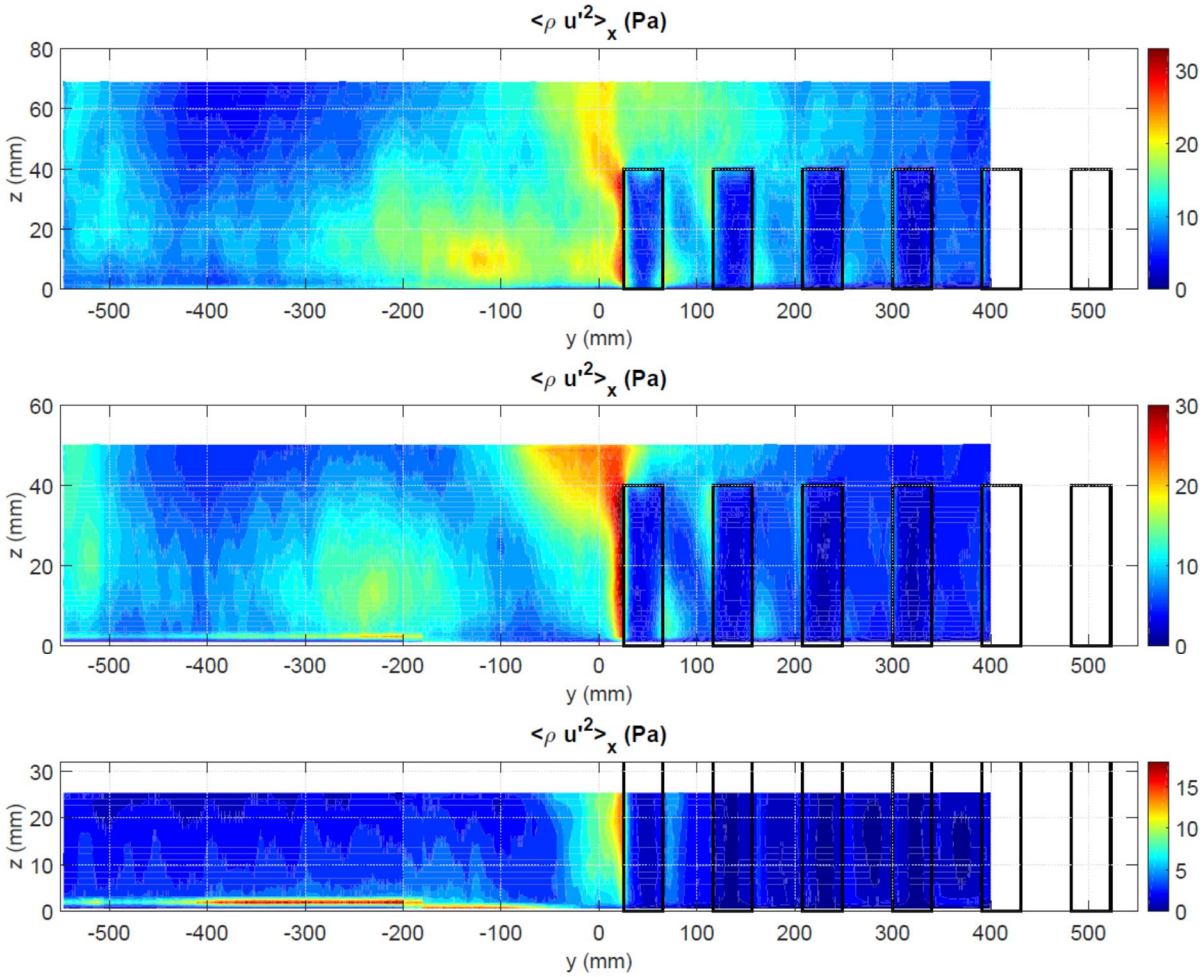

Figure 55 : Cross-section distribution of mean longitudinal velocity (left page) and longitudinal turbulence intensity (right page) for test cases S2 (top), S1 (middle) and E (bottom). The two quantities are spatially averaged in longitudinal direction.

The mixing layer is not the only source of turbulence production in these flows. Turbulence production also comes from the cube wakes and from the bottom and wall friction. Whereas the cube wakes and the bottom friction are associated with turbulent length scales that are smaller than the water depth, the mixing layer produces turbulence length scales that are one order of magnitude higher than water depth, as revealed by time-resolved measurements. In order to identify the relative contribution of the small scale and the large-scale fluctuations in the overall turbulence fluctuation, a spatial smoothing of the velocity fluctuations has been performed. Figure 56 shows for test case S2 the longitudinal (left) and vertical (right) turbulence intensity after spatial smoothing. The smoothing occurs over a cubic box of increasing size: 1.3 mm, 5.2 mm, 10.4 mm, 18.2 mm and 39.0 mm (from top to bottom). Note that the first smoothing box corresponds to no smoothing since 1.3 mm is the step of the measuring mesh.

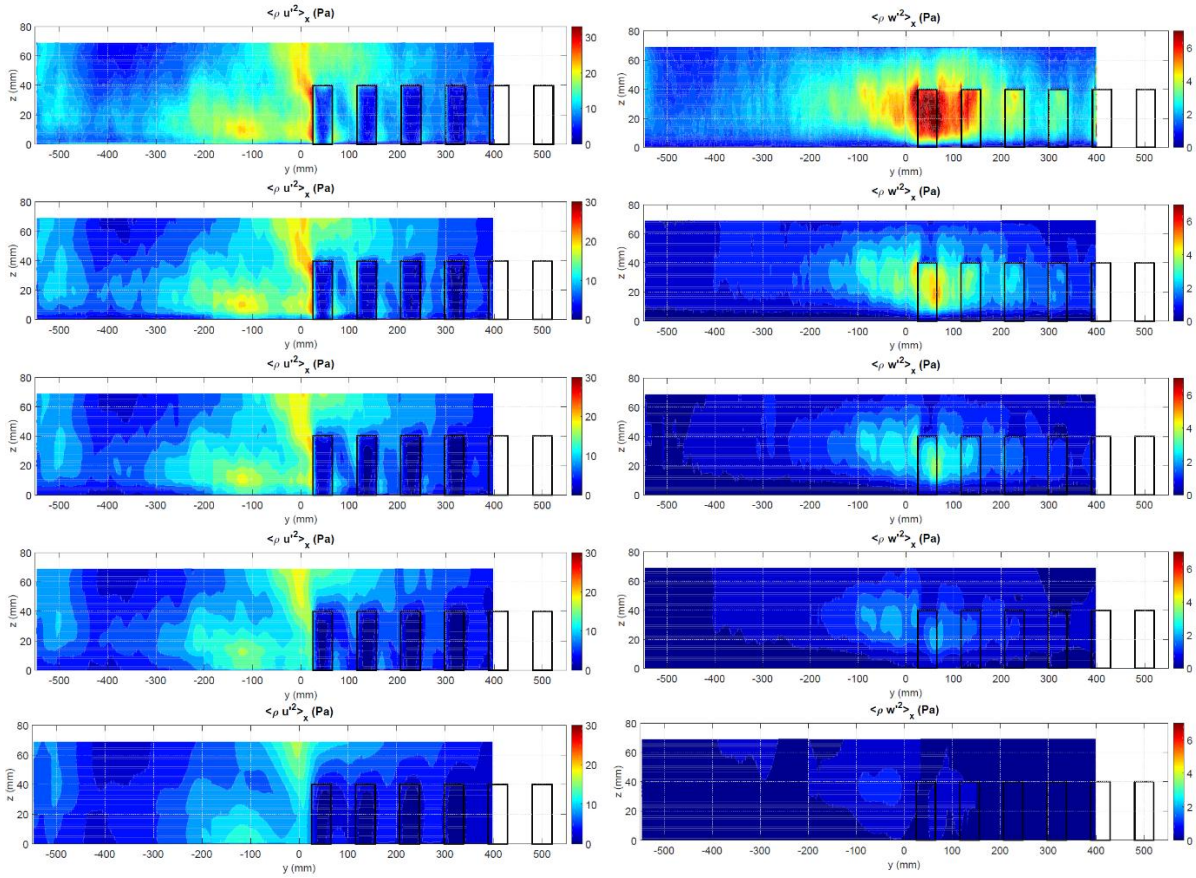

Figure 56 : Longitudinal (left) and vertical (right) turbulence intensity after spatial smoothing of the velocity fluctuations. The smoothing occurs over a cubic box of increasing size 1.3 mm (no smoothing: accuracy of the measuring mesh), 5.2 mm, 10.4 mm, 18.2 mm and 39.0 mm (from top to bottom). Test case S2.

For large smoothing boxes, only the large-scale fluctuations are left. For the longitudinal turbulence intensity (left side on Figure 56), large-scale fluctuations are located at the interface between the smooth channel and the cube array and mostly above the cubes, corresponding to a well-developed mixing layer in this area. By contrast, the high turbulence intensity located close to the cube surface disappears after smoothing, indicating that it is related to wall friction and not to the mixing layer. Indeed, such a shallow mixing layer is associated with coherent turbulence structures of vertical axes that induce large-scale quasi-periodic oscillations of the lateral and longitudinal velocity components (White and Nepf 2007, Dupuis et al. 2017). However, such a mixing layer does not generate coherent fluctuations for the vertical velocity component. Thus, the vertical turbulence intensity (right side of Figure 56) almost completely disappears after smoothing, indicating that the fluctuations of *w* are mainly related to friction and cube wakes.

The data obtained by the scanning PIV technique also enable to plot transverse profiles of flow quantities at fix elevation *z*. This is of particular importance for studying the mixing layer since the properties of the mixing layer much depends on the shape of the lateral profile of *U* (Proust et al. 2017, Dupuis et al. 2017). Figures 57 and 58 show the transverse profiles of mean longitudinal velocity (left) and longitudinal turbulence intensity (right) at fix *z*-elevation above and below the cube height for the three test cases. Consider first the longitudinally averaged profiles, noted $<.>_x$ (blue and red lines). Below the cube height, the cube wakes are clearly visible and characterized by a

strong dip in the velocity and by increased longitudinal turbulence along the side faces of the cubes. Sufficiently above the cube, there is no more spatial variation due to the presence of the cubes. In order to smooth out the spatial variations due to the cube and let only the spatial variations due to the horizontal mixing, a lateral spatial averaging over a cube pattern length (91.5 mm) was done. These quantities are denoted by $<.>_{x,y}$ and correspond to the green and black lines in Figures 57 and 58.

It can be observed that the double averaged velocity $<U>_{x,y}$ within the cube array for test case E decreases from the sidewall towards the smooth bed. This is not an ordinary observation, since a mixing layer generally involves an acceleration of the low-velocity side and a deceleration of the high-velocity side. This fact can be explained by the perturbation of the flow in the free corridor through the action of the mixing layer. For outer cubes away from the interface, the flow in the free corridor in mainly unidirectional in the *x*-direction. Near the interface however, strong sweeps and ejections, that characterize mixing layers (White and Nepf 2007), induce high-intensity lateral cross-flows in the main corridors, such that a unidirectional flow cannot develop. The fact that $<U>_{x,y}$ decreases in the cube array for test case S2 when going towards the interface indicates that this latter effect (perturbation of the flow in the free corridor by the mixing layer) is dominant compared to the mixing effect of the mixing layer (inflow of high-speed fluid), except very close to the interface ($x < 50$ mm).

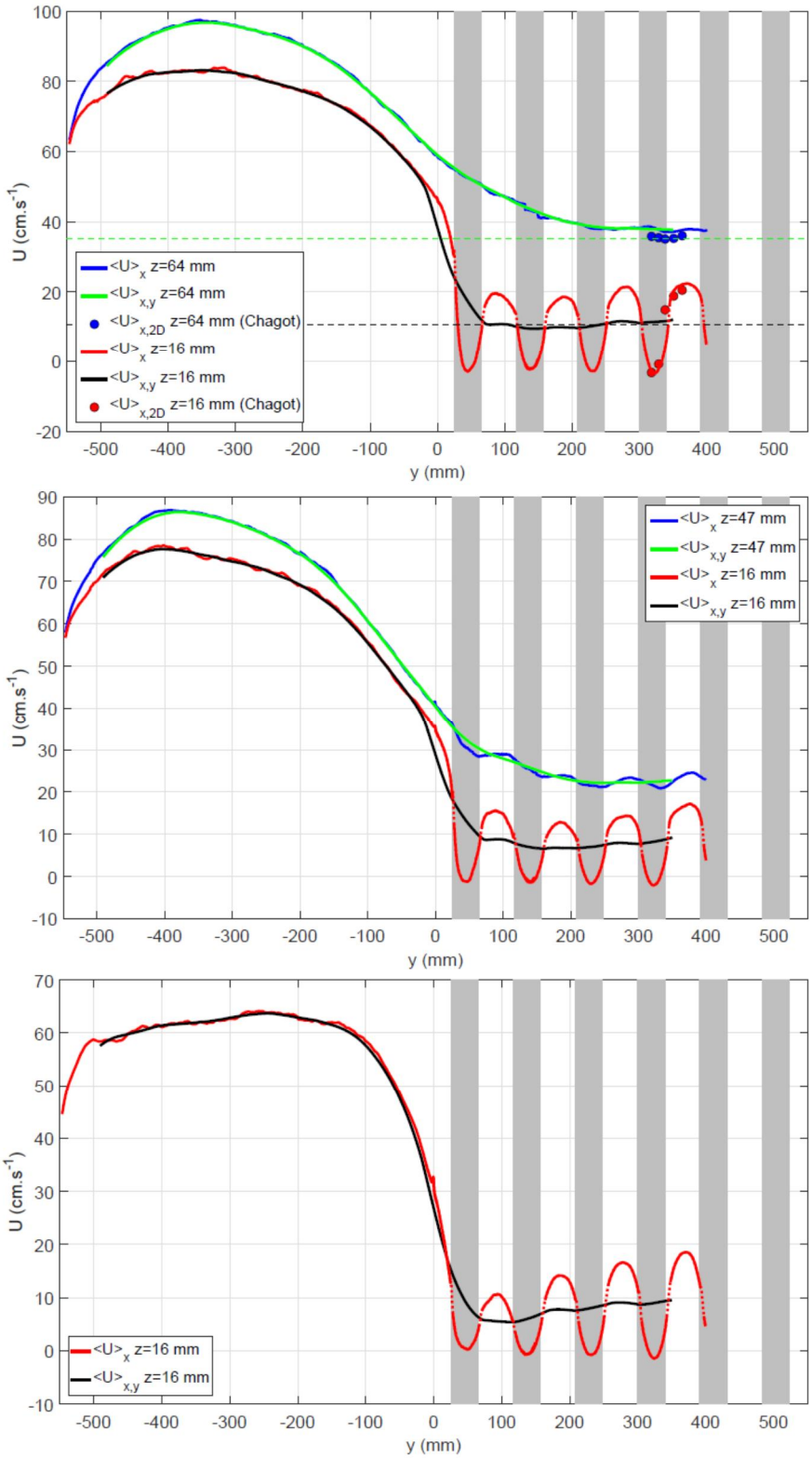

Figure 57 : Transverse profiles of mean longitudinal velocity at fix z-elevation above and below the cube height. Test cases: S2 (top), S1 (middle) and E (bottom). For test case E, there is no flow above the cube. The quantities are either only longitudinally averaged ($<.>_x$) over both longitudinally and and laterally averaged ($<.>_{x,y}$).

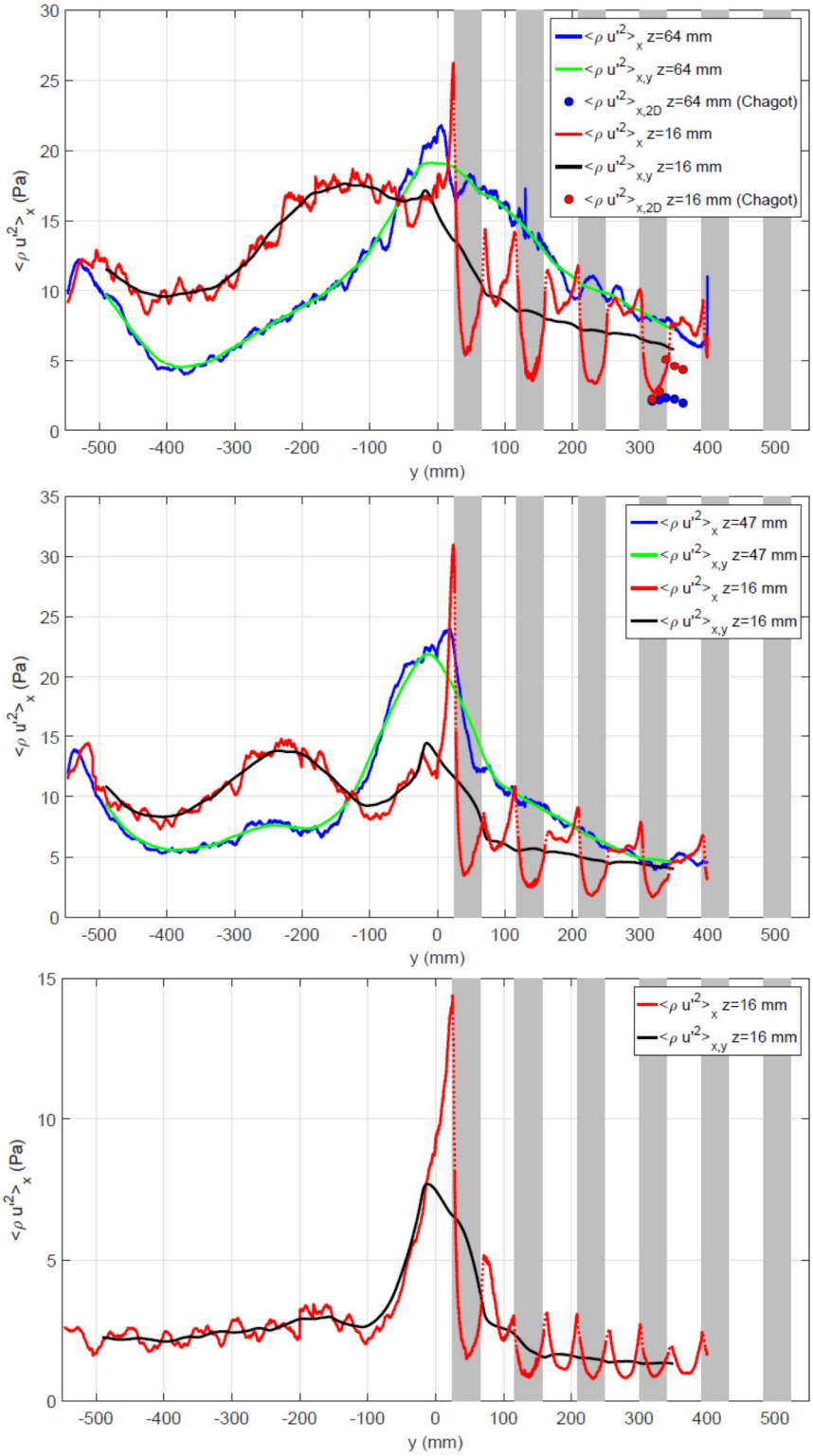

Figure 58 : Transverse profiles of longitudinal turbulence intensity at fix z-elevation above and below the cube height. Test cases: S2 (top), S1 (middle) and E (bottom). For test case E, there is no flow above the cube. The quantities are either only longitudinally averaged (<.>$_x$) over both longitudinally and and laterally averaged (<.>$_{x,y}$).

2.7.4 Recommendations

We recommend choosing the second technique that was presented above, i.e. with a pulsed laser. The main advantage over the first approach is that the acquisition frequency of the bursts, f_D, is independent of the time delay *dt* between the two frames inside a burst. Compared to the first technique presented (continuous laser), it allows to reduce the number of images recorded within one scan and therefore, it yields to an increase of the number of 3D-2C velocity samples.
The protocol reads:

- Determine the size of the PIV interrogating window according to the expected resolution, the particle size and the size of the camera sensor;
- Choose a laser sheet thickness *e* that is of the order of the interrogating window size (in order to have a cubic interrogating box);
- Choose the time delay *dt* according to the typical flow velocity and the expected pixel displacement (e.g. 10 pixels);
- Choose a frame overlap *B* at about 85 %;
- The motor velocity is then $U_{mot} = e(1 - B)/dt$;
- Determine the frame-doublets frequency f_D according to the expected spatial resolution and the available camera data storage (at least 1000 scans – samples – should be aimed to achieve time convergence for the first and second order statistics);
- Determine the delay between two scans in order to have statistically independent samples (this time delay should be on the order of the Eulerian integral time scale).

2.8 VARYING RAINFALL EVENT SEQUENCES FOR LONG-TERM CATCHMENT EVOLUTION

2.8.1 Objective description

Long-term landscape evolution within a catchment is greatly influenced by soil erosion, which in its simplest form consists of three parts, the detachment of soil, and transport of this liberated soil and finally deposition of these soil particles elsewhere. This process can be initiated by raindrops impacting the soil surface, with resultant runoff further contributing to the erosion of the soil.

Despite significant research and interventions, soil erosion by water continues to be the dominant soil threat globally. The relationship between rainfall, runoff and erosion is known to be highly non-linear (Boardman and Favis-Mortlock, 1999, Philips, 2003, Cammeraat, 2004, Cantón et al, 2011, Vanmaercke et al, 2011, Cerdà et al, 2013), making the reduction or prevention of soil erosion a complex process.

Previous field and numerical modelling studies have demonstrated non-linear, self-organising behaviour within a catchment; such as intense rainfall events not necessarily producing the highest net erosion, or lower intensity rainfall resulting in higher erosion.

Currently there is a lack of data on the effect of varying magnitude-frequency rainfall event sequences on erosion and sediment dynamics in catchments. Baartman et al. (2013) explored the temporal effect using a numerical model and 50 different sequences of rainfall events, all with the same total rainfall, but with varying temporal occurrence of high and low magnitude events. The erosion response in this series of model runs did not appear to follow a particular trend. The purpose of these experiments was to test and quantify this non-linear effect of varying temporal sequences of rainfall event frequency-magnitude on erosion and sediment transport dynamics.

2.8.2 Tests and experiments

The experiments were conducted in the Total Environment Simulator (TES) at the University of Hull. The TES has an approximate working area of 6m wide by 11m long in total, and for these experiments was subdivided into two separate idealised catchments, each measuring 4m wide by 4m long, tapering at an angle to 1.5m wide across the final 1m of the catchment.

The shapes of the two catchments were identical to each other, and carefully rebuilt after each experimental run using a sliding template that could pass over a frame. This system was used to ensure repeatability in the experiments. Each catchment consisted of a valley shape with sloping sides of gradient 1 in 25, with an overall downward gradient of 1 in 10 towards the bottom of the catchment. This set-up can be seen in Figure 59.

The catchments themselves were constructed using two different grain sizes of sand. One consisted of a fine sand with an average grain size of 215 microns and one consisted of a coarser sand with an average grain size of 458 microns.

Across the outfall of each catchment, a large box was placed on a set of scales. This allowed water to flow into it, and collect sediment that had been mobilised and eroded from the catchment. At the opposite side of each box, was a high level water outflow. This allowed water to flow out into separate larger containers, each also placed on a set of scales. The water level within the sediment box was kept to just below the outfall, so as soon as water flowed in off the catchment, it could then

flow out into the larger containers and the discharge from the catchment could be measured (with a small time-lag as water flowed through the pipe system). To enable longer runs of continuous rainfall the larger discharge containers had a pumping system installed that could remove the water when the containers became full. This integrated system allowed us to continuously measure the sediment and water discharge from each plot whilst the experiments were running.

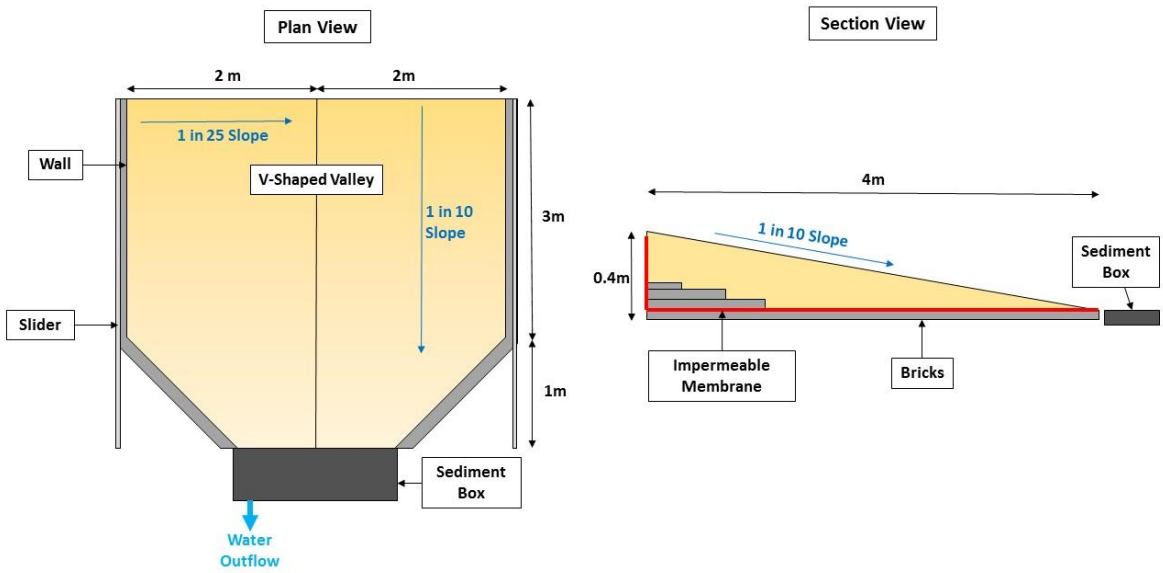

Figure 59 : Experimental Set-up

The TES is equipped with a rainfall generator system, comprising a total of 50 nozzles, each capable of producing an even water distribution over an approximately square area. The nozzles are spaced to ensure water will fall on all areas of the catchment. Ten nozzles were removed from the system since they were not directly above the catchments which enable higher rainfall amounts on the catchments themselves.

During the initial set-up, work to calibrate the rainfall was carried out. This was completed by using rain gauges distributed across each catchment, to measure the rainfall over a set time period. Different intensities were achieved by either altering the flow through the water pump, or by shutting off certain nozzles, resulting in three different rain intensities, representative of low (35mm/h), medium (92mm/h) and high (125mm/h) for these experiments. The lowest rainfall intensities were limited by the nozzle operation which requires a minimum flow rate for a spray to be reduced an the highest rainfall rates were limited by a combination of the pump discharge supplying the rainfall generator and the number of nozzles in operation. The maximum rainfall rate was obtained by only producing rainfall on one catchment at a time.

Each time, after the catchment was rebuilt, a spin-up event was run. This was the same for each experimental sequence and was designed to ensure that the initial conditions of the catchment were similar for each of the experiments. Then five different individual rain events as shown in Table 14, were used for the main experiments. The order of these events was altered for each experimental run resulting in a total of 9 different sequences.

Table 14 Individual Rainfall Events

Rain Intensity	Event Length
Spin Up (Low)	60 min
Low	30 min
Low	60 min
Medium	15 min
Medium	30 min
High	15 min

After each rainfall event, the nozzles had a tendency to drip causing rainsplash erosion of the surface. Therefore when each rainfall event ceased, covers were deployed to protect the sand surface from rainsplash erosion. Once the dripping had ceased, a terrestrial laser scanner (Faro x330) was used to scan the surface topography of both catchments. These could be used to produce a digital elevation model of the catchments, allowing comparisons with the previous state, so the evolution of the catchment between each rain event could be observed and quantified. Also, during this period, the sediment collected in the boxes was manually removed and weighed, before the next rain event began.

2.8.3 Initial results and discussion

These experiments were run over a period of 6 weeks, giving full results for 9 different rainfall sequences as shown in Figure 60. These results show a weakly non-linear relationship between the water run-off and the sediment erosion for both plots. As the volume of water discharged from each plot increases, the quantity of sediment being transported and removed increases by a growing proportion.

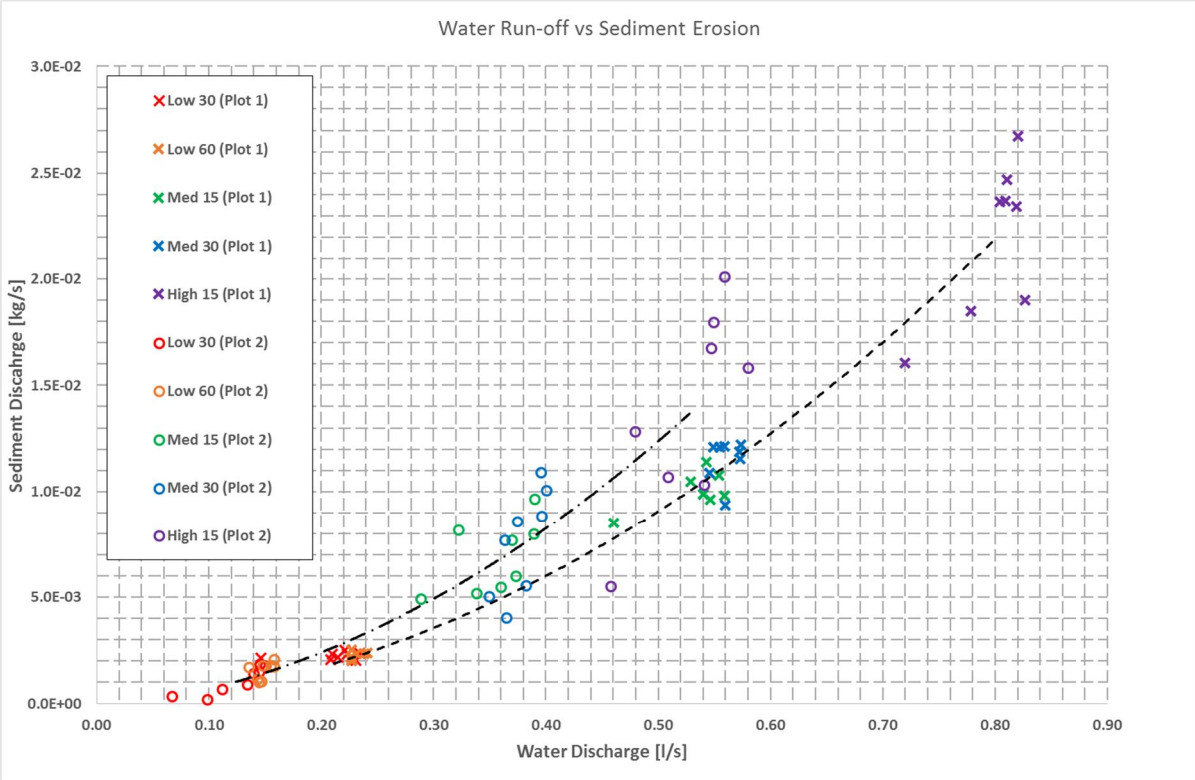

Figure 60 : Graph showing relationship between water run-off and sediment erosion during each rainfall event for both catchments

Each magnitude of rain intensity shows some scatter in both the water and sediment discharge within the results. This is likely due to the initial conditions of the catchment at the start of the event. For example, if the catchment was not fully saturated prior to the event, then the rain would first penetrate the surface rather than producing surface runoff, and mobilizing sediment. This is emphasized further in Figure 61, which shows the amount of sediment coming off in each event with relation to when in the sequence it was situated. It can be seen that usually, the later an event occurs within the sequence, the greater the mass of sediment that is eroded. However, it can also be observed that at a certain point this increase begins to decline, suggesting that there is a point at which the initial erosion and deposition has already occurred, and the sediment has reached a level of stability.

This possibility was further investigated in this work, by extending the rain sequence. Instead of consisting of 5 events, these initial sequences were repeated 3 times in succession, resulting in a total of 15 events. These results do show that as the experiments continues, the quantity of sediment removed from the system for each rain intensity does indeed decrease, despite the water discharge remaining approximately constant for the comparable events.

Overall, the results suggest that the sediment erosion is directly affected by the intensity of the rain, although this is not linear relationship. If the initial conditions are of a fully saturated sediment, then the sequencing of these events do not appear to have a major influence. However, if the catchment is not fully saturated at the start of the event, then this does effect the sediment erosion. It is therefore possible, that it is the saturation level of the sediment when each rain event begins, or other features of the catchments that causes the strong non-linearity that has been observed in the numerical modelling, and during field campaigns.

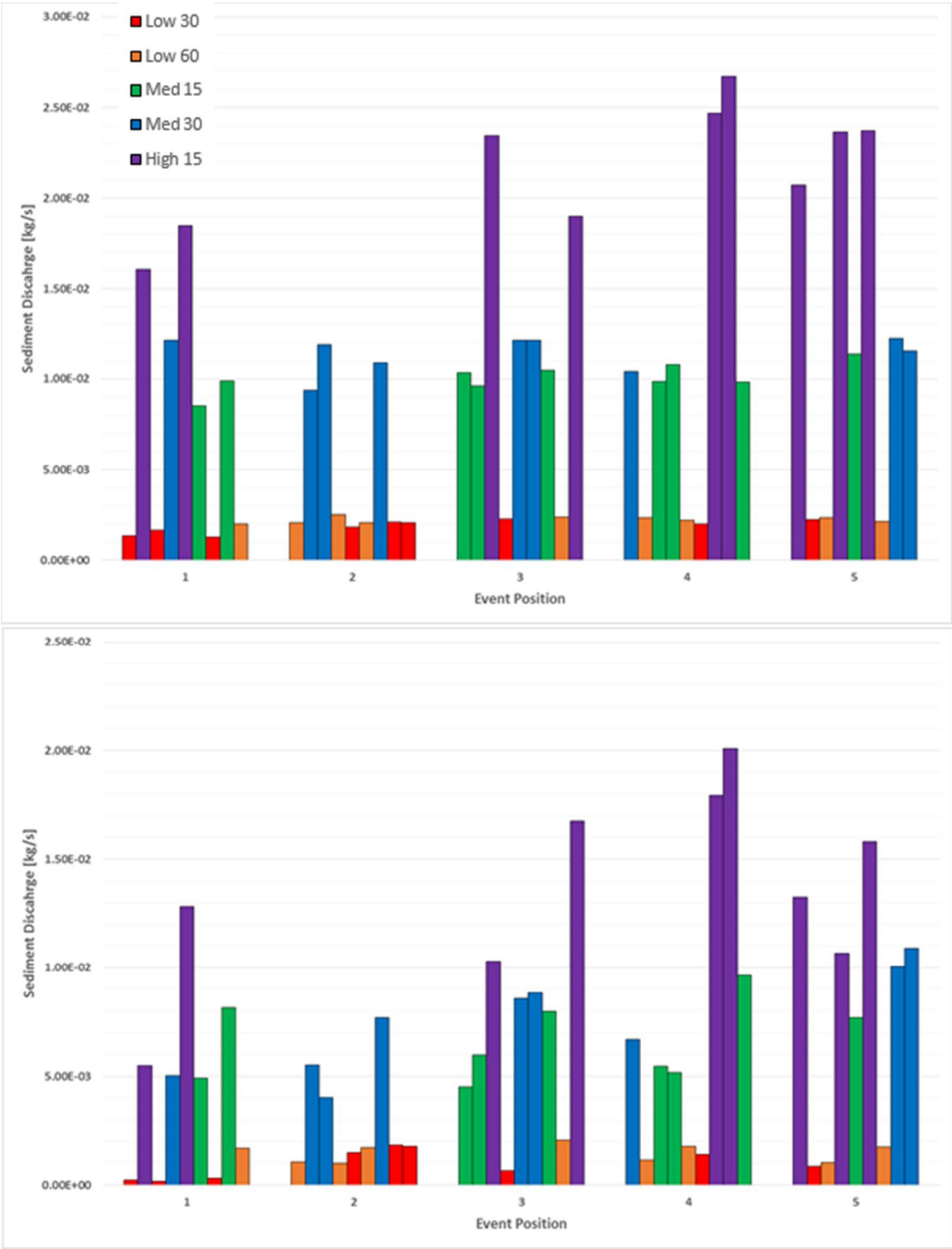

Figure 61 : Top: Graph showing sediment removal for each rain event and its position in sequence for plot 1 for each experimental run. Bottom: Graph showing sediment removal for each rain event and its position in sequence for plot 2 for each experimental run.

2.8.4 Recommendations

During these experiments, although the majority of procedures employed were fairly generic, a number of procedures specific to this type of work were developed. These are detailed in the following sections.

2.8.4.1 Equipment

The nozzle system used for these experiments provides a relatively uniform distribution of droplets in a wide angle solid cone square shaped pattern, rather than circular. This is important as it ensures that rainfall is distributed over the entire catchment, without any gaps at the edge of the cone. It is also important to space the nozzles appropriately to ensure full coverage of the catchment. In these experiments, to produce a low intensity rainfall, alternate lines of nozzles were turned off. The nozzles are situated (as shown in Figure 62) so that this is possible, without introducing gaps in the rainfall distribution.

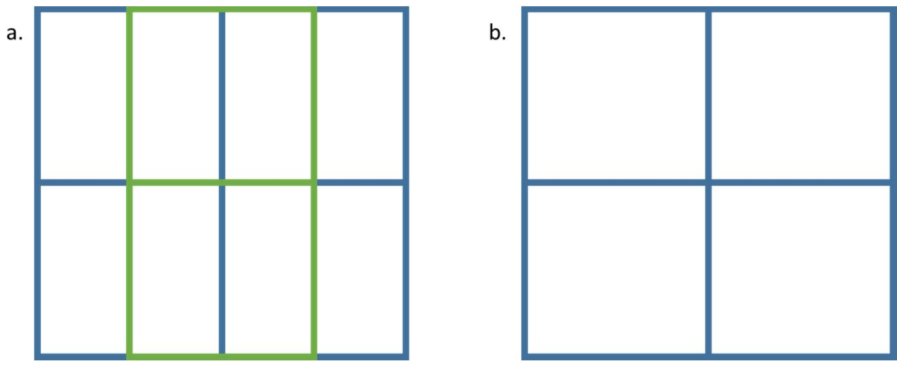

Figure 62 : Diagram showing distribution of rain when a) all the nozzles are operational, and b) when alternate lines of nozzles are closed.

2.8.4.2 Initial Conditions

To ensure the initial conditions for each sequence of events remained the same, a specific routine was developed. The sand on each catchment was loosened, and a template was then used to rebuild the catchment. This template shaped the central valley profile, and traversed a frame at the overall gradient of the catchment. The bottom section where the catchment narrowed was then rebuilt by hand.

Once the catchment was rebuilt, a spin-up event was conducted. This always consisted of the same event, and was initially identified as suitable to ensure that catchments were fully wetted, but without any major morphological changes occurring.

Finally, as the spin-up event took place the day before the main experimental sequence, to ensure the initial saturation of the catchments remained approximately the same throughout the experiments, a permeable hose was deployed across the top of the catchment. This allowed water to flow slowly onto the plot, keeping the saturation level consistent but without affecting the morphology of the catchment. This was also deployed overnight on the longer sequences which spanned several days.

2.8.4.3 Measurements

A number of different measurement techniques were utilised during these experiments. Firstly, the water and sediment coming off of each plot was continuously recorded. This was achieved by placing boxes across the bottom of the catchment, into which the sediment laden water would flow. Beneath each box was a set of scales, constantly weighing the contents. A high level outflow at the rear of the box then allowed water to flow out, depositing any sediment into this box. This overflow water was then directed into separate boxes also placed on scales.

It was important at the start of each rain event, to ensure that the water level was touching the bottom of the outflow pipe, meaning that as soon as water entered it would begin to flow out. The weight of the sediment within the box could then be reconciled with the readings by accounting for the displacement of water as it entered. The weight of the water was simply recorded in the latter boxes. These water boxes also included pumps that allowed the water to be removed during an event to avoid overflow. A full record of the weights was logged.

An alternative method for obtaining the weight of sediment coming off of the plots was to manually weigh it at the end of each rain event. This was simply done by emptying the sediment out of the boxes by hand and using a set of scales to obtain the saturated weight.

The final method for calculating the sediment removal is using the Terrestrial Laser Scanner. This allowed the production of digital elevation models of the catchments after each rainfall event. These could then be compared to calculate the sediment that had been removed.

References

Achanta, R., Appu Shaji, Kevin Smith, Aurelien Lucchi, Pascal Fua, and Sabine Süsstrunk, SLIC Superpixels, EPFL Technical Report no. 149300, June 2010.

Achanta, R., Appu Shaji, Kevin Smith, Aurelien Lucchi, Pascal Fua, and Sabine Süsstrunk, SLIC Superpixels Compared to State-of-the-art Superpixel Methods, IEEE Transactions on Pattern Analysis and Machine Intelligence, vol. 34, num. 11, p. 2274 - 2282, May 2012.

Albagnac, J., Moulin, F. Y., Eiff, O., Lacaze, L., & Brancher, P. (2014). A three-dimensional experimental investigation of the structure of the spanwise vortex generated by a shallow vortex dipole. Environmental Fluid Mechanics, 14(5), 957-970.

Allsop N.W.H. (1994) *Wave overtopping of sea walls, breakwaters and shoreline structures*, Technical Note 633 in Proc. ICE, Water, Maritime and Energy, December 1994, publn. Thomas Telford, London.

Allsop NWH & Hawkes PJ (2016) *RECIPE Task 8.2: Multi variable analysis and discussion on test conditions for wave overtopping*, HYDRALAB+ internal discussion note, Rev. 2, 28 January 2016

Baartman, J.E.M., Messelink, R., Keesstra, S.D. & Temme, A.J.M. (2013). *Linking landscape morphological complexity and sediment connectivity*. Earth Surf. Process. Landf. 38, 1457–1471.

Boardman, J., Favis-Mortlock,D. *Frequency-magnitude distributions for soil erosion, runoff and rainfall – a comparative analysis*. Zeitschrift für Geomorphologie, Supplement band, 1999. 115: p. 51-70.

Broderick, L.L. 1983. Riprap stability, a progress report. Proc. Coastal Structures '83. American Society of Civil Engineering, pp. 320– 330.

Brücker, C. (1996). 3-D scanning-particle-image-velocimetry: technique and application to a spherical cap wake flow. Applied Scientific Research, 56(2), 157-179.

Burcharth, H.F., T. Lykke Andersen, J.L. Lara. 2014. Upgrade of coastal defence structures against increased loadings caused by climate change: A first methodological approach. Coastal Engineering 87 (2014) pp. 112–121.

Cammeraat, E.L.H (2004), *Scale dependent thresholds in hydrological and erosion response of a semi-arid catchment in southeast Spain*, In Agriculture, Ecosystems & Environment, Volume 104, Issue 2, 2004, Pages 317-332

Cantón, Y., Solé-Benet, A., de Vente, J., Boix-Fayos, C., Calvo-Cases, A., Asensio, C., Puigdefábregas, J. (2011). *A review of runoff generation and soil erosion across scales in semiarid south-eastern Spain*. Journal of Arid Environments, Volume 75, Issue 12, 2011, Pages 1254-1261.

Capel, A. (2015). Wave run-up and overtopping reduction by block revetments with enhanced roughness. Coastal Engineering 104, p.76-92, Elsevier.

Cerdà, A., Brazier, R., Nearing, M., de Vente, J. (2013). *Scales and erosion*. CATENA, 2013. 102: p. 1-2.

Cheng, S., Tsarau, A., Li, H., Herman, A., Evers, K.-U. and Shen, H.H. (2017) Loads on structure and waves in ice (LS-WICE) project, Part 1: Wave attenuation and dispersion in broken ice fields, POAC'17, June 11-16, 2017, Busan, Korea.

CIRIA, CUR, CETMEF (2007). The Rock Manual. The use of rock in hydraulic engineering (2nd edition). C683, CIRIA, London.

De Almeida, E. 2017. Damage assessment of coastal structures in climate change adaptation. MSc thesis Delft University of Technology. DOI: uuid:f2548fc9-d1f6-443c-8f06-bec6d06c879e.

De Almeida, E. M.R.A. Van Gent, B. Hofland. 2018. Damage characterisation of rock armoured slopes. Proc. CoastLab2018, Santander, Spain.

Doble, M. De Carolis, J., G. Meylan, M. H. Bidlot, J.-R., and Wadhams P. (2015) Relating wave attenuation to pancake ice thickness, using field measurements and model results, Geophys. Res. Lett., 42, 4473–4481, doi:10.1002/2015GL063628.

De Michele, C., Salvadori, G., Passoni, G. and Vezzoli, R. (2007). *A multivariate model of sea storms using copulas*, Coastal Engineering, 54(10), pp. 734–751. doi: 10.1016/j.coastaleng.2007.05.007.

Dupuis, V., Proust, S., Berni, C., & Paquier, A. (2017). Mixing layer development in compound channel flows with submerged and emergent rigid vegetation over the floodplains. Experiments in Fluids, 58(4), 30.

EurOtop (2007) Editors: Pullen T., Allsop, N.W.H., Bruce T., Kortenhaus A., Schüttrumpf H. & van der Meer, J. W. *EurOtop: Wave Overtopping of Sea Defences and Related Structures: Assessment Manual*, pdf download available from : www.overtopping-manual.com

EurOtop, (2016). *Manual on wave overtopping of sea defences and related structures.* An overtopping manual largely based on European research, but for worldwide application. Van der Meer, J.W. Allsop, N.W.H., Bruce, T., De Rouck, J., Kortenhaus, A., Pullen, T., Schüttrumpf, H., Troch, P. and Zanuttigh, B., www.overtopping-manual.com

Ferreira, R (2006). Reconstruction of a Submerged Model Breakwater and Interface Estimation. Master degree thesis. Instituto Superior Técnico, Lisbon, Portugal.

Fortes, C.J.E.M., Lemos, R., Mendonça, A., Reis, M.T. (2018) Damage progression in rubble-mound breakwaters scale model tests, under a climate change storm sequence. Proceedings of the ASME 2018 37th International Conference on Ocean, Offshore and Arctic Engineering, OMAE2018, June 17-22, Madrid, Spain.

Gao, Q., Ortiz-Dueñas, C., & Longmire, E. K. (2013). Evolution of coherent structures in turbulent boundary layers based on moving tomographic PIV. Experiments in fluids, 54(12), 1625.

Herman, A., Evers, K.-U., Reimer, N., 2017a. Floe-size distributions in laboratory ice broken by waves. *The Cryosphere Discuss.*, doi: 10.5194/tc-2017-186.

Herman, A., Tsarau, A., Evers, K.-U., Li, H. and Shen, H.H. (2017b) Loads on structure and waves in ice (LS-WICE) project, Part 2: Sea ice breaking by waves, POAC'17, June 11-16, 2017, Busan, Korea.

Herman,A., Evers, K.-U., and Reimer ,N.(2018a). Floe-size distributions in laboratory ice broken by waves, The Cryosphere, 12, 685-699, 2018, https://doi.org/10.5194/tc-12-685-2018

Herman, A. et al. (2018b). Supplement of Floe-size distributions in laboratory ice broken by waves, Supplement of The Cryosphere, 12, 685–699, 2018, https://doi.org/10.5194/tc-12-685-2018-supplement

Hofland, B., M.R.A. Van Gent, T. Raaijmakers, F. Liefhebber. 2011. Damage evaluation using the damage depth. Proc. Coastal Structures 2011. Yokohama, Japan.

Hofland, B., M. Disco, M.R.A. Van Gent. 2014. Damage characterization of rubble mound roundheads. Proc. CoastLab2014. Varna, Bulgaria.

Hofland, B., Rosa-Santos, P., Taveira-Pinto, F., de Almeida Sousa, E., Lemos, R., Mendonça, A., & Fortes, C.J.E.M. (2017). Measuring damage in physical model tests of rubble mounds. In Coasts, Marine Structures and Breakwaters 2017: Liverpool, 5-7 September 2017. [125] ICE - Institution of Civil Engineering.

Hoonhout, B. M., Baart, F., & Van Thiel de Vries, J. S. M. (2014). Intertidal beach classification in infrared images. Journal of Coastal Research, 70(sp1), 657-662.

Hoonhout, B. M., Radermacher, M., Baart, F., & Van der Maaten, L. J. P. (2015a). An automated method for semantic classification of regions in coastal images. Coastal Engineering, 105, p.1-12, Elsevier.

Hoonhout, B. M., & Radermacher, M. (2015b). Flamingo: a coastal image analysis toolbox. GIT repository. doi:10.5281/zenodo.14596.

Hughes S.A. (1993) *Physical models and laboratory techniques in coastal engineering,* World Scientific, Singapore ISBN 981-02-1540-1.

IAHR 2011. Users Guide to Physical Modelling and Experimentation: Experience of the HYDRALAB Network. IAHR Design Manual. CRC Press/Balkema, pp. 245.

Lemos, R., J. Santos. 2013. Photogrammetric profile survey in scale model tests of rubble-mound breakwaters. Proc. 6th SCACR – International Short Course/Conference on Applied Coastal Research.

Lemos, R., Fortes, C.J.E.M., Mendonça, A., Rosa-Santos, P., Taveira-Pinto, F., Almeida, E., Hofland, B. (2018). Damage progression on a rubble mound breakwater in climate change scnarios. Proceedings of the 14 th Water Congress, APRH, 7 -9 th March, Évora, Portugal (in Portuguese).

Lemos, R., Neves, M.G., Fortes, C.J.E.M., Mendonça, A., Capitão, R. Reis. M.T. (2018) Damage progression in rubble-mound breakwaters scale model tests under different storm sequences. Proceedings of the 7th International Conference on the Application of Physical Modelling in Coastal and Port Engineering and Science (Coastlab18). Santander, Spain, May 22-26, 2018 (to be published).

Liberzon, A., Gurka, R., & Hetsroni, G. (2004). XPIV–Multi-plane stereoscopic particle image velocimetry. Experiments in Fluids, 36(2), 355-362.

Martín-Hidalgo, M., Martín-Soldevilla, M. J., Negro, V., Aberturas, P., & López-Gutiérrez, J. S. (2014). *Storm evolution characterization for analysing stone armour damage progression*. Coastal Engineering, 85, 1–11. doi:10.1016/j.coastaleng.2013.11.008

Martín Soldevilla, M. J., Martín-Hidalgo, M., Negro, V., López-Gutiérrez, J. S., & Aberturas, P. (2015). *Improvement of theoretical storm characterization for different climate conditions*. Coastal Engineering, 96, 71–80. doi:10.1016/j.coastaleng.2014.11.004

Marzeddu, A., De Leau, J., Mathijs, A., Gironella, X., Hofland, B., Gracia, V. and Sanchez Arcilla, A. (2017). Effects of storm duration and sequencing on armour layer damages, In Coasts, Marine Structures and Breakwaters 2017: Liverpool, 5-7 September 2017. [125] ICE - Institution of Civil Engineering.

Melby, J.A. and N. Kobayashi (1998). *Progression and variability of damage on rubble mound breakwaters*. Journal of Waterway, Port, Coastal, and Ocean Engineering. 124(6).

Melby, J. A., & Kobayashi, N. (2011). *Stone Armour Damage Initiation and Progression Based on the Maximum Wave Momentum Flux*. Journal of Coastal Research, 27(1), 110–119. doi:10.2112/JCOASTRES-D-09-00122.1

Mendonça, A., Lemos, R., Fortes, J., Reis, M.T., Neves, M.G., Ramos, A. and Capitão, R. (2017a). Overtopping events in breakwaters: comparison of 2D physical experiments and empirical formulae. Proc. 37th IAHR World Congress, 13-18 August, Kuala Lumpur, Malásia.

Mendonça, A.; Lemos, R, Reis, M.T., Fortes, C.J.E.M., Neves, M.G. and Ramos, A. (2017b). Runup in rubble mound breakwaters: comparison between physical model results and empirical formulae. Proc. 13º Simpósio de Hidráulica e Recursos Hídricos dos Países de Língua Portuguesa, 13-15, september, FEUP, Oporto (in portuguese).

Mendonça, A.; Fortes, C.J.E.M., Reis, M.T., Lemos, R, Neves, M.G., Ramos, A. and Capitão, R. (2017c). Overtopping over rubble mound breakwaters in climate change scenarios: physical model and empirical formulae results. Proc. 9as Jornadas Portuguesas de Engenharia Costeira e Portuária, 23-24, november, LNEC, Lisbon (in portuguese).

Mendonça, A., Lemos, R., Fortes, C.J.E.M., Capitão, R., Neves, M.T., Reis, M.T. (2018) Physical modelling of runup and overtopping over rubble mound breakwater in climate change scenarios. Proc. 14th Water Congress, 7 -9 th March, Évora, Portugal (in Portuguese).

Meylan, M. ., Bennetts, L. G. and Kohout A. L. (2014) In situ measurements and analysis of ocean waves in the Antarctic marginal ice zone, Geophys. Res. Lett., 41, 5046–5051, doi:10.1002/2014GL060809.

Molines, J., M.P. Herrera, T.J. Perez, V. Pardo, J.R. Medina. 2013. Laser Scanning technique to quantity randomness in cube and cubipod armour layers. Proc. Coastlab 2012. Gent, Belgium.

Nikora, V., McEwan, I., McLean, S., Coleman, S., Pokrajac, D., & Walters, R. (2007). Double-averaging concept for rough-bed open-channel and overland flows: Theoretical background. Journal of Hydraulic Engineering, 133(8), 873-883.

Oliveira, T. C. A. (2012). *Generacion de olas y estudio del rebase en un canal numerico de oleaje basado en el PFEM*. Universitat Politecnica de Catalunya.

Phillips, J.D., (2003). *Sources of nonlinearity and complexity in geomorphic systems*. Progress in Physical Geography, 2003. 27(1): p. 1-23.

Proust, S., Fernandes, J. N., Leal, J. B., Riviere, N., & Peltier, Y. (2017). Mixing layer and coherent structures in compound channel flows: Effects of transverse flow, velocity ratio, and vertical confinement. Water resources research.

Puente, I., J. Sande, H. González-Jorge, E. Peña-González, E. Maciñeira, J. Martínez-Sánchez, P. Arias. 2014. Novel image analysis approach to the terrestrial LiDAR monitoring of damage in rubble mound breakwaters. Ocean Engineering 91(2014) pp. 273–280.

Raaijmakers, T., F. Liefhebber, B. Hofland, P. Meys. 2012. Mapping of 3d-bathymetries and structures using stereophotography through an air-water-interface. Proc. CoastLab 2012, Ghent, Belgium.

Rigden, T., T. Stewart. 2012. Use of 3D laser scanning in determining breakwater damage parameters. Proc. Coastlab 2012, Ghent, Belgium.

Schröder, A., Geisler, R., Staack, K., Elsinga, G. E., Scarano, F., Wieneke, B., ... & Westerweel, J. (2011). Eulerian and Lagrangian views of a turbulent boundary layer flow using time-resolved tomographic PIV. Experiments in fluids, 50(4), 1071-1091.

Shen, H.H. and Squire, V.A. (1998) Wave damping in compact pancake ice fields due to interactions between pancakes, AGU Antarctic Research Series 74, Antarctic Sea Ice: Physical Processes, Interactions and Variability, (Ed. Dr. Martin O. Jeffries): 325-342.

Silva, E., Allsop, W., Riva, R., Rosa-Santos, P., Mendonça, A. and Teresa Reis, M. (2017). The Conundrum of Specifying very low Wave Overtopping Discharges, In Coasts, Marine Structures and Breakwaters 2017: Liverpool, 5-7 September 2017. [125] ICE - Institution of Civil Engineering.

Squire, V.A. (2007) Of ocean waves and sea-ice revisited, Cold Reg. Sci. Technol., 49(2), 110–133.

Stagonas, D., Marzeddu, A., Gironella, X. and Sánchez-Arcilla, A. (2016). *Measuring wave impact induced pressures with a pressure mapping system*, Coastal Engineering, (112), pp. 44–56.

Todd, D., Sutherland, J., Crossouard, N., Rankine, R., Rigden, T. and Whitehouse, R., 2016. *Comparison between methods for creating DEMs of physical models*. Proc 6th Int Conf on the Application of Physical Modelling in Coastal and Port Engineering and Science (Coastlab '16).

Tsarau, A., Sukhorukov, S., Herman, A., Evers, K.-U. and Loset, S. (2017) Loads on structure and waves in ice (LS-WICE) project, Part 3: Ice-structure interaction under wave conditions, POAC'17, June 11-16, 2017, Busan, Korea.

Van der Meer, J. W. (1988a). *Rock Slopes and Gravel Beaches under wave attack*.

Van der Meer, J. W. (1988b). *Stability of Cubes, Tetrapods and Accropode*, Proceedings of the Conference Breakwaters '88, 1988(m), pp. 59–68.

Van der Meer, J. W. (1999). *Design of concrete armour layers*, Proceedings of the International Conference Coastal Structures '99 : Santander, Spain, 7-10 June 1999, Volume 1, pp. 213–221.

Van Gent, M.R.A, and I. van der Werf. 2010. Stability of breakwater roundheads during construction. Proc. of 32nd International Conference on Coastal Engineering (ICCE2010). Shanghai, China.

Van Gent, M.R.A., De Almeida E., Hofland B., 2018, Statistical analysis of the stability of rock armoured slopesCoastLab2018, Santander, Spain.

Vanmaercke, M., Jean Poesen, J., Verstraeten, G., de Vente, J., Ocakoglu, F. (2011), *Sediment yield in Europe: Spatial patterns and scale dependency*, Geomorphology, 130(3–4): 142-161,.

Wadhams, P., Squire, V.A., Goodman, D.J., Cowan, A.M. and Moore, S.C. (1988) The Attenuation Rates of Ocean Waves in the Marginal Ice Zone, J. Geophys. Res., 93(C6), 6799-6818.

Westoby, M.J, J. Brasington, N.F. Glasser, M.J. Hambrey, J.M. Reynolds (2012) *Structure-from-Motion photogrammetry: A low-cost, effective tool for geoscience applications,* Geomorphology, 179: 300-314, 10.1016/j.geomorph.2012.08.021

White, B. L., & Nepf, H. M. (2007). Shear instability and coherent structures in shallow flow adjacent to a porous layer. Journal of Fluid Mechanics, 593, 1-32.

Wolters G, van Gent M, Allsop W, Hamm L, & Mühlestein D, (2007) *Guidelines for physical model testing of breakwaters: Rubble mound breakwaters,* Doc. Ref. HYDRALAB III, Deliverable NA3.1, publn Deltares, Delft.

Wolters G, van Gent M, Allsop W, Hamm L, & Mühlestein D, (2009) *HYDRALAB III: Guidelines for physical model testing of rubble mound breakwaters*, Proc ICE Conf. on Coasts, Marine Structures & Breakwaters, Edinburgh, September 2009, publn. Thomas Telford, London.